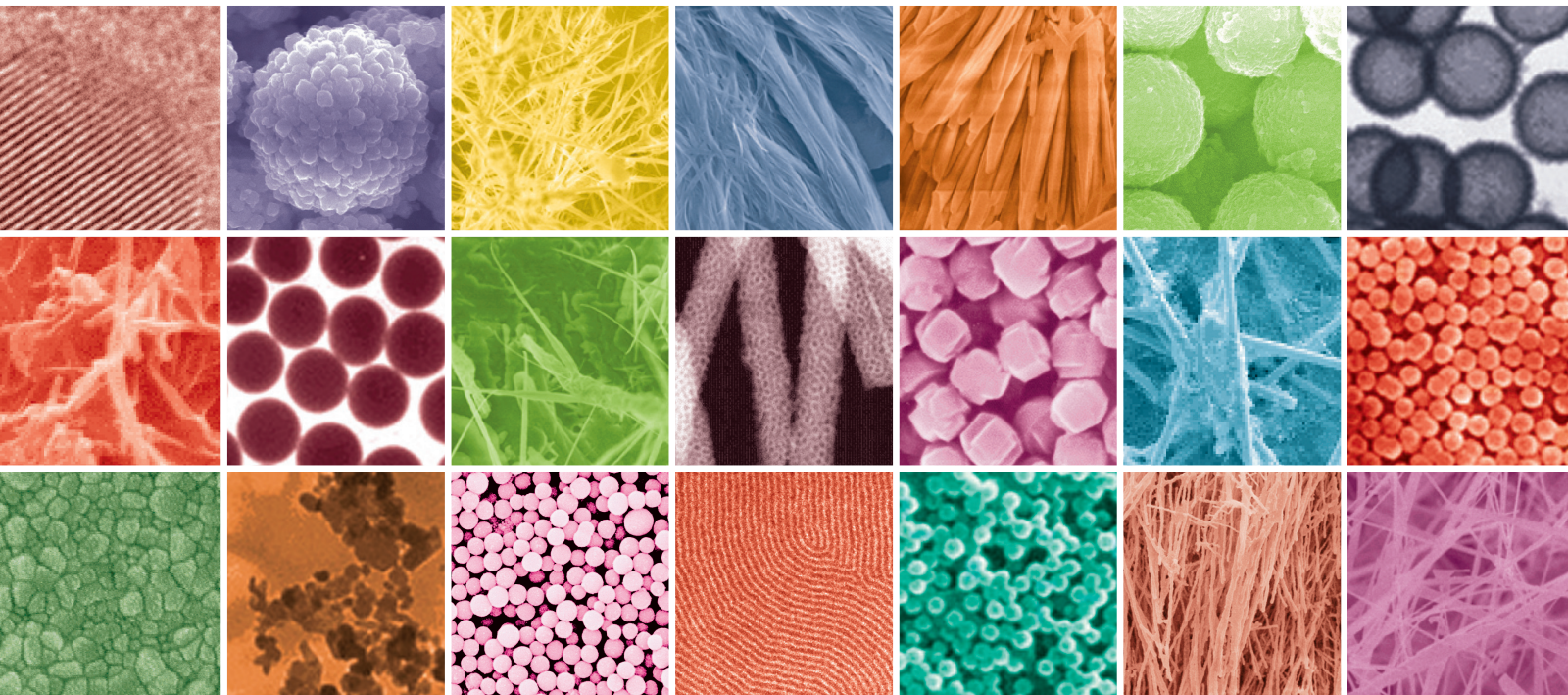


Nanomaterials Processed by Spark Plasma Sintering

Guest Editors: Faming Zhang, Bikramjit Basu, Lianjun Wang, Izabel Fernanda Machado, and Claude Estournès





Nanomaterials Processed by Spark Plasma Sintering

Nanomaterials Processed by Spark Plasma Sintering

Guest Editors: Faming Zhang, Bikramjit Basu, Lianjun Wang,
Izabel Fernanda Machado, and Claude Estournès



Copyright © 2013 Hindawi Publishing Corporation. All rights reserved.

This is a special issue published in "Journal of Nanomaterials." All articles are open access articles distributed under the Creative Commons Attribution License, which permits unrestricted use, distribution, and reproduction in any medium, provided the original work is properly cited.

Editorial Board

Katerina E. Aifantis, Greece
Nageh K. Allam, USA
Margarida Amaral, Portugal
Xuedong Bai, China
Lavinia Balan, France
Enrico Bergamaschi, Italy
Theodorian Borca-Tasciuc, USA
C. Jeffrey Brinker, USA
Christian Brosseau, France
Xuebo Cao, China
Shafiq Chowdhury, USA
Kwang-Leong Choy, UK
Cui Chunxiang, China
Miguel A. Correa-Duarte, Spain
Shadi A. Dayeh, USA
Claude Estourns, France
Alan Fuchs, USA
Lian Gao, China
Russell E. Gorga, USA
Hongchen Chen Gu, China
Mustafa O. Guler, Turkey
John Zhanhu Guo, USA
Smrati Gupta, Germany
Michael Harris, USA
Zhongkui Hong, China
Michael Z. Hu, USA
David Hui, USA
Y.-K. Jeong, Republic of Korea
Sheng-Rui Jian, Taiwan
Wanqin Jin, China
Rakesh K. Joshi, UK
Zhenhui Kang, China
Fathallah Karimzadeh, Iran
Alireza Khataee, Iran

Do Kyung Kim, Korea
Alan K. T. Lau, Hong Kong
Burtrand Lee, USA
Jun Li, Singapore
Benxia Li, China
Xing-Jie Liang, China
Shijun Liao, China
Gong Ru Lin, Taiwan
J.-Y. Liu, USA
Tianxi Liu, China
Jue Lu, USA
Songwei Lu, USA
Daniel Lu, China
Ed Ma, USA
Gaurav Mago, USA
Santanu K. Maiti, India
Sanjay R. Mathur, Germany
Vikas Mittal, UAE
Weihai Ni, Germany
Sherine Obare, USA
Atsuto Okamoto, Japan
Abdelwahab Omri, Canada
Edward Andrew Payzant, USA
Kui-Qing Peng, China
Anukorn Phuruangrat, Thailand
Suprakas Sinha Ray, South Africa
Ugur Serincan, Turkey
Huaiyu Shao, Japan
Donglu Shi, USA
Vladimir Sivakov, Germany
Marinella Striccoli, Italy
Bohua Sun, South Africa
Saikat Talapatra, USA
Nairong Tao, China

Titipun Thongtem, Thailand
Somchai Thongtem, Thailand
Alexander Tolmachev, Ukraine
Valeri P. Tolstoy, Russia
Tsungh-Yen Tsai, Taiwan
Takuya Tsuzuki, Australia
Raquel Verdejo, Spain
Mat U. Wahit, Malaysia
Zhenbo Wang, China
Ruiping Wang, Canada
Shiren Wang, USA
Cheng Wang, China
Yong Wang, USA
Jinquan Wei, China
Ching-Ping Wong, Hong Kong
Xingcai Wu, China
Guodong Xia, Hong Kong
Zhi Li Xiao, USA
Ping Xiao, UK
Yangchuan Xing, USA
Shuangxi Xing, China
N. Xu, China
Doron Yadlovker, Israel
Yingkui Yang, China
Khaled Youssef, USA
Kui Yu, Canada
William W. Yu, USA
Haibo Zeng, China
Tianyou Zhai, Japan
Renyun Zhang, Sweden
Bin Zhang, China
Yanbao Zhao, China
Lianxi Zheng, Singapore
Chunyi Zhi, Hong Kong

Contents

Nanomaterials Processed by Spark Plasma Sintering, Faming Zhang, Bikramjit Basu, Lianjun Wang, Izabel Fernanda Machado, and Claude Estournès
Volume 2013, Article ID 346952, 1 page

Fabrication and Thermoelectric Properties of Graphene/Bi₂Te₃ Composite Materials, Beibei Liang, Zijun Song, Minghui Wang, Lianjun Wang, and Wan Jiang
Volume 2013, Article ID 210767, 5 pages

Control of FeAl Composition Produced by SPS Reactive Sintering from Mechanically Activated Powder Mixture, S. Paris, E. Gaffet, and F. Bernard
Volume 2013, Article ID 150297, 11 pages

Reactive Spark Plasma Sintering: Successes and Challenges of Nanomaterial Synthesis, Dina V. Dudina and Amiya K. Mukherjee
Volume 2013, Article ID 625218, 12 pages

Dense Nanostructured Nickel Produced by SPS from Mechanically Activated Powders: Enhancement of Mechanical Properties, F. Naimi, L. Minier, S. Le Gallet, H. Couque, and F. Bernard
Volume 2013, Article ID 674843, 11 pages

Formation Behavior of Continuous Graded Composition in Ti-ZrO₂ Functionally Graded Materials Fabricated by Mixed-Powder Pouring Method, Murali Jayachandran, Hideaki Tsukamoto, Hisashi Sato, and Yoshimi Watanabe
Volume 2013, Article ID 504631, 8 pages

Spark Plasma Sintering and Densification Mechanisms of Antimony-Doped Tin Oxide Nanoceramics, Junyan Wu, Fei Chen, Qiang Shen, Julie M. Schoenung, and Lianmeng Zhang
Volume 2013, Article ID 561895, 7 pages

Editorial

Nanomaterials Processed by Spark Plasma Sintering

**Faming Zhang,¹ Bikramjit Basu,² Lianjun Wang,³
Izabel Fernanda Machado,⁴ and Claude Estournès⁵**

¹ *Physics of New Materials, Institute of Physics, University of Rostock, 18055 Rostock, Germany*

² *Materials Research Center, Indian Institute of Science (IISc), Bangalore 560012, India*

³ *College of Materials Science and Engineering, Donghua University, Songjiang District, Shanghai 201620, China*

⁴ *Departamento de Engenharia Mecatrônica e Sistemas Mecânicos, Escola Politécnica da Universidade de São Paulo, 05508-900 São Paulo, SP, Brazil*

⁵ *Institut Carnot CIRIMAT (UMR 5085 CNRS-UPS-INP), Université Paul Sabatier, 118 Route de Narbonne, 31062 Toulouse Cedex 09, France*

Correspondence should be addressed to Faming Zhang; faming.zhang@uni-rostock.de

Received 17 November 2013; Accepted 17 November 2013

Copyright © 2013 Faming Zhang et al. This is an open access article distributed under the Creative Commons Attribution License, which permits unrestricted use, distribution, and reproduction in any medium, provided the original work is properly cited.

The spark plasma sintering (SPS), a variant of field-assisted sintering (FAST) or pulsed electric current sintering (PECS), is a novel pressure assisted pulsed electric current sintering process, which utilizes ON-OFF DC pulse energizing. Due to the repeated application of an ON-OFF DC pulse voltage and current flow between powder particles, the spark discharges and the Joule heating (local high temperature state) are therefore dispersed to the overall specimen. The SPS process is based on the electrical spark discharge phenomenon and is a high efficient, energy saving technique with a high heating rate and a short holding time. The problem of rapid grain growth of nanomaterials during conventional sintering can be inhibited to a larger extent by using the SPS technique. The SPS can be used for diverse novel bulk material applications, but it is particularly suitable for the processing of nanomaterials. Despite such anticipated advantages, the optimization of the process window (heating rate-temperature-time) in SPS process is a challenging task. More importantly, the underlying mechanisms for superfast densification still remains to be explored.

In the above perspective, this special issue contains some peer-reviewed research papers, which address some of the exciting issues or illustrate new nanomaterials development using SPS. This special issue's papers are all very much of the "head up" variety. First D. V. Dudina and A. K. Mukherjee reviewed the reactive SPS on the successes and challenges of

nanomaterial synthesis. Secondly, some work on bioceramics is covered, for example, antimony-doped tin oxide nanoceramics (J. Wu et al.). Additionally, we look to some works on the nanostructured metals, for example, nanostructured nickel (F. Naimi et al.) and FeAl alloys (S. Paris et al.). In the end, the SPS of nanocomposites is also introduced, for example, graphene/Bi₂Te₃ thermoelectric materials (B. Liang et al.) and Ti-ZrO₂ functionally graded materials (M. Jayachandran et al.).

This field of "nanomaterials processed by SPS" develops very fast. This special issue is just a tip of the iceberg, but we also can conjure up the whole thing through seeing a part of it.

We thank all the authors for their contribution to the literature on SPS.

*Faming Zhang
Bikramjit Basu
Lianjun Wang
Izabel Fernanda Machado
Claude Estournès*

Research Article

Fabrication and Thermoelectric Properties of Graphene/Bi₂Te₃ Composite Materials

Beibei Liang,¹ Zijun Song,¹ Minghui Wang,² Lianjun Wang,¹ and Wan Jiang¹

¹ State Key Laboratory for Modification of Chemical Fibers and Polymer Materials, Donghua University, 2999 People of North Road, Shanghai 201620, China

² Instrumental Analysis Center, Donghua University, Shanghai 201620, China

Correspondence should be addressed to Minghui Wang; wmh@dhu.edu.cn and Wan Jiang; wanjiang@dhu.edu.cn

Received 22 March 2013; Accepted 21 August 2013

Academic Editor: Faming Zhang

Copyright © 2013 Beibei Liang et al. This is an open access article distributed under the Creative Commons Attribution License, which permits unrestricted use, distribution, and reproduction in any medium, provided the original work is properly cited.

Graphene/Bi₂Te₃ thermoelectric materials were prepared by spark plasma sintering (SPS) using hydrothermal synthesis of the powders as starting materials. The X-ray diffraction (XRD) and field emission scanning electron microscope (FE-SEM) were used to investigate the phase composition and microstructure of the as-prepared materials. Electrical resistivity, Seebeck coefficient, and thermal conductivity measurement were applied to analyze the thermoelectric properties. The effect of graphene on the performance of the thermoelectric materials was studied. The results showed that the maximum dimensionless figure of merit of the graphene/Bi₂Te₃ composite with 0.2 vol.% graphene was obtained at testing temperature 475 K, 31% higher than the pure Bi₂Te₃.

1. Introduction

Thermoelectric (TE) materials can directly convert thermal energy to electricity and vice versa through all solid-state energy conversion. They have been considered as one of the potential solutions to energy crisis and global climate changes [1–3]. Good thermoelectric materials require a high Seebeck coefficient (α), high electrical conductivity (σ), and low thermal conductivity (κ) for a high figure of merit ($Z = \alpha^2\sigma/\kappa$), which is related to the thermoelectric energy conversion efficiency. These parameters are not independent for a given material.

Bismuth telluride- (Bi₂Te₃-) based compounds, as one of the most excellent thermoelectric materials near room temperature, are extensively used in the area of medical appliance, microelectronic devices, biologic slug, and so on [4, 5]. Due to the wide practical applications, a great deal of research has focused on improving the TE properties of Bi₂Te₃ materials [6–12]. Nanostructure can enhance the electronic density of states near Fermi level, and the nanostructured thermoelectric materials have a large number of boundaries that will strongly scatter the phonons and carries [13]. Therefore, the Seebeck coefficient is improved,

and the thermal conductivity is reduced, which lead to the improvement of thermoelectric properties.

Graphene has become one of the most exciting topics of research in recent years. This two-dimensional material constitutes layers of carbon atoms arranged in six-membered rings. As a new kind of function materials, graphene has high conductivity, high carrier mobility, and excellent mechanical properties [14, 15]. So, it has been widely used to prepare various kinds of functional composites since the first report of the free standing graphene [16–20].

In this work, Graphene/Bi₂Te₃ nanopowders with different graphene contents were synthesized by hydrothermal synthesis, and then bulk materials were fabricated by spark plasma sintering (SPS). The TE properties of the Graphene/Bi₂Te₃ composite materials sintered body, prepared from the synthesized nanopowders, were characterized. Our studies focus on the particle morphology and sintering behavior of Graphene/Bi₂Te₃ nanopowders.

2. Experimental Procedure

All the chemicals were of analytical grade and were used without further purification. Graphene nanosheet (JK Scientific

Inc.) was dispersed in the alcohol to form a certain concentration of solution.

In a typical procedure, BiCl_3 and Te powders with the stoichiometric ratio of Bi:Te = 2:3 were mixed in a beaker filled with a certain amount of distilled water. Then different quantities of graphene nanosheet (0, 0.1 vol.%, 0.2 vol.%, 2 vol.%) were dissolved in the beaker. The solution was stirred immediately following the addition of NaOH as the pH controller, hydrazine hydrate ($\text{N}_2\text{H}_4 \geq 50\%$ v/v) as the reductant, and ethylenediaminetetraacetic acid disodium salt (EDTA-2Na) in sequence. The process of ultrasonic agitation lasts 0.5 h. Finally, the solution was removed into the autoclave with the water up to 80% volume. The solution was heated to 180°C and then cooled naturally to room temperature after about 8 h. The dark-grey powders in the autoclave were centrifuged and washed with distilled water and anhydrous ethanol several times and then dried in vacuum oven at 60°C for 5 h. The phase structures of the samples were investigated by X-ray diffraction (XRD) using Cu/ $K\alpha$ radiation ($\lambda = 1.54056 \text{ \AA}$). The morphologies of powders were observed by field emission scanning electron microscopy (FESEM).

The as-prepared Graphene/ Bi_2Te_3 nanopowders were sintered using spark plasma sintering (Dr. Sinter 725; Sumitomo Coal Mining Co., Tokyo, Japan). The nanopowders were loaded into cylindrical carbon dies with an inner diameter of 10 mm. The heating rate was controlled in the range of 70°C/min, and the pressure was set at 80 MPa. The final temperature was selected at 350°C for a dwelling time of 6 min. The Seebeck coefficient and electrical conductivity were measured by using temperature differential and four-probe methods, respectively, with Ulvac-Riko ZEM-3 equipment in a helium atmosphere. The thermal conductivity was estimated from the specific heat, thermal diffusivity, and density by using DSC, laser flash method (Model No. LFA 447 NanoFlash), and Archimedes immersion method, respectively. The thermoelectric figure of merit was evaluated.

3. Results and Discussion

Figure 1 shows the X-ray diffraction (XRD) patterns of Graphene/ Bi_2Te_3 compounds with different contents of graphene. Main diffraction peaks in Figure 1 could be indexed according to JCPDS 15-0863 for Bi_2Te_3 . Diffractions of other phases could not be found such as Te, Bi, or their compounds. It indicated that we had obtained a pure Bi_2Te_3 phase with good crystallinity. As the contents of graphene in the composites are very low, the diffraction peaks of graphene show low strength. We found that the Graphene/ Bi_2Te_3 composite powders showed the same XRD pattern as the Bi_2Te_3 .

Figure 2 shows the morphologies of the as-prepared Graphene/ Bi_2Te_3 nanopowders with different concentrations of graphene. Figure 2(a) reveals the synthesized Bi_2Te_3 powders with a size of 30–200 nm, which are agglomerated and nonuniform. Figure 2(b) demonstrates the existence of graphene in the composite powders (marked by arrow), and the particle size is uniform. This is because the presence of graphene hindered the Bi_2Te_3 grain growth. Therefore, Bi_2Te_3

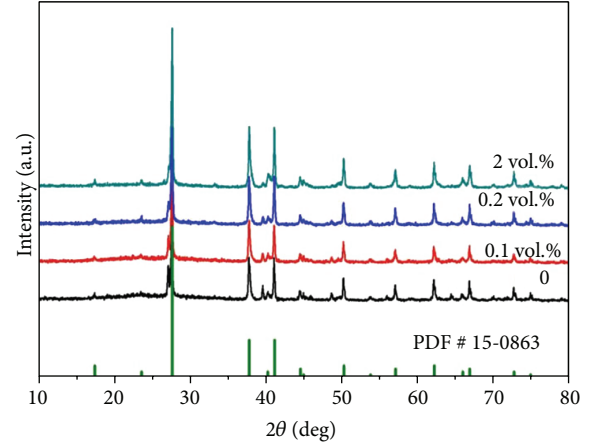


FIGURE 1: XRD patterns of Graphene/ Bi_2Te_3 nanopowders with different contents of graphene.

TABLE 1: Relative density of Bi_2Te_3 /graphene bulk materials fabricated by SPS.

	Content of graphene			
	0	0.1 vol.%	0.2 vol.%	2 vol.%
Actual density (g/cm^3)	7.71	7.70	7.68	7.57
Theoretical density (g/cm^3)	7.86	7.85	7.85	7.79
Relative density	98.09%	98.09%	97.83%	97.18%

grains become smaller and homogeneous. From Figures 2(c)-2(d), the existence form of graphene and Bi_2Te_3 can be observed clearly. A large number of Bi_2Te_3 particles were coated by large nanosheet of graphene. Figure 2(d) is the place that the arrow pointed in Figure 2(c). The coated Bi_2Te_3 particles can be seen clearly through the graphene.

SPS was used to densify the Bi_2Te_3 /graphene composite powders. The actual densities of Bi_2Te_3 /graphene bulk materials were calculated using the Archimedes immersion method with deionized water as the immersion medium. The theoretical densities of the samples were calculated according to the rule of mixtures. The relative densities are shown in Table 1. The results reveal that the relative densities of the Bi_2Te_3 /graphene bulk materials decrease slightly as the contents of graphene increase.

Figure 3 shows FESEM images for the fracture surface of bulk samples with different contents of graphene. Comparing pure Bi_2Te_3 sample with 2 vol.% graphene composited samples, it is easy to find that the pure Bi_2Te_3 samples are well-densified, but there are some holes (marked by arrow) in the composite. And, it is observed that the average grain sizes of the two bulk samples are obviously different. The grain size of composite sample is smaller than pure Bi_2Te_3 sample. It is suggested that the existence of graphene not only reduced the density of the sample but also decreased the size of grains. The density reduced makes the carrier concentration drop which is detrimental to the improvement of electrical conductivity. But, at the same time, the decrease of the grain size increases the ability of grain boundary scattering phonons, which is beneficial to the decrease of the thermal conductivity.

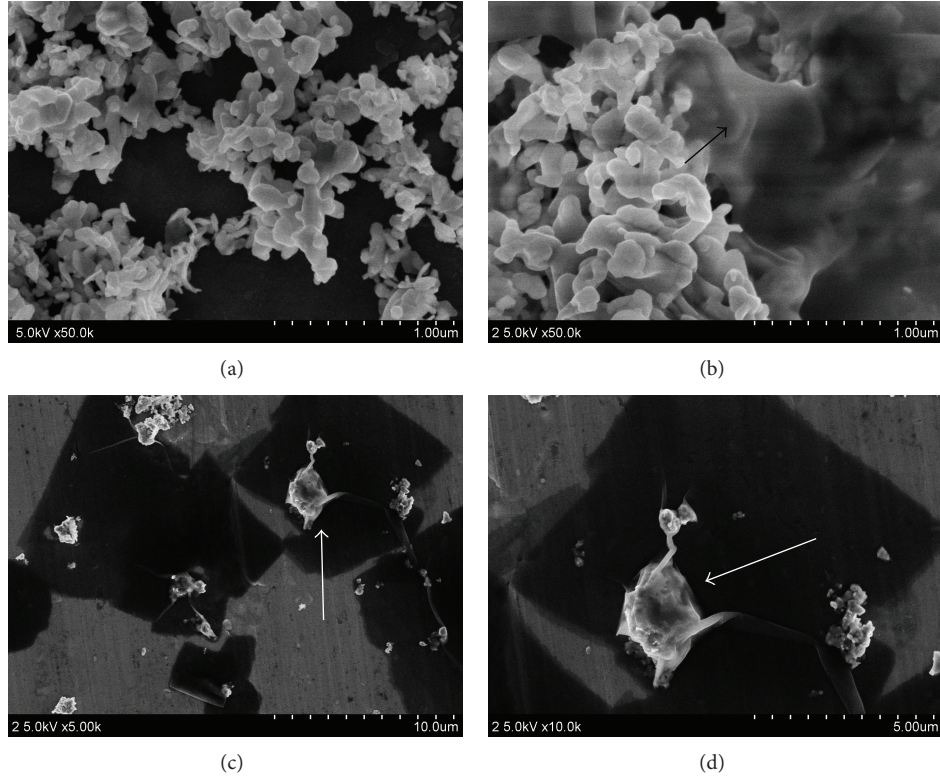


FIGURE 2: FESEM images of graphene/ Bi_2Te_3 nanopowders with different graphene contents, (a) 0, ((b)–(d)) 2 vol.%.

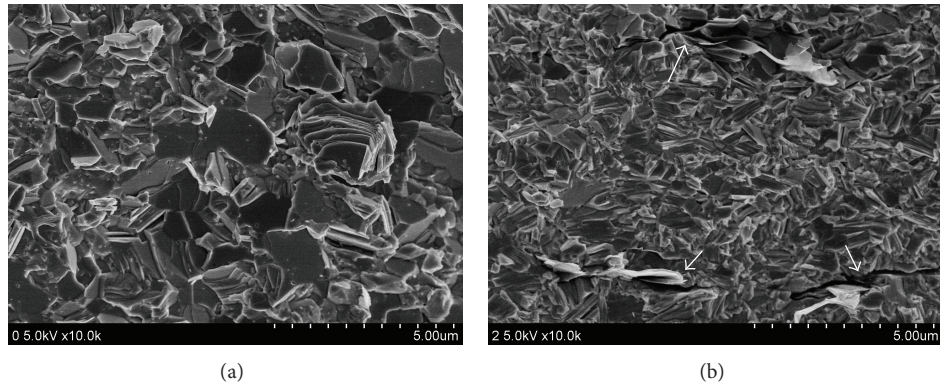


FIGURE 3: FESEM fractographs of bulk Bi_2Te_3 /graphene with different graphene contents, (a) 0, (b) 2 vol.%.

The temperature dependence of Seebeck coefficient is presented in Figure 4(a). The negative Seebeck coefficient confirmed that the electrical charge was transported mainly by electron and all the samples are n-type conductor. A similar varying trend of the Seebeck coefficient is showed in the whole measuring temperature range. The absolute values of Seebeck coefficient first increase and then decrease with raising the measuring temperature. The Seebeck coefficient of semiconductor can be expressed as

$$\alpha = (\gamma + C - \ln n_e) \frac{k_B}{e}, \quad (1)$$

where k_B is the Boltzmann constant, e is the electron charge, γ is the exponent of the power function in the

energy-dependent relaxation time expression, C is constant, and n_e is the electron concentration. Therefore, as shown in Figure 4(a), the Seebeck coefficient of Graphene/ Bi_2Te_3 decreased at high temperatures (>400 K) with increasing the temperature due to an increase in the carrier concentration by intrinsic conduction.

Figure 4(b) shows the temperature dependence of the electrical conductivity. All the samples show a decreasing trend in the electrical conductivity with raising the measuring temperature, which indicate a metallic conducting behavior. With the temperature rising, scattering process of lattice vibration on the carrier is strengthened gradually, and the carrier mobility is reduced. So, the conductive performance of materials declines. The highest and lowest conductivity

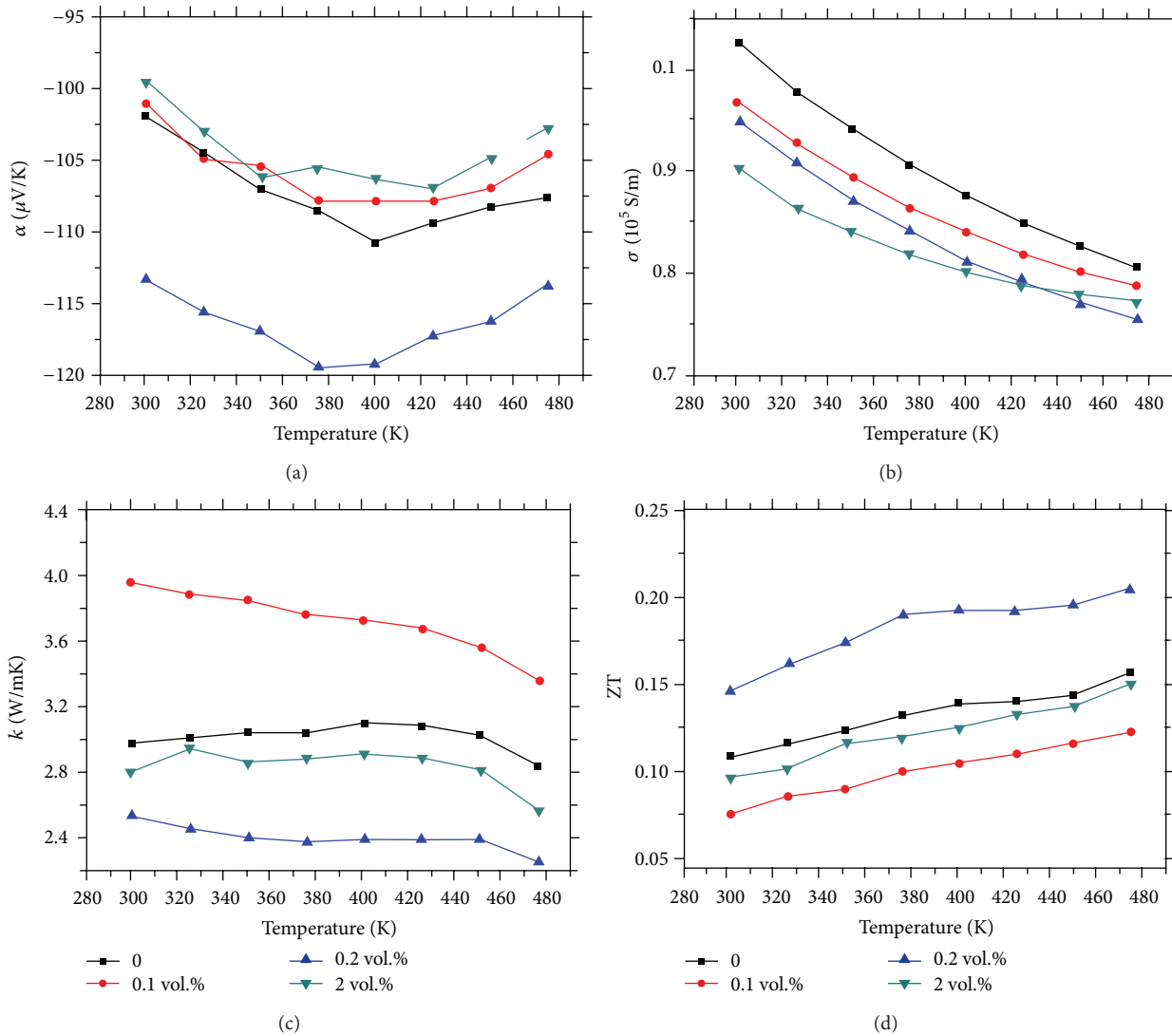


FIGURE 4: Temperature dependence of Seebeck coefficient (a), electrical conductivity (b), thermal conductivity (c), and ZT (d) for bulk materials of different graphene contents.

values at room temperature are 1.03×10^5 S/m and 0.91×10^5 S/m, respectively. There is no big difference.

Figure 4(c) shows the temperature dependence of the total thermal conductivity on the Graphene/ Bi_2Te_3 compounds. The thermal conductivity of Bi_2Te_3 increased roughly with increasing the temperature, whereas that of the graphene/ Bi_2Te_3 composites decreased slightly with increasing the temperature. With an increase in the temperature, the total thermal conductivity of the compounds decreased roughly.

Figure 4(d) gives the dimensionless figures of merit, ZT of all composite samples. A remarkable tendency can be seen from Figure 4(d). With the temperature rising, ZT value increases and the effect of graphene is obvious. The maximum ZT of about 0.21 is obtained in the present work of the sample with 0.2 vol.% graphene. The microstructure has a certain extent effect on the performance of the material, but ZT value depends on a combination of various factors, so higher ZT could be expected by the composition optimization.

4. Conclusions

In summary, the bulk nanostructured Graphene/ Bi_2Te_3 composites have been prepared by hydrothermal synthesis followed by spark plasma sintering. In the precursor nanopowders, Bi_2Te_3 particles were coated by graphene nanosheets with a grain sizes varying from 30~200 nm. The effect of graphene composite content on the thermoelectric properties of nanostructured bulk materials is investigated in this study. The maximum ZT value of about 0.21 has been obtained at 475 K with the 0.2 vol.% content of graphene, which is 31% higher than that of pure Bi_2Te_3 materials.

Acknowledgments

This work was supported by the Natural Science Foundation of China (no. 51374078), Program for New Century Excellent Talents in University (NCET-10-0323), "Shu Guang" project supported by Shanghai Municipal Education Commission

and Shanghai Education Development Foundation (no. 11SG34), Shanghai Rising-Star Program (no. 12QH1400100), Shanghai Committee of Science and Technology (no. 13JC1400100), the Fundamental Research Funds for the Central Universities, and the Program for Changjiang Scholars and Innovative Research Team in University (no. IRT1221).

References

- [1] L.-D. Chen, Z. Xiong, and S.-Q. Bai, "Recent progress of thermoelectric nano-composites," *Journal of Inorganic Materials*, vol. 25, no. 6, pp. 561–568, 2010.
- [2] Y. Zhang, G. Xu, P. Ren, Z. Wang, and C. Ge, "Effects of various reductants and surfactants on the nanostructure of Bi_2Te_3 synthesized by a hydrothermal process," *Journal of Electronic Materials*, vol. 40, no. 5, pp. 835–839, 2011.
- [3] G. J. Snyder and E. S. Toberer, "Complex thermoelectric materials," *Nature Materials*, vol. 7, no. 2, pp. 105–114, 2008.
- [4] D. Dhak and P. Pramanik, "Characterization of nanocrystalline bismuth telluride (Bi_2Te_3) synthesized by a novel approach through aqueous precursor method," *Journal of the American Ceramic Society*, vol. 89, no. 2, pp. 534–537, 2006.
- [5] R. T. Frost, J. C. Corelli, and M. Balicki, "Reactor irradiation PbTe , Bi_2Te_3 and ZnSb ," *Advanced Energy Conversion*, vol. 2, pp. 77–78, 1962.
- [6] J. Jiang, L. Chen, Q. Yao, S. Bai, and Q. Wang, "Effect of Te14 content on the thermoelectric properties of n-type Bi-Te-Se crystals prepared by zone melting," *Materials Chemistry and Physics*, vol. 92, no. 1, pp. 39–42, 2005.
- [7] B. Poudel, Q. Hao, Y. Ma et al., "High-thermoelectric performance of nanostructured bismuth antimony telluride bulk alloys," *Science*, vol. 320, no. 5876, pp. 634–638, 2008.
- [8] Y. Q. Cao, X. B. Zhao, T. J. Zhu, X. B. Zhang, and J. P. Tu, "Syntheses and thermoelectric properties of $\text{Bi}_2\text{Te}_3/\text{Sb}_2\text{Te}_3$ bulk nanocomposites with laminated nanostructure," *Applied Physics Letters*, vol. 92, no. 14, Article ID 143106, 2008.
- [9] M. Salavati-Niasari, M. Bazarganipour, and F. Davar, "Hydrothermal preparation and characterization of based-alloy Bi_2Te_3 nanostructure with different morphology," *Journal of Alloys and Compounds*, vol. 489, no. 2, pp. 530–534, 2010.
- [10] X. Tang, W. Xie, H. Li, W. Zhao, Q. Zhang, and M. Niino, "Preparation and thermoelectric transport properties of high-performance p-type Bi_2Te_3 with layered nanostructure," *Applied Physics Letters*, vol. 90, no. 1, Article ID 012102, 2007.
- [11] W. Xie, X. Tang, Y. Yan, Q. Zhang, and T. M. Tritt, "Unique nanostructures and enhanced thermoelectric performance of melt-spun BiSbTe alloys," *Applied Physics Letters*, vol. 94, no. 10, Article ID 102111, 2009.
- [12] L.-D. Zhao, B.-P. Zhang, J.-F. Li, M. Zhou, W.-S. Liu, and J. Liu, "Thermoelectric and mechanical properties of nano-SiC-dispersed Bi_2Te_3 fabricated by mechanical alloying and spark plasma sintering," *Journal of Alloys and Compounds*, vol. 455, no. 1–2, pp. 259–264, 2008.
- [13] G. S. Nolas, J. Sharp, and H. J. Goldsmid, *Thermoelectrics: Basic Principles and New Materials Developments*, Springer, New York, NY, USA, 2001.
- [14] J. C. Meyer, A. K. Geim, M. I. Katsnelson, K. S. Novoselov, T. J. Booth, and S. Roth, "The structure of suspended graphene sheets," *Nature*, vol. 446, no. 7131, pp. 60–63, 2007.
- [15] E. R. Margine, M.-L. Bocquet, and X. Blase, "Thermal stability of graphene and nanotube covalent functionalization," *Nano Letters*, vol. 8, no. 10, pp. 3315–3319, 2008.
- [16] D. Dragoman and M. Dragoman, "Giant thermoelectric effect in graphene," *Applied Physics Letters*, vol. 91, no. 20, Article ID 203116, 3 pages, 2007.
- [17] G. Wang, X. Shen, J. Yao, and J. Park, "Graphene nanosheets for enhanced lithium storage in lithium ion batteries," *Carbon*, vol. 47, no. 8, pp. 2049–2053, 2009.
- [18] G. Eda and M. Chhowalla, "Graphene-based composite thin films for electronics," *Nano Letters*, vol. 9, no. 2, pp. 814–818, 2009.
- [19] J. T. Robinson, M. Zalalutdinov, J. W. Baldwin et al., "Wafer-scale reduced graphene oxide films for nanomechanical devices," *Nano Letters*, vol. 8, no. 10, pp. 3441–3445, 2008.
- [20] T. Wei, G. Luo, Z. Fan et al., "Preparation of graphene nanosheet/polymer composites using in situ reduction-extractive dispersion," *Carbon*, vol. 47, no. 9, pp. 2296–2299, 2009.

Research Article

Control of FeAl Composition Produced by SPS Reactive Sintering from Mechanically Activated Powder Mixture

S. Paris,^{1,2} E. Gaffet,² and F. Bernard¹

¹ ICB UMR 6303 CNRS/Université de Bourgogne, 9. Avenue A. Savary, BP 47870, 21078 Dijon Cedex, France

² IJL UMR 7198 CNRS/Université de Lorraine, Parc de Saurupt, CS 50840, 54011 Nancy Cedex, France

Correspondence should be addressed to F. Bernard; fbernard@u-bourgogne.fr

Received 19 February 2013; Revised 7 April 2013; Accepted 13 June 2013

Academic Editor: Claude Estournès

Copyright © 2013 S. Paris et al. This is an open access article distributed under the Creative Commons Attribution License, which permits unrestricted use, distribution, and reproduction in any medium, provided the original work is properly cited.

The effects of mechanically activated powder mixture (Fe + Al) on the microstructure and the chemical composition of FeAl compound produced by reactive sintering implying an exothermic reaction were studied. Firstly, the characteristics of Fe/Al mechanically activated powder mixtures were investigated in terms of their phase composition and microstructure. The high-energy milling allowed the formation of micrometric agglomerates composed of nanometric crystallites of iron and aluminum. Three aggregate sizes class A: $\phi < 125 \mu\text{m}$, class B: $125 \mu\text{m} \leq \phi < 250 \mu\text{m}$, and class C: $\phi \geq 250 \mu\text{m}$ were considered. The latter class enhanced the reactivity of powder mixtures due to an increase of interfaces in contact as an analogy to nanostructured multilayer systems. Interrupted SPS experiments were performed on these mixtures to understand the origin of chemical heterogeneities observed after the reactive sintering. Formation of the intermediate phase Fe_2Al_5 at $\sim 510^\circ\text{C}$ was accompanied by an exothermic reaction and a linear expansion and followed by the formation of small amount of FeAl. The conversion to FeAl was complete at temperatures higher than the melting point of Fe_2Al_5 (1170°C). Finally, a phase evolution between Fe and Al versus the temperature during the reactive sintering is suggested.

1. Introduction

Obtaining dense FeAl compounds with a perfectly controlled microstructure is of interest because of improved hardness and strength but also because of expectations of better ductility and toughness for these intrinsically brittle materials [1]. Techniques for producing ultrafine grained bulk materials have been extensively studied over the last decade [2–9]. They include consolidation from nanostructured milled powder by using conventional hot compaction [2, 3], thermal spraying by different processes such as high velocity oxy-fuel (HVOF) [4–6] as well as the spark plasma sintering (SPS) [7–9]. Prior works reported that SPS was an effective method for the synthesis of monolithic FeAl compounds using powders prepared via ball-milling [10–12]. Consequently, it is crucial to control the microstructure of mechanically activated powder mixtures (called hereafter MAP-mixture) which can be considered as agglomerates composed of nanoreactants. Such MAP-mixtures are reported to be combustion synthesis nanoreactors [13]. Indeed, the combustion front reaction

propagates in individual aggregate from the surface to the core. In addition, this fine multilayers system inside MA-agglomerates allows to improve the combustion synthesis parameters such as an increase of the combustion front velocity (by a factor 3 or 5 in the case of Mo/2Si [14] and of Fe/Al systems, resp. [15]) or decrease the ignition temperature of the exothermic reaction between Fe and Al by 100°C down to about 400°C [16]. However, the decrease of the grain size down to the nanometer scale is not the only pertinent parameter. Indeed, the quality and the size of the exchange surface between reactants are essential, especially when a mechanical pressure is applied during a liquid-solid reaction [17]. Such contacts between particles play a major role in the heat conduction and the kinetics of the reaction. For example, in contrast to combustion synthesis of MAP-mixtures, the reaction from Fe/Al nanostructured powders prepared by evaporation-condensation in cryogenic media [18] leads to the formation of alumina with some minor FeAl compounds [19]. The purpose of this work is to control the characteristics (morphology, structure, chemical

composition, analogy with fine multilayers systems without any mechanical alloyed phases) of mechanically activated powder mixtures. In addition, to understand the origin of the FeAl chemical heterogeneities, SPS-stop experiments (i.e., when the current is switched off) were performed at desired temperatures determined from the SPS shrinkage curve. Consequently, each stage of the synthesis and the consolidation of FeAl by SPS reactive sintering were investigated.

2. Experimental Procedure

The synthesis process to produce dense nanostructured FeAl from elemental powders (Fe + Al) is composed of two steps [20]: (i) mechanical activation of the elemental powder mixture by a short duration treatment in a high energy planetary ball-mill and, (ii) synthesis and densification of FeAl in one step by reactive sintering using SPS equipment.

The Al and Fe reactants are taken in the stoichiometric ratio 53 at.% Fe. 10 g mixture of elemental powders of Al (Cerac, 15–20 μm in particle size, and 99.5% purity) and Fe (Prolabo, 10–15 μm in particle size, and 99.5% purity) was co-milled in confined air via a planetary ball vario-mill Fritsch Pulverisette 4 [22, 23]. Based on previous works [10, 16], a specific ball-milling condition was established at 150 rpm (rotation per minute) for the disk rotation speed, –200 rpm for the absolute vial rotation speed, and 4 h uninterrupted milling duration. The charge ratio C_R (ball to powder mass ratio) was 7. The powders being constituted of quite abrasive materials, a short duration of milling has been selected to avoid any contamination of the product by the milling tools. In fact, in order to limit the powder contamination by the milling tools but also to increase simultaneously the yield of MAP-mixtures, three millings without cleaning milling tools have been carried out. Indeed, under these conditions, the ductile character of powders induced the formation of FeAl coating on the vial surface aging as a protective liner against the abrasion on the surface of tempered steel tools. In addition, the milling parameters were selected to be short to avoid the formation of mechanically induced phases but still sufficiently long for producing MA-agglomerates. In fact, fracture and welding are the two basic events which cause a permanent exchange of matter between particles and ensure a mixing of components at a nanometer scale level [10, 16]. To perform study of the aggregate size effect, two sieves of 125 and 250 μm mesh size were selected in order to prepare three granulometric classes.

Then, these MA-powders were introduced in the SPS apparatus [24] for performing reactive sintering implying an exothermic reaction. The mechanically activated powders were first cold compacted into green body in a cylindrical graphite die lined with graphite foil using a uniaxial pressure of 80 MPa during 2 min. The relative density of the green sample resulting from the cold compaction was about 70%, determined by geometrical measurements. The graphite die containing the cold-compacted sample was set inside the SPS chamber. SPS process is a pressure-assisted pulse-current sintering in which by repeated application of DC pulses, spark point discharges and Joule heating points result in efficient

sintering with low power consumption. The experimental procedure is well detailed elsewhere [11]. A uniaxial pressure of 14 kN (i.e., 70 MPa) was applied both during the reaction and during the cooling. A high DC current was generated, increasing from 0 to 1750 A in 20 s then held at the maximum value for 160 s. Thus, the total duration for applying DC pulse current from the beginning of the heating to the beginning of the cooling is equal to 4 minutes. Temperatures were measured by means of a K-type thermocouple inside a hole located at 3 mm of sample surface. The end-products were typically disks of 18.8 mm in diameter and from 2.2 up to 5.5 mm in height. Before characterization, samples were first polished with 180-grit silicon carbide and down to 1 μm with diamond paste and, finally cleaned in an ultrasonic ethanol bath in order to remove surface contamination from graphite foil. The density of sintered products was evaluated by Archimede's method.

For each “quenched” sample corresponding to SPS stop experiments, a phase and a chemical analysis were carried out, respectively, by X-ray diffraction (XRD) and by scanning electron microscopy (SEM). These quenching means freezing the different stages from shrinkage curve at desired temperatures of the SPS process by shutting off the electric current. X-ray powder diffraction (XRD) measurements were performed using a D5000 Siemens high-resolution diffractometer with a monochromatic Cu-K_β beam ($\lambda = 0.1392 \text{ nm}$) focused with a secondary curved graphite monochromator. Pattern decomposition was achieved by means of the profile-fitting. At the same time, a least-square refinement program was used to determine the cell parameter of reactants. A JEOL 6400F Scanning Electron Microscope (SEM) with a field emission gun (FEG) and coupled with a LINK OXFORD Energy Dispersive X-Ray Spectrometry (EDXS) was used to analyze, respectively, the grain morphology and the local chemical composition of materials. Consequently, MAP-mixtures were embedded and polished whereas dense materials were cut along the axial direction and were embedded in carbon charged resin (Konductomet). A back-scattered electron (BSE) technique was also used to determine the elemental chemical distribution. To estimate the global chemical composition, EDXS measurements were also performed on FeAl products annealed at 950 °C in vacuum during 48 hours in order to get a reference material; these analyses were performed on square surfaces (100 \times 100 μm^2). The chemical composition was determined from 50 measurements. An ICP plasma torch (ICP OES Vista Pro commercialized by Varian) coupled with a Meinhardt nebulizer and cyclonic chambers (200 kPa, 1.3 kW) was also used to check the Fe and Al contents.

3. Results and Discussion

3.1. The MAP-Mixture. The microstructure analysis deduced from XRD, SEM, and ICP experiments of all MAP-mixtures including polydisperse mixture is reported in Table 1. In comparison with the classical mixture (Turbula) composed of micrometer sized grains (10–15 μm and 20 μm for Fe and Al, resp.) [15], the mechanical activation stage allows

TABLE 1: Average characteristics in terms of chemical composition and microstructure parameters (crystallite size, microdistortion level, and lattice parameter) for each class of MAP-mixtures (Fe + Al) in comparison with those obtained by a TURBULA classical mix. $a_{\text{JCPDS Al}} = 0.4049 \text{ nm}$, $a_{\text{JCPDS Fe}} = 0.2866 \text{ nm}$. * Average characteristics $i = \sum(\text{Characteristic } i \times \text{yield of each granulometric class})$. \diamond Grain size given by suppliers.

Characteristics	TURBULA powders	MA powders resulting from the third ball-milling				
		Polydispersity Average*	3rd milling	Seaved—grain-size ranges Φ (μm)		
				Class A < 125	Class B 125–250	Class C ≥ 250
Yield (%)	100%		96%	8 ± 4	17 ± 2	75 ± 03
Chemical composition						
Global—ICP (%at. Fe)	53 ± 1	53 ± 3	53 ± 3	45 ± 3	47 ± 4	55 ± 3
Global—EDXS (%at. Fe)	53 ± 1	53 ± 2	53 ± 2	46 ± 2	49 ± 2	54 ± 1
Microstructure						
Fe						
Crystallite size (nm)	$10\text{--}15 \mu\text{m}^\diamond$	53	50	90 ± 5	67 ± 4	45 ± 3
Microdistortion level (%)		0.13	0.13	0.10	0.12	0.14
Lattice parameter (nm)	0.2866 (3)	0.2867 (1)	0.2867 (2)	0.2866 (9)	0.2867 (4)	0.2868 (3)
Al						
Crystallite size (nm)	$20 \mu\text{m}^\diamond$	70	70	110 ± 7	87 ± 5	62 ± 3
Microdistortion level (%)		0.09	0.08	0.08	0.08	0.09
Lattice parameter (nm)	0.4049 (2)	0.4049 (9)	0.4050 (4)	0.4050 (2)	0.4050 (6)	0.4049 (7)

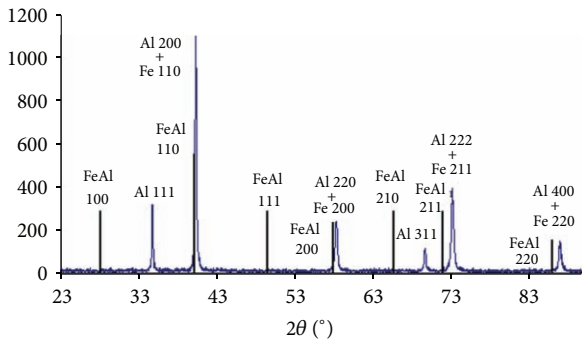


FIGURE 1: X-ray diffraction pattern of Fe/Al MAP-mixtures (theoretical XRD peak position of FeAl phase from ICDD n°01-1257).

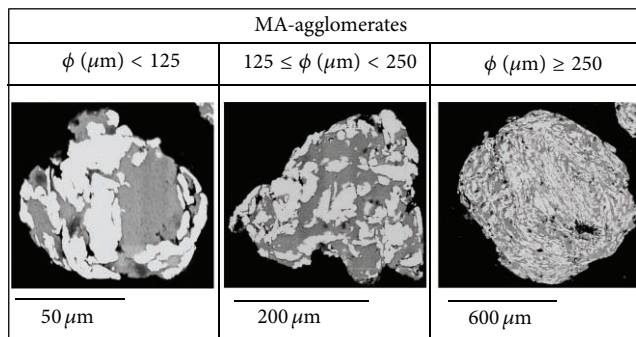


FIGURE 2: SEM (BSE mode) micrographs showing and comparing different morphologies of MAP-mixtures (53 at.% Fe/Al) in function of the granulometry class (P4 (150/–200/4h)). The bright layers and the dark ones are Fe and Al phase, respectively [21].

the formation of micrometer size MA-powders (ranging from $0.4 \mu\text{m}$ up to $800 \mu\text{m}$) constituted of Fe and Al with an average crystallite sizes of 50 nm and 70 nm , respectively.

The size distribution of MAP-mixtures is very wide and may be responsible for some heterogeneity after SPS reactive sintering. Taking into account the detection limit of the apparatus, XRD patterns which performed MAP-mixtures confirm that no mechanical alloyed phase is formed during the milling (Figure 1). In fact, only Fe and Al XRD peaks were observed and any modification of the lattice parameters of these phases was highlighted. The internal microstructure of the MA powders depended on the aggregate size (Figure 2). From chemical composition, microstructure, and structure, the yield of each aggregate size was calculated (Table 1). The yield was improved when the size of MA-powders increased; as an example 75% of MAP-mixtures had larger size than $250 \mu\text{m}$. The size difference can be explained by an activation degree of powder which increases with the agglomerate size. This operation allowed selecting three classes of MA-agglomerates, having different particle sizes: (i) class A: $\phi < 125 \mu\text{m}$, (ii) class B: $125 < \phi < 250 \mu\text{m}$, and (iii) class C: $\phi > 250 \mu\text{m}$. A fourth batch of powder labeled as “polydisperse” was also studied, that is, without any size separation.

From SEM observations of the MA-aggregate cross-sections (Figure 2), it is obvious that the morphology and the microstructure between each class are heterogeneous and may be responsible for the chemical contrast observed in sintered products [10, 12]. Indeed, SEM observations of MA-agglomerates (Figure 2) revealed that the chemical distribution between Fe (white color) and Al (dark color) is different from one type of aggregates to another one. Even after a mechanical activation step, the initial grain size of Fe ($10\text{--}15 \mu\text{m}$) and Al ($20 \mu\text{m}$) is still observed in smaller MA-aggregates (Class A, Figure 2(a)). In addition, concerning the medium MA-agglomerates (Class B, Figure 2(b)), some grains of Fe and Al are slightly elongated and had a thickness in the range of few micrometers. Finally, only large MA-aggregates (i.e., Class C, Figure 2(c)) may be considered

as Fe/Al multilayers. Indeed, this latter is comparable to the Fe/Al diffusion couples. Moreover, a variation of the aggregate morphology inside this lamellar structure can be observed on the larger agglomerate (Class C). The analogy with multilayers structure is improved from the surface to the center of the agglomerate. In comparison to the initial powders, the thickness reduction of Al elongated grains (i.e., layers) is greater than those of Fe especially at the center of aggregates (i.e., ranging from 100 nm to 500 nm). Similar behavior has been reported for other systems such as Al-Cr [25] and Al-Mo [26]. In the center of agglomerate, it can be assumed that the microstructure of the powder particles could not be solved using SEM, since the size of layers has been reduced below 0.2 micrometer. Between the finest multilayers, it is possible to distinguish the presence of a new intermediate color (gray) (Figure 3(a)) that consisted of 53 at.% Fe from chemical analyses (Figure 3(b)). These confirm the well-established Fe/Al diffusion couples, the improvement of powder reactivity, and, therefore, the conversion rate. In fact, according to Fe/Al binary phase diagram [27] and to the schematic diagram showing the possible hierarchy of phase formation in the case of a diffusion couple [28], this interfacial intermediate phase may correspond to an amorphous phase, a Fe or Al rich solid solution, and/or another intermetallic phase like Fe_2Al_5 formed at higher temperature [29]. This latter intermetallic is assumed to form after an annealing of Fe/Al multilayer thin films [30].

From Table 1, the crystallite sizes of reactants are in the nanometric range for both Al and Fe parts. In particular, the crystallite size of Fe (idem for Al) decreases when the size of MA-aggregates increases whereas the Fe microdistortion rate decreases (no evolution is observed for Al). In addition, whatever the granulometry, overestimated value of aluminum amount (70 at.%) was determined. Similar results were obtained for powders mixed during 4 h in Turbula. This difference can be explained by the higher analyzed XRD depth (~ 7 times) of Al (30 μm) in comparison with that of Fe (2.4 μm) for a similar fraction of irradiated area. Nevertheless, as the Fe particles seem to be embedded by an aluminum layer, a careful interpretation is needed. In addition, whatever the granulometry, no contamination (mainly by Cr) from milling tools has been observed (Figure 3(b)). Nevertheless, the global chemical analysis of aggregate shows a significant amount of oxygen (<10 at.%) which increases with the grain size, that is, 5, 7, and 9 at.% for the smallest (Class A), the medium (Class B), and the larger (Class C) agglomerates, respectively. Similar results were reported by Godlewska et al. [31]. However, the origin of the oxygen may be due to the milling atmosphere (confined air) containing oxygen. Nevertheless, these oxides are not detected by XRD (in the detection limit of the apparatus). This study confirms the interest to use high-energy ball-milling without cleaning vials in order to avoid any contamination. Moreover, the formation of passive layer around the micrometric aggregate surface will reduce considerably the reactivity towards ambient air of the isolated nanometric particles allowing storage, transport, and handling.

Although the ball-milling conditions are identical for each granulometric class (P4 (150/–200/4 h), noticeable heterogeneities have been found to appear whatever the scale observation (from macroscopic to microscopic levels) in micrometric Fe/Al MA-aggregates. Transverse observations have shown that aggregates are heterogeneous and that they are responsible for the chemical contrast present on reactive sintered compound. Similar behavior was observed in the case of the Mo/2Si agglomerates [32]. Heterogeneities of Fe/Al aggregates depend on their size. Consequently, the control of the MA-aggregates features (chemical composition, microstructure, intergranular porosity, etc.) is crucial in order to elaborate intermetallic compounds with expected properties. Such a result is emphasized because Fe/Al MA-aggregates can be considered as combustion synthesis nanoreactors [13]. To adjust the specific characteristics of MA-aggregates for expected foreseen applications, it is necessary to understand the origin of such heterogeneities. A similar behavior, that is, the observation of heterogeneous micrometric aggregates composed of nanostructured reactants was already reported in the case of the production of items from cold-rolling process [33]. A nanometer size multilayers system and the chemical homogeneity are obtained when the number of cycle is increased and when the mechanical pressure is higher. Consequently, it is possible to assume that the difference of MA-aggregate characteristics must be due to a modification of plastic deformation mechanism during the ball-milling process [34, 35]. In MA techniques, the repeated fracture-welding process results in an intimate mixture of the two constituents with a concomitant increase of the defect concentration and strain in the mixture. In the case of ductile-ductile powder mixture (such as Fe/Al system), milling refines the grain size further to a lamellar structure and even greater number of defects are introduced [36–38]. Ball-milling conditions have an influence on the nature and, also on the concentration of defects and, consequently on the chemical homogeneity. High energy planetary ball-mill (especially pulverisette P4), in which the rotation speeds of vials and the plate can be selected independently, allows extending the milling investigation for producing powders with the desired characteristics [39–44]. Oleszak and Shingu [34] reported that the shape of agglomerates with different chemical composition from 50 to 100 at.% Fe is more regular when the milling duration is prolonged. According to El-Eskandarany et al. [45], the large distribution of the MA-aggregates size indicates that the growth mechanism of aggregates to obtain powders with optimal characteristics is not complete. It can be stipulated that the heterogeneity can be due to a difference of co-milling effective duration. Milling injects an additional energy to the reactant system in the form of the interfacial and strain energies and effectively lowers the activation barriers. In fact, in a few minutes to one hour, the lamellar spacing (Figure 3(a)) usually becomes small (few micrometers) and the crystallite size is refined to nanometric dimensions. Moreover, the presence of structural defects (i.e., dislocations, vacancies, stacking faults, grain boundaries, etc.) enhances the diffusivity of dissolved elements into the matrix. Additionally, the slight temperature increase during milling

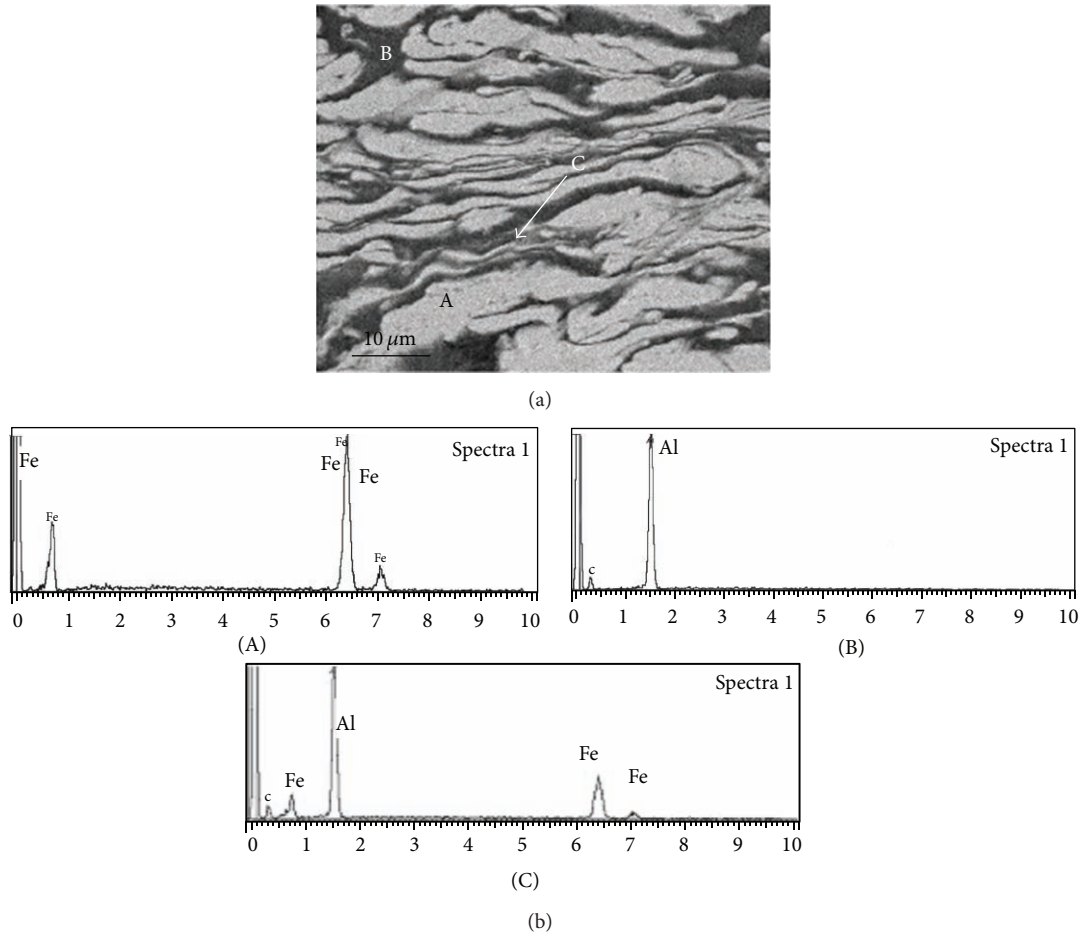


FIGURE 3: (a) BSE micrographs showing the transverse cut of coarser agglomerates (class C) to reveal the multilayer structure in each MAP-mixtures. The bright layers (A) are Fe phase, and the dark ones (B) are Al phase. Between the finest multilayers (A and B), a layer with an intermediate color (C) is observed and corresponds to a mix of Fe and Al. The EDX spectra of each contrasted layer (A, B, and C) are reported in (b).

	Class A- ϕ (μm) < 125	Class B- $125 \leq \phi$ (μm) < 250	Class C- ϕ (μm) ≥ 250
Corresponding SPS products			

FIGURE 4: SEM (BSE mode) micrographs of products synthesized by SPS. These are performed on the transverse cut of each of them. The bright layers and the dark ones are Fe and Al phase in the agglomerates, respectively. Contrast of brightness is characteristic of the heterogeneity such as brighter area which can correspond to higher % at. Fe content.

supports the diffusion and, consequently, a true alloying takes place among the constituent elements.

3.2. SPS Reactive Sintering. These MAP-mixtures were introduced in the SPS apparatus for performing reactive sintering according to conditions previously described. The control of the SPS processing parameters has been found to allow

the formation of a dense FeAl compound (close to 99%) forming a microstructure with nanosized coherently diffracting domains [12]. TEM analyses have been found to reveal that the nanoorganization, especially the nanosize of the coherently diffracting domain size, was due to dislocation networks [12]. The beneficial effect of the SPS process on the densification was demonstrated elsewhere [11] showing

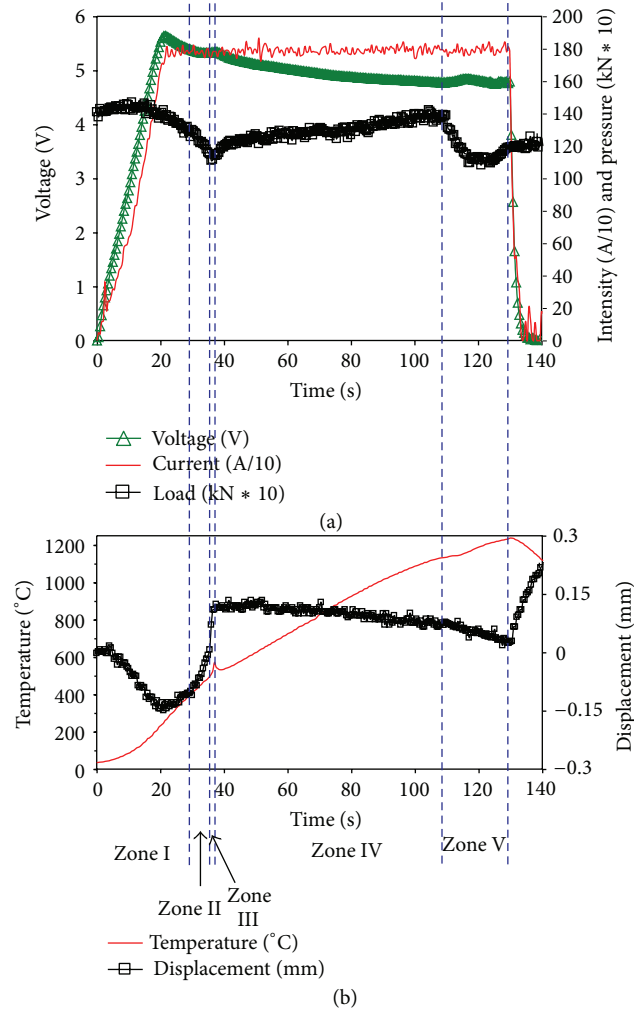


FIGURE 5: Evolutions of (a) the voltage (V), intensity ($I/10$) and pressure ($kN \times 10$) and of (b) the temperature (T) and the displacement versus the time of a sample sintered at 1750 A and 70 MPa.

that the relative density increased with the heating rate, the applied pressure, and the holding time up to a critical value. SEM observations (Figure 4) of the sintered sample showed clearly the presence of heterogeneous chemical compositions which differ versus MA-agglomerate size. In order to explain the origin of these heterogeneities, SPS-stop experiments were carried out using only larger MA-agglomerates (Class C) in which the chemical contrast seems to be stronger and also closer to expected FeAl stoichiometry (53% at. Fe, Table 1). Figure 5(a) presents the evolution of SPS processing parameters versus the time during the reactive sintering from Fe + Al. In addition, as presented in Figure 5(b). From a fine analysis of such curves associated to reaction mechanisms, it is possible to describe the different sintering stages of the process leading to the formation of FeAl during a reactive sintering implying an exothermic reaction, that is, temperatures at which expansion and phase transformation take place. Such analysis allows selecting “interesting” temperatures that is performing SPS “stop.” From Figure 5, five distinct successive stages can be highlighted labeled as zones I to V. XRD patterns from the SPS end-products quenched

from different temperatures are presented in Figure 6. The corresponding microstructure contrast due to the difference in chemical composition is presented in Figure 7. The phase identification deduced from XRD characterization analysis and the chemical composition determined by EDX are also reported. It can be clearly stated that the nature of the phases determined by XRD (Figure 6) and microstructure observed by SEM (Figure 7) change versus the temperature. For describing all stages of the reactive sintering in the Fe/Al system, the linear expansion (deduced from Figure 5(b)) and the relative density evolutions were plotted versus the temperature (Figure 8).

In Zone I, as can be observed (Figure 8), the displacement increases slowly from the room temperature to 400°C. A SPS-stop experiment carried out at 350°C revealed the absence of chemical interaction. The sample contained only Fe (bright layers) and Al (dark layers) like the initial green sample which is validated by the XRD analysis (Figure 6(b)). This confirms that no significant reaction occurs from RT up to 400°C. Consequently, the slight expansion in Zone I was caused by the thermal expansion of particles, die, and gas.

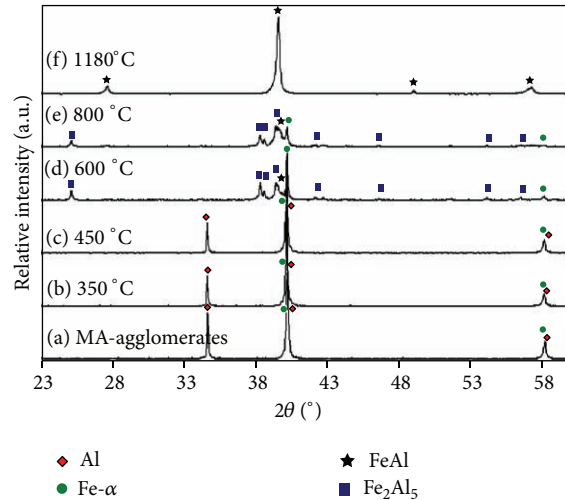


FIGURE 6: X-ray diffraction patterns (from (b) to (f)) versus temperature for quenched specimens to room temperature.

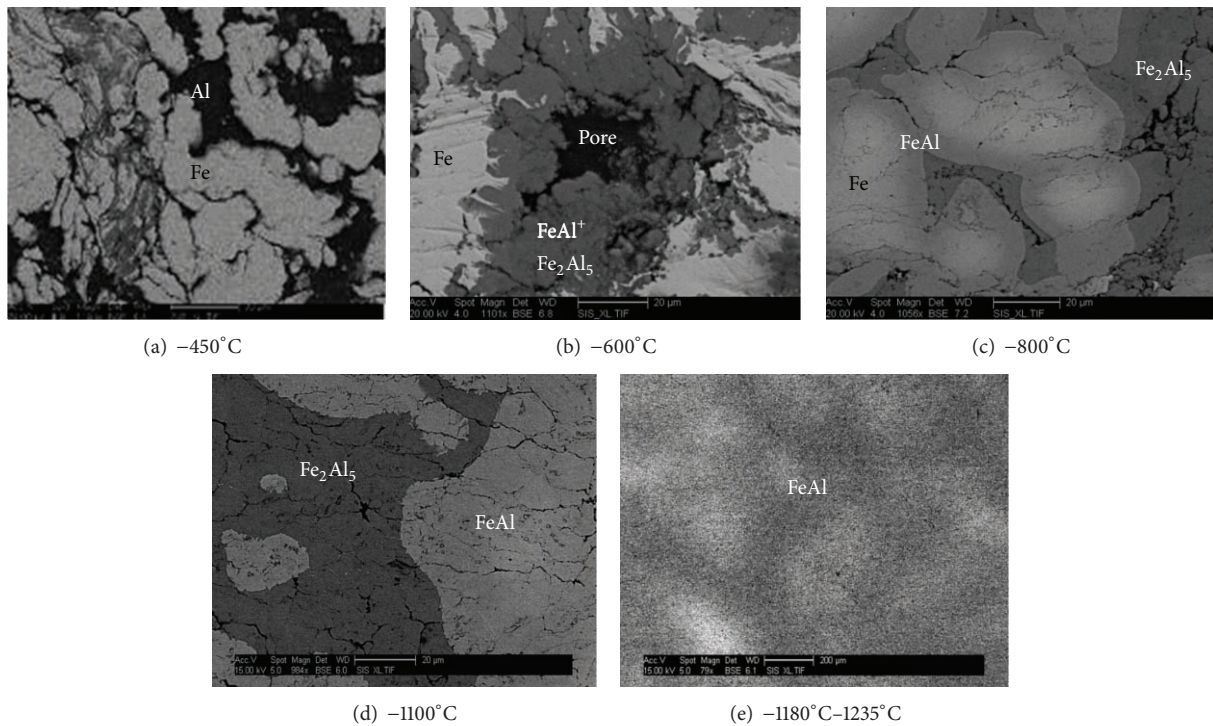


FIGURE 7: SEM (BSE mode) micrographs showing and comparing microstructure of samples quenched from different temperatures. Temperatures are characteristics of each zone relative to the reaction sequence of FeAl formation determined from the evolutions of the XRD patterns curves (Figure 6).

In Zone II, from 400 °C to 500 °C, a slight shrinkage of the sample is observed (Figure 8(a)).

At 450 °C, for the sample quenched from 450 °C, an intermediate color can be observed at the Fe(s)/Al(s) interfaces (Figure 7(a)). Using energy dispersive spectroscopy (EDS), the dark gray phase surrounded by iron gets an atomic percent Fe equal to $\sim 30 \pm 2$. This latter can be identified as an amorphous or crystallized intermetallic phase rich in Al (such as Fe_2Al_5 according to the Fe-Al phase diagram [27])

and/or as a solid solution of Fe(Al) or Al(Fe). In particular, Thompson [46] has pointed out that an interdiffusion is necessary between pure components at the interface before the nucleation of any intermetallic compound. In addition, it was reported [21] that at temperatures below 300 °C, the interdiffusion of Fe in f.c.c Al is faster for Al-Fe diffusion couple. Above this temperature, the diffusion behavior is opposite; that is, interdiffusion of Al in b.c.c. Fe is faster. From calculated free energy at 450 °C, intermetallic compound can

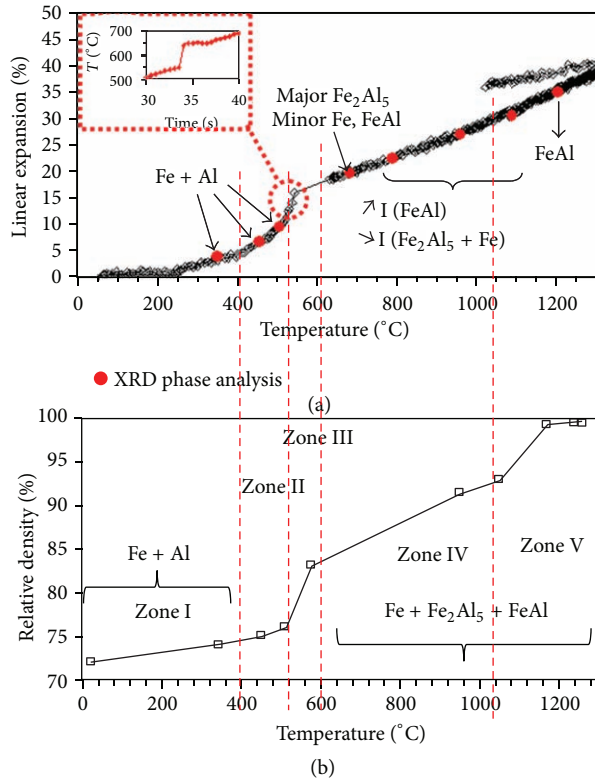


FIGURE 8: Evolution of (a) of the linear expansion during a SPS reactive sintering from Fe + Al mixture. Red points correspond to XRD phase analysis presented in Figure 6. A zoom of the temperature profile showing the fast increase of the temperature characteristic of the exothermic reaction is inset. (b) Dependence of relative density of interrupted sample, that is, of the different phases (detected by XRD from Figure 6), as a function of temperature. In addition, five zones in agreement with Figure 5 are presented.

nucleate within the aluminum solid solution [47]. However, the amount of solute content (Fe) in solid solution of Al is too small to be detected.

In Zone III, a sharp temperature elevation ($3780^{\circ}\text{C}\cdot\text{min}^{-1}$) from 500°C to 600°C is observed simultaneously as a significant shrinkage which is validated by the faster stage of densification (Figure 8). These evolutions are characteristics of the exothermic reaction occurring between Fe and Al powders. This latter is confirmed by X-ray analysis which shows the presence of an unreacted Fe and the formation of the aluminum rich Fe_2Al_5 (Figure 6(d)) and of a minor amount of FeAl. The formation of Fe_2Al_5 is detectable only from 600°C whereas it can exist at lower temperature. As previously observed, the dark gray phase is confirmed as Fe_2Al_5 ($\sim 30\text{at. Fe}$). The intermetallic compound is formed around the partially unreacted Fe particle (bright layer). The interface between the Fe_2Al_5 layer and Fe grain is irregular due to the tongue-like morphology of the Fe_2Al_5 layer. Similar morphology was observed during dipping solid Fe in liquid aluminum [48, 49]. It can be concluded that at this stage, despite the fact that melting point of Al was not reached (660°C), aluminum has totally reacted to form iron aluminide and left behind large pores (Figure 7(b)) certainly due to

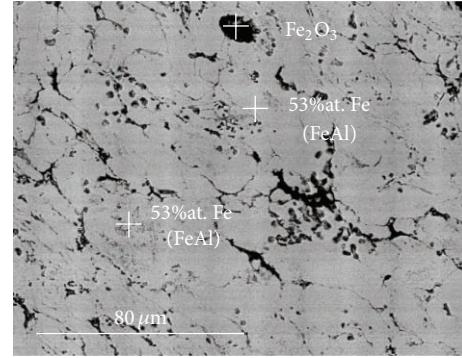


FIGURE 9: SEM (BSE mode) micrographs of a homogeneous single phase FeAl after thermal treatment (1000°C , 30 min) on sample containing Fe + Fe_2Al_5 + FeAl phases presented in Figures 6(e) and 7(c).

a local temperature higher than measured temperature. As reported by different authors [29], the reaction demonstrated to be always accompanied by an expansion of the sample due to the solid state exothermic reaction $2\text{Fe(s)} + 5\text{Al} \Rightarrow \text{Fe}_2\text{Al}_5$ which occurred at $\sim 560\text{--}565^{\circ}\text{C}$.

Then, in Zone IV from 600°C to 1100°C , it can be seen that the amount of FeAl increases on the expense of Fe_2Al_5 and Fe (Figure 6(e)). These observations are confirmed by high resolution SEM images (Figure 7(c)). Three uniform well-distinguished phases which differ in contrast can be observed. However the amount of FeAl is very small even after the second reaction. The EDS analysis obtained from these regions indicate that between Fe (bright grain) and aluminum rich Fe_2Al_5 there is another layer (light grey layers) exhibiting narrow morphology rings with Fe concentration much higher (55% at.) than expected in Fe_2Al_5 (Figure 7). These may be the rings of the aggregates. These layers are believed to be consisting of FeAl or a mixture of FeAl with Fe or Fe_2Al_5 . At higher temperature (1100°C), according to SEM analysis (Figure 7(d)), the amounts of Fe_2Al_5 and Fe still decrease whereas the quantity of FeAl increases. Such observations can be explained from diffusion couple of species. As reported by Maitra and Gupta [30] during the formation of FeAl, the microstructure of the diffusion couple has revealed that exist two Kirkendall planes: one at the Fe/FeAl interface and, the other at the FeAl/ Fe_2Al_5 interface on the Fe_2Al_5 side. For the Kirkendall plane at Fe/FeAl interface, it can be inferred that Fe diffused faster ($\sim 10^4$) than Al in the Fe-rich part of FeAl. A similar conclusion can be drawn for the other Kirkendall plane in agreement with the diffusivity values [50]. These observations are confirmed from activation energy for the growth of the FeAl layer. The activation energy for the growth of the FeAl layer is larger ($180\text{ kJ}\cdot\text{mol}^{-1}$) than that for the diffusion of iron atoms into Fe_2Al_5 ($141\text{ kJ}\cdot\text{mol}^{-1}$) and is smaller than that for the diffusion of aluminum atoms into FeAl ($340\text{ kJ}\cdot\text{mol}^{-1}$) [51]. It was identified that the growth of all intermetallic layers was controlled by the diffusion of Fe atoms into the Al-rich intermetallic layers [52]. The growth of the FeAl layer was likely controlled by the diffusion of iron atoms into the Fe_2Al_5 layers.

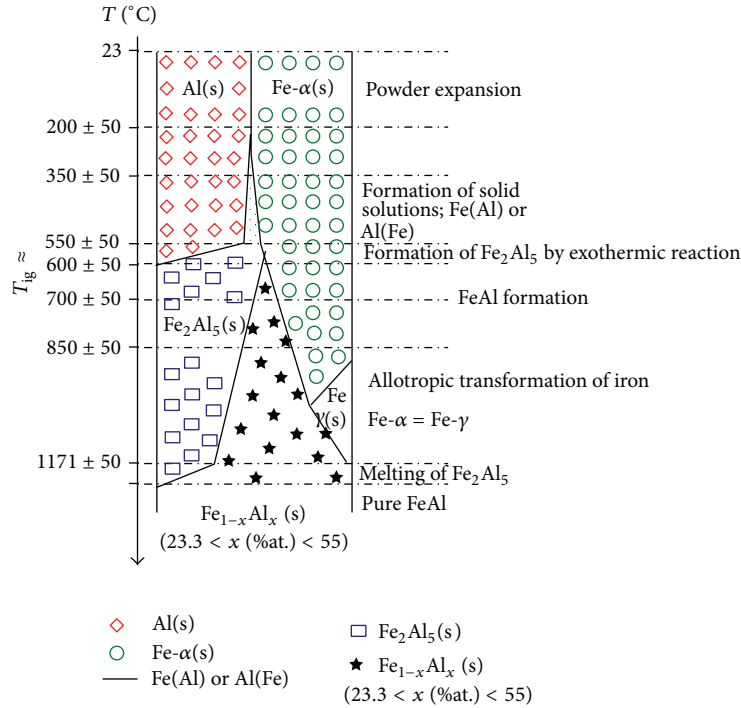


FIGURE 10: Phase evolution from Fe/Al MAP-mixtures for producing pure FeAl compound by reactive sintering.

Finally, in Zone V from 1100°C to 1235°C, the evolution of the SPS curves corresponds to the formation of FeAl. At 1180°C, only XRD peaks of FeAl are observed (Figure 6(f)). FeAl compound was formed to exhibit a micrometric grain size ranging from 1 to 6 μm [12]. Nevertheless, from the observation of BSE micrograph, whereas the previous areas corresponding to Fe and Fe_2Al_5 disappear, a modulation of contrast can be clearly observed (Figure 7(e)). Such observations can be explained by the chemical contrast present at the submillimeter-scale (EDX) [10, 11] with a variability of Al content in the range of 36–47%. The specificities can be introduced by the melting of Fe_2Al_5 at 1171°C according to the Fe-Al phase diagram [27]. Hence, the melting of Fe_2Al_5 allows a faster shrinkage and leads to a fully dense compound; that is, the density of the compact reaches 99.5% TD. No macroporosity can be observed in SEM image (Figure 7(e)) which is confirmed from Hg porosimetry analysis, and no open porosity was detected. It is obvious that hot pressure applied during SHS allows full-densification of material.

To confirm the role of Fe_2Al_5 in the formation of FeAl, an additional experiment was performed on the sample quenched from 800°C in order to get FeAl from solid state reaction between $\text{Fe}_{(s)}/\text{Fe}_2\text{Al}_{5(s)}/\text{FeAl}_{(s)}$ phases. The sample was heated for 30 min at 1000°C, below the melting point of Fe_2Al_5 . Compared to previous FeAl compounds formed, a single phase material (with pores) was formed (Figure 9) with 94% relative density. After polishing of the sample to eliminate oxide layers, local phase analysis (EDS) on several zones showed that the sample composition is homogeneous and corresponds to the expected composition (53 at.% Fe, Figure 9). Characteristics are consistent with those obtained by Gedevisashvili and Deevi [29] at 900°C. Homogeneous

FeAl compounds can be formed via a solid state reaction. Consequently, it is expected that the new FeAl phase formed during the melting of Fe_2Al_5 has a different formation mechanisms than the FeAl synthesized at lower temperature. This study confirms the necessity on the one hand, to follow the evolutions of the phase nature and of their respective domains of composition and, on the other hand, to understand the sequence of phase formation, the interface type, the morphology of interfaces, and the growth mechanism. Thus, it is possible to suggest a reaction mechanism for producing pure FeAl (Figure 10). Whatever the SPS conditions, the formation of FeAl occurred in three steps: the formation of a solid solution Fe (Al) followed by a solid state reaction of Fe_2Al_5 to the interfaces of Fe(s)/Al(s) and, then FeAl. Nevertheless, it is not possible to conclude the fact that such reactions are competitive or successive. The formation of Fe_2Al_5 is prejudicial to elaborate dense FeAl in one step from Al liquid phase [15]. To limit the reaction duration, it is necessary to go through the melting of Fe_2Al_5 . This latter phase, combined to the presence of Fe(s), is responsible for the original characteristics of the FeAl compounds. In agreement with others intermetallics, an increase of the heating rate will reduce the duration of precombustion reaction and, consequently the formation of Fe_2Al_5 . A higher heating rate will promote Fe-solid-Al-liquid reaction which results in the production of pure nanostructured FeAl compounds [53] whereas the presence of Fe_2Al_5 leads to a stoichiometry gap. Consequently, the heterogeneous characteristics of MA-agglomerates according to their size which are considered as SHS microreactors reinforce the obligation of their check. They are responsible for the FeAl chemical heterogeneities which depend on the reaction path.

4. Conclusion

This study gives a fine description of the formation of Fe/Al MA-agglomerates using a high energy planetary ball-mill. It has been demonstrated that mechanical activation resulted in the formation of micrometer size aggregates composed of nanostructured Fe/Al multilayers with heterogeneous characteristics themselves. These latter are responsible for the heterogeneous characteristics of the subsequent dense “nanostructured” FeAl compounds synthesized by SPS reactive sintering. A system presenting an “ideal” nanometer size multilayer system is obtained when the larger aggregates are formed. Consequently, for this ball-milling conditions, that is, P4 (150/–200/4 h), the optimal mixture resulted from the 3rd ball-milling without cleaning tools and had the coarsest studied granulometry ($\phi \geq 250 \mu\text{m}$, i.e., Class C). In addition, it is essential for each agglomerate size to adapt reactive sintering parameters for limiting FeAl chemical heterogeneities.

The dense FeAl intermetallics synthesized via a mechanically activated reactive sintering process have been shown to exhibit some chemical heterogeneity. To produce FeAl materials with perfectly controlled characteristics, the sequences of phases formed during the sintering of MAP-mixtures (Fe + Al) were identified by X-ray diffraction, scanning electron microscopy back scattered electrons coupled with energy dispersive X-ray spectrometry, and density measurements. The results were correlated to the temperature profile and the shrinkage curve occurring during flash sintering. It was found that the formation of the intermediate phase Fe_2Al_5 at $\sim 510^\circ\text{C}$ was associated with an exothermic reaction and a linear expansion and followed by the formation of small amount of FeAl. The conversion to nanoorganized FeAl is complete at higher temperatures than the melting point of Fe_2Al_5 (1170°C). The formation of two types of iron aluminide intermetallics. (i.e., with distinct reaction mechanisms) seems to be at origin of the FeAl specificities. Consequently, it is essential to limit the formation of Fe_2Al_5 by solid state reaction and to promote the direct reaction between Fe(s) and Al(l) by a control of the mechanical activation and reactive sintering conditions.

Acknowledgment

The authors acknowledge the financial support of the “Ministère de l’Enseignement Supérieur et de la Recherche.”

References

- [1] D. G. Morris and M. A. Morris-Muñoz, “The influence of microstructure on the ductility of iron aluminides,” *Intermetallics*, vol. 7, no. 10, pp. 1121–1129, 1999.
- [2] M. A. Morris-Muñoz, A. Dodge, and D. G. Morris, “Structure, strength and toughness of nanocrystalline FeAl,” *Nanostructured Materials*, vol. 11, no. 7, pp. 873–885, 1999.
- [3] L. D’Angelo, L. D’Onofrio, and G. Gonzalez, “Nanophase intermetallic FeAl obtained by sintering after mechanical alloying,” *Journal of Alloys and Compounds*, vol. 483, no. 1-2, pp. 154–158, 2009.
- [4] T. Grosdidier, H. L. Liao, S. Lenhard, A. Tidu, and S. Revol, “Processing and characterisation of nanocrystalline iron aluminide coatings prepared by thermal spraying of milled powders,” *Journal de Physique I*, vol. 11, pp. 11–18, 2001.
- [5] J. Gang, J.-P. Morniroli, and T. Grosdidier, “Nanostructures in thermal spray coatings,” *Scripta Materialia*, vol. 48, no. 12, pp. 1599–1604, 2003.
- [6] G. Ji, T. Grosdidier, and J. P. Morniroli, “Microstructure of a high-velocity oxy-fuel thermal sprayed nanostructured coating obtained from milled powder,” *Metallurgical and Materials Transactions A*, vol. 38, no. 10, pp. 2455–2463, 2007.
- [7] T. Grosdidier, G. Ji, F. Bernard, E. Gaffet, Z. A. Munir, and S. Launois, “Synthesis of bulk FeAl nanostructured materials by HVOF spray forming and spark plasma sintering,” *Intermetallics*, vol. 14, no. 10-11, pp. 1208–1213, 2006.
- [8] G. Ji, T. Grosdidier, F. Bernard, S. Paris, E. Gaffet, and S. Launois, “Bulk FeAl nanostructured materials obtained by spray forming and spark plasma sintering,” *Journal of Alloys and Compounds*, vol. 434-435, pp. 358–361, 2007.
- [9] T. Skiba, P. Haušild, M. Karlík, K. Vanmeensel, and J. Vleugels, “Mechanical properties of spark plasma sintered FeAl intermetallics,” *Intermetallics*, vol. 18, no. 7, pp. 1410–1414, 2010.
- [10] S. Paris, C. Valot, L. Gosmain, E. Gaffet, F. Bernard, and Z. Munir, “Investigation of mechanically activated field-activated pressure-assisted synthesis processing parameters for producing dense nanostructured FeAl,” *Journal of Materials Research*, vol. 18, no. 10, pp. 2331–2338, 2003.
- [11] S. Paris, E. Gaffet, F. Bernard, and Z. A. Munir, “Spark plasma synthesis from mechanically activated powders: a versatile route for producing dense nanostructured iron aluminides,” *Scripta Materialia*, vol. 50, no. 5, pp. 691–696, 2004.
- [12] G. Ji, D. Goran, F. Bernard, T. Grosdidier, E. Gaffet, and Z. A. Munir, “Structure and composition heterogeneity of a FeAl alloy prepared by one-step synthesis and consolidation processing and their influence on grain size characterization,” *Journal of Alloys and Compounds*, vol. 420, no. 1-2, pp. 158–164, 2006.
- [13] A. S. Rogachev, N. A. Kochetov, V. V. Kurbatkina et al., “Microstructural aspects of gasless combustion of mechanically activated mixtures. I. High-speed microvideorecording of the Ni-Al composition,” *Combustion, Explosion and Shock Waves*, vol. 42, no. 4, pp. 421–429, 2006.
- [14] C. Gras, D. Vrel, E. Gaffet, and F. Bernard, “Mechanical activation effect on the self-sustaining combustion reaction in the Mo-Si system,” *Journal of Alloys and Compounds*, vol. 314, no. 1-2, pp. 240–250, 2001.
- [15] F. Charlot, F. Bernard, E. Gaffet, D. Klein, and J. C. Niepce, “In situ time-resolved diffraction coupled with a thermal I.R. camera to study mechanically activated SHS reaction: case of Fe-Al binary system,” *Acta Materialia*, vol. 47, no. 2, pp. 619–629, 1999.
- [16] F. Charlot, E. Gaffet, B. Zeghmati, F. Bernard, and J. C. Niepce, “Mechanically activated synthesis studied by X-ray diffraction in the Fe-Al system,” *Materials Science and Engineering A*, vol. 262, no. 1-2, pp. 279–288, 1999.
- [17] D. E. Alman and N. S. Stoloff, “Powder fabrication of monolithic and composite NiAl,” *International Journal of Powder Metallurgy*, vol. 27, no. 1, pp. 29–41, 1991.
- [18] Y. Champion and J. Bigot, “Synthesis and structural analysis of aluminum nanocrystalline powders,” *Nanostructured Materials*, vol. 10, no. 7, pp. 1097–1110, 1998.
- [19] F. Charlot, *Etude et compréhension des réactions auto-entretenuées activées mécaniquement. Elaboration du composé FeAl*

- nanostructuré [Ph.D. thesis]*, Université de Bourgogne, Dijon, France, 1999.
- [20] Z. A. Munir, F. Charlot, F. Bernard, and E. Gaffet, "One-step synthesis and consolidation of nano-phase materials," U.S. Patent, no. 6, 200, 515, March 2001.
- [21] S. R. Teixeira, P. H. Dionisio, E. F. da Silveria, F. L. Freire Jr., W. H. Schreiner, and I. J. R. Baumvol, "Interdiffusion and reaction in the FeAl bilayer: I: rutherford backscattering analysis of furnace-annealed samples," *Materials Science and Engineering*, vol. 96, pp. 267–277, 1987.
- [22] M. Abdellaoui, T. Barradi, and E. Gaffet, "Mechanism of mechanical alloying phase formation and related magnetic and mechanical properties in the FeSi system," *Journal of Alloys and Compounds*, vol. 198, no. 1-2, pp. 155–164, 1993.
- [23] M. Abdellaoui and E. Gaffet, "The physics of mechanical alloying in a planetary ball mill: mathematical treatment," *Acta Metallurgica et Materialia*, vol. 43, no. 3, pp. 1087–1098, 1995.
- [24] M. Tokita, "Trends in advanced spark plasma sintering systems and technology. Functionally gradient materials and unique synthetic processing methods from next generation of powder technology," *Journal of Japan Society Powder Technology*, vol. 30, pp. 790–804, 1993.
- [25] K. F. Kobayashi, N. Tachibana, and P. H. Shingu, "Formation of amorphous Al-Cr alloys by mechanical alloying of elemental aluminium and chromium powders," *Journal of Materials Science*, vol. 25, no. 7, pp. 3149–3154, 1990.
- [26] M. V. Zdujic, K. F. Kobayashi, and P. H. Shingu, "Structural changes during mechanical alloying of elemental aluminium and molybdenum powders," *Journal of Materials Science*, vol. 26, no. 20, pp. 5502–5508, 1991.
- [27] O. Kubaschewski, *IRON-Binary Phase Diagrams*, Springer, 1986.
- [28] D. L. Zhang and D. Y. Ying, "Solid state reactions in nanometer scaled diffusion couples prepared using high energy ball milling," *Materials Science and Engineering A*, vol. 301, no. 1, pp. 90–96, 2001.
- [29] S. Gedevisashvili and S. C. Deevi, "Processing of iron aluminides by pressureless sintering through Fe+Al elemental route," *Materials Science and Engineering A*, vol. 325, no. 1-2, pp. 163–176, 2002.
- [30] T. Maitra and S. P. Gupta, "Intermetallic compound formation in Fe-Al-Si ternary system—part II," *Materials Characterization*, vol. 49, no. 4, pp. 293–311, 2002.
- [31] E. Godlewska, S. Szczepanik, R. Mania, J. Krawiarz, and S. Koziński, "FeAl materials from intermetallic powders," *Intermetallics*, vol. 11, no. 4, pp. 307–312, 2003.
- [32] G. Cabouro, S. le Gallet, S. Chevalier, E. Gaffet, Y. Grin, and F. Bernard, "Dense Mosi_2 produced by reactive flash sintering: control of Mo/Si agglomerates prepared by high-energy ball milling," *Powder Technology*, vol. 208, no. 2, pp. 526–531, 2011.
- [33] J. H. Perepezko, R. J. Hebert, and G. Wilde, "Synthesis of nanostructures from amorphous and crystalline phases," *Materials Science and Engineering A*, vol. 375–377, no. 1-2, pp. 171–177, 2004.
- [34] D. Oleszak and P. H. Shingu, "Mechanical alloying in the FeAl system," *Materials Science and Engineering A*, vol. 181-182, pp. 1217–1221, 1994.
- [35] E. Hellstern, H. J. Fecht, Z. Fu, and W. L. Johnson, "Structural and thermodynamic properties of heavily mechanically deformed Ru and AlRu," *Journal of Applied Physics*, vol. 65, no. 1, pp. 305–310, 1989.
- [36] P. Baláž, M. Achimovičová, M. Baláž et al., "Hallmarks of mechanochemistry: from nanoparticles to technology," *Chemical Society Reviews*, 2013.
- [37] C. Suryanarayana, "Mechanical alloying and milling," *Progress in Materials Science*, vol. 46, no. 1-2, pp. 1–184, 2001.
- [38] E. Gaffet and F. Bernard, "Mechanically activated powder metallurgy processing: a versatile way towards nanomaterials synthesis," *Annales de Chimie: Science des Matériaux*, vol. 27, no. 6, pp. 47–59, 2002.
- [39] E. Gaffet and G. le Caër, "Mechanical processing for nanomaterials," in *Encyclopedia of Nanoscience and Nanotechnology*, H. S. Nalwa, Ed., vol. 5, pp. 91–129, American Scientific Publishers, 2004.
- [40] E. Gaffet, "Planetary ball-milling: an experimental parameter phase diagram," *Materials Science and Engineering A*, vol. 132, pp. 181–193, 1991.
- [41] E. Gaffet, "Dynamic equilibrium induced by ball milling in the NiZr system," *Materials Science and Engineering A*, vol. 119, pp. 185–197, 1989.
- [42] E. Gaffet, "Ball milling: an $E-v-T$ parameter phase diagram," *Materials Science and Engineering A*, vol. 135, pp. 291–293, 1991.
- [43] S. Vives, E. Gaffet, and C. Meunier, "X-ray diffraction line profile analysis of iron ball milled powders," *Materials Science and Engineering A*, vol. 366, no. 2, pp. 229–238, 2004.
- [44] O. Boytsov, A. I. Ustinov, E. Gaffet, and F. Bernard, "Correlation between milling parameters and microstructure characteristics of nanocrystalline copper powder prepared via a high energy planetary ball mill," *Journal of Alloys and Compounds*, vol. 432, no. 1-2, pp. 103–110, 2007.
- [45] M. S. El-Eskandarany, K. Aoki, and K. Suzuki, "Solid state formation of Al-TM (TM: Ti, Zr, Nb and Ta) amorphous alloys by mechanical rod milling, mechanical alloying," *Materials Science Forum*, vol. 88–90, pp. 81–88, 1992.
- [46] C. V. Thompson, "On the role of diffusion in phase selection during reactions at interfaces," *Journal of Materials Research*, vol. 7, no. 2, pp. 367–373, 1992.
- [47] P. Bhattacharya, K. N. Ishihara, and K. Chattopadhyay, "FeAl multilayers by sputtering: heat treatment and the phase evolution," *Materials Science and Engineering A*, vol. 304–306, no. 1-2, pp. 250–254, 2001.
- [48] J.-M. Lee, S.-B. Kang, T. Sato, H. Tezuka, and A. Kamio, "Evolution of iron aluminide in Al/Fe in situ composites fabricated by plasma synthesis method," *Materials Science and Engineering A*, vol. 362, no. 1-2, pp. 257–263, 2003.
- [49] K. Bouché, F. Barbier, and A. Coulet, "Intermetallic compound layer growth between solid iron and molten aluminium," *Materials Science and Engineering A*, vol. 249, no. 1-2, pp. 167–175, 1998.
- [50] E. A. Brande, Ed., *Smithells Metals Reference Book*, Butterworth, 1983.
- [51] H. Bakker and H. Mehrer, Eds., *Diffusion in Solid Metals and Alloys*, vol. 26 of *Numerical Data and Functional Relationship in Science and Technology*, Springer, 1990.
- [52] S. Kobayashi and T. Yakou, "Control of intermetallic compound layers at interface between steel and aluminum by diffusion-treatment," *Materials Science and Engineering A*, vol. 338, no. 1-2, pp. 44–53, 2002.
- [53] F. Bernard, F. Charlot, E. Gaffet, and Z. A. Munir, "One-step synthesis and consolidation of nanophase iron aluminide," *Journal of the American Ceramic Society*, vol. 84, no. 5, pp. 910–914, 2001.

Research Article

Reactive Spark Plasma Sintering: Successes and Challenges of Nanomaterial Synthesis

Dina V. Dudina¹ and Amiya K. Mukherjee²

¹ Institute of Solid State Chemistry and Mechanochemistry SB RAS, Kutateladze Street 18, Novosibirsk 630128, Russia

² Department of Chemical Engineering and Materials Science, University of California, Davis, 1 Shields Avenue, Davis, CA 95616, USA

Correspondence should be addressed to Dina V. Dudina; dinal807@gmail.com

Received 21 February 2013; Accepted 4 June 2013

Academic Editor: Izabel Fernanda Machado

Copyright © 2013 D. V. Dudina and A. K. Mukherjee. This is an open access article distributed under the Creative Commons Attribution License, which permits unrestricted use, distribution, and reproduction in any medium, provided the original work is properly cited.

Spark plasma sintering (SPS), initially developed as an advanced sintering technique for consolidating nanopowders into nanostructured bulk materials, has been recently looked at in much broader perspective and gained a strong reputation of a versatile method of solid state processing of metals, ceramics, and composites. The powders in the SPS-dies experience the action of pulsed electric current and uniaxial pressure; they are heated at very high rates unachievable in furnace heating and sintered within shorter times and at lower temperatures than in conventional methods. The principle of SPS and convenient design of the facilities make it attractive for conducting solid state synthesis. In this paper, based on our own results and the literature data, we analyze the microstructure formation of the products of chemical reactions occurring in the SPS in an attempt to formulate the requirements to the microstructure parameters of reactant mixtures and SPS conditions that should be fulfilled in order to produce a nanostructured material. We present successful syntheses of nanostructured ceramics and metal matrix composite with nanosized reinforcements in terms of microstructure stability and attractive properties of the materials and discuss the challenges of making a dense nanostructured material when reaction and densification do not coincide during the SPS. In the final part of the paper, we provide an outlook on the further uses of reactive SPS in the synthesis of nanostructured materials.

1. Introduction

Spark plasma sintering (SPS) has attracted enormous interest from researchers and engineers in the past two decades such that it is now difficult to imagine the development of modern materials science without the advantages offered by this method. SPS uses a combination of uniaxial pressure and pulsed direct current to heat and sinter the powder specimen placed in a die usually made of graphite [1]. When the powders pressed in a die are conductive, the current passes directly through the sample and heats the material rapidly. Nonconductive materials are usually heated by means of heat conduction from the die walls. The role of the ON-OFF pulsing is to create hot spots at the interparticle contacts constantly moving within the sample during the sintering cycle. The sintering is performed in dynamic vacuum protecting

sensitive materials from oxidation, in the meantime enabling processes of chemical reduction. The main advantage of the SPS over conventional pressure-less furnace sintering and hot pressing is a possibility of shortening densification time, lowering sintering temperature and producing nearly fully dense or fully dense materials with limited grain growth. High activity in the SPS-related research in different laboratories is demonstrated by reviews and research articles discussing the process features and mechanisms [2–8], sintering possibilities of nanograined materials [9–11], and systematically describing the material systems [11–13] processed by this method.

With SPS advancing as a promising method for rapid and successful consolidation of nanopowders and nanostructured materials, it has been soon recognized that chemical reactions can be also performed in the SPS so that synthesis and

densification could be combined saving processing time and adding flexibility to the materials design. Researchers became intrigued by a possibility of making nanostructured materials by chemical reactions conveniently placing solid reactants in a SPS-die and subjecting them to pulsed current. If the reactants are prepared in such a way that the reaction occurs at multiple points within the reactant mixture, the treatment of the mixture by pulsed current is highly suitable for reaction initiation and ultimately for synthesizing a nanograined product. Then, if SPS can preserve the microstructure of the ex situ synthesized nanopowders, it is likely that the nanostructured product obtained in situ could be consolidated into a nanostructured body.

By now, reactive SPS has been used for synthesizing nanomaterials and making nanocomposites in a large number of systems. In this paper, we analyze the successes and challenges of reactive SPS and provide an outlook on the further developments in this area. We did not aim at making a list of all studies that have been published up to date, rather, by analyzing the literature data and our own results, we have tried to reveal the factors responsible for the successes of reactive SPS in nanomaterial synthesis and issues pertaining to the processing that still remain unsolved. As in other reactive sintering processes, when new phases form during the SPS, such factors as uniformity of distribution of the reactants in the mixture, heat release during exothermic reactions, specific volume change and the presence of reaction byproducts need to be taken into account when the microstructure evolution of the synthesized product is traced. In addition to factors common to all reactive processes, there are specific features of the microstructure development during the reactive SPS, which are related to the use of electric current: the changes in electrical conductivity of the material during the course of reaction and the presence of high-temperature regions at the inter-particle contacts serving as reaction initiation zones.

2. SPS-Dies as Chemical Reactors: Targeted Synthesis and Undesirable Chemical Reactions

Sintering dies of the SPS facilities can be considered as high-temperature reactors with a controlled atmosphere. Figure 1 shows a schematic of the die-punch setup normally used in the SPS experiments. Beneficially for oxidation-sensitive materials, dynamic vacuum of the SPS chamber creates a protective environment. In the presence of carbon as a material of the die/punches and foil lining the walls of the die (a possible option), the atmosphere of the chamber becomes reducing, which can be helpful in full chemical reduction of oxides present in the material in small concentrations as additives or contamination, or lead to partial reduction of the oxide material being sintered. The reducing environment of the SPS is favorable for conducting reduction reactions to form new phases and nanocomposite structures (e.g., Ni nanoparticle-toughened alumina in situ formed from coprecipitated Al_2O_3 and NiO oxides [14, 15]; magnetic FePt/ Fe_3Pt nanocomposites, in which the Fe_3Pt phase is

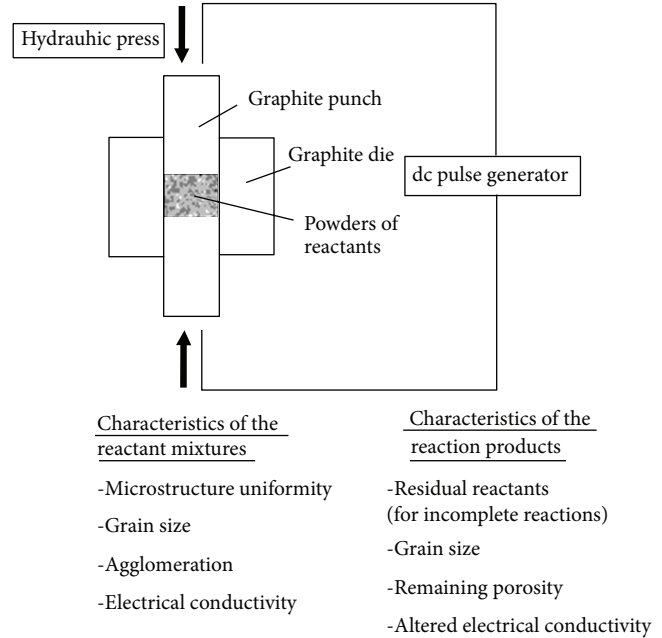


FIGURE 1: A die-punch setup of the SPS facility as a chemical reactor.

formed as a result of in situ reduction of Fe_3O_4 during the SPS [16]) and to tailor the phase composition and microstructure of the surface of SPS-ed specimens (e.g., Fe- FeAl_2O_4 - Al_2O_3 composites, in which the Fe phase in the surface layer is formed in situ by reduction [17]). The reducing action of the SPS environment can be enhanced by increasing the SPS temperature: the higher the SPS-temperature, the lower oxygen content will be retained in the SPS-ed materials.

Thanks to the capabilities of the SPS facilities, such features of reactive sintering as specific volume changes and heat release during exothermic reactions, which create complications in conventional sintering process, can be addressed. Applied pressure helps consolidate the porous reaction product into a denser material upon reaction completion. During the SPS-process, a controlled power input balances the heat from an exothermic reaction so that a temperature schedule is maintained with only small deviations of the measured temperatures from the programmed values. This is achieved by a controlled drop of current through the sample once the reaction is initiated in the system. Experimentally, a stability of the programmed temperature schedule has been proved during the synthesis of titanium diboride [18] and rhenium diboride [19] from elements in the SPS. Compounds that form with extensive evolution of heat can be synthesized in the presence of a diluent, which is introduced into the reactant mixture to decrease the adiabatic temperature of the reaction and to control the grain size of in situ synthesized phases. Similar to conventional self-propagating high-temperature synthesis, the reaction mode in reactive SPS depends on the heating rate with a certain minimum heating rate required to ignite the reaction and to carry it out in a self-sustaining or thermal explosion mode.

Pulsed direct current can enhance the reaction kinetics when the reactants are brought to interaction in the SPS.

This effect is, however, system-dependent. Applied currents induce faster growth of the MoSi_2 product layer in the Mo-Si system [4] relative to the reaction performed without current. In the Hf-B system, no reactivity changes have been observed under applied current as the thicknesses of the HfB_2 product layers formed during the SPS agreed well with the calculations for diffusion couples [20].

The chemical properties and microstructural characteristics of the reactant mixture such as mixing uniformity, grain size and degree of agglomeration will influence the microstructure of the as synthesized product obtained by the SPS. This statement will be also true for other processes of reactive sintering. Specific to the synthesis in the SPS is a change in the electrical conductivity of the materials in the die with reaction advancement and a possibility of controlling the synthesis by varying the electrical conductivity of the reactants. If a high-conductivity additive is introduced into an insulating mixture of the reactants, local high-temperature spots will form within the sample in the regions adjacent to the conducting particles; it is in these hot spots that the reaction will start. When pulsed electric current passes through Ti-B powder mixtures containing Mg additions, hot spots form in the areas adjacent to the Mg grains as the electrical conductivity of Mg is higher than that of the Ti-B mixture [18]. The observed effects of the Mg additions are a reduced ignition temperature and a more uniform sintered product. A similar approach was used for initiating decomposition of magnesium hydride MgH_2 , which is an insulator [21]. In order to increase electrical conductivity, graphite was added to the MgH_2 powder. Magnesium, the product of decomposition, increases the electrical conductivity of the material in the SPS-die. This example shows that as the reaction product accumulates, the conductivity of the material in the sintering die changes; if it increases, the reaction is self-accelerated due to the presence of in situ formed conductive particles inducing the formation of hot spots in the remaining, not yet fully reacted, mixture.

Partial reduction of oxides during the SPS presents another way of increasing electrical conductivity of the material in the sintering die. Interestingly enough, it can be used to advantage to facilitate densification of materials that would otherwise have been heated through conduction from the die only [23]. During the SPS of nanocrystalline rutile TiO_2 , its partial reduction led to the formation of oxygen vacancies and an increase in its electrical conductivity, which, in turn, made it possible for the current to pass through the sample ultimately resulting in successful densification of the material at unexpectedly low temperatures and pressures.

An important factor in the SPS synthesis is the temperature range of the reaction. If the reaction does occur within a wide temperature range during the SPS heating, the upper temperatures of the range are likely to destroy the nanostructure of the synthesized product formed at the initial heating stages. These considerations are illustrated by the synthesis of AlMgB_{14} in the SPS in a mechanically milled mixture of Al, Mg, and B [24]. The first boride phase formed was the lower boride AlMgB_4 , which appeared in the sintered sample at 600°C . The AlMgB_{14} phase was found after the

SPS at 800°C and the synthesis continued until the reaction was complete at 1325°C . The noticeable shrinkage of the sample was observed starting from 1250°C , which is much higher than the reaction onset temperature. Obviously, a fine-grained product was not favored as the grains nucleated in the beginning of the process coalesced and continued to grow with increasing SPS temperature.

Chemical changes in materials during the SPS can be due to reactions that are purposefully conducted (targeted synthesis of new phases) or to undesirable chemical reactions. The latter are interfacial reactions between the phases that are to be preserved, or reduction of oxides that lose their valuable properties upon change in the oxygen content in the SPS environment. An example of an interfacial reaction occurring mainly in the vicinity of contacts between the powder particles was observed in titanium silicon carbide Ti_3SiC_2 -reinforced copper composites ex situ synthesized and SPS-ed [25]. During sintering of 5 vol.% Ti_3SiC_2 -Cu powders, the low intrinsic resistivity of the composite particles and a well-established contact between the powder agglomerates due to applied pressure helped avoiding melting of the copper matrix, which would otherwise have taken place as a result of a local increase in temperature at the particle contacts under pulsed electric current. In the 18 vol.% Ti_3SiC_2 -Cu composite, which has a higher intrinsic resistivity and whose higher hardness prevents the formation of an intimate contact between the composite particles under the chosen pressure (40 MPa), SPS resulted in partial melting of the Cu matrix.

The evidence of melting and resolidification can be seen in the images taken both from the polished cross section and fracture surface of the composite (Figures 2(a) and 2(b)). The XRD phase analysis (Figure 2(c)) shows that local melting of Cu resulted in its fast interaction with Ti_3SiC_2 leading to the formation of TiC_x separated from the Cu-Si melt during the SPS. The EDS analysis confirmed the absence of Ti and the presence of Cu and Si in the resolidified areas marked in Figure 2(a). The concentration of Si in such areas was determined to be 11% by the EDS, which corresponds to the maximum solubility of silicon in copper. This result demonstrated that local melting during the SPS can destabilize the Ti_3SiC_2 phase leading to deintercalation of Si, which dissolves in Cu. Fast cooling of inter-particle contacts during the SPS enables supersaturated Cu (Si) solid solutions to form. Partial melting of the Cu matrix compromises phase stability and uniformity of the microstructure of the Ti_3SiC_2 -Cu composites and therefore, cannot be suggested as a pathway to enhanced densification.

Partial reduction of oxides in the SPS environment can lead to the formation of oxygen vacancies in their crystalline structure [22, 26]. Jiang and Mukherjee have sintered sol-gel-produced Y_2O_3 -MgO composite nanopowders and produced a nanograined compact [22]. Due to oxygen losses, the crystalline lattices of both phases experienced contraction as indicated by decreased lattice parameters determined from the shift of the positions of the corresponding peaks on the XRD patterns (Figure 3). Low infrared transmission of the SPS-ed Y_2O_3 -MgO nanocomposite could be greatly improved when the oxygen content was restored by annealing in air after the SPS (Figure 4).

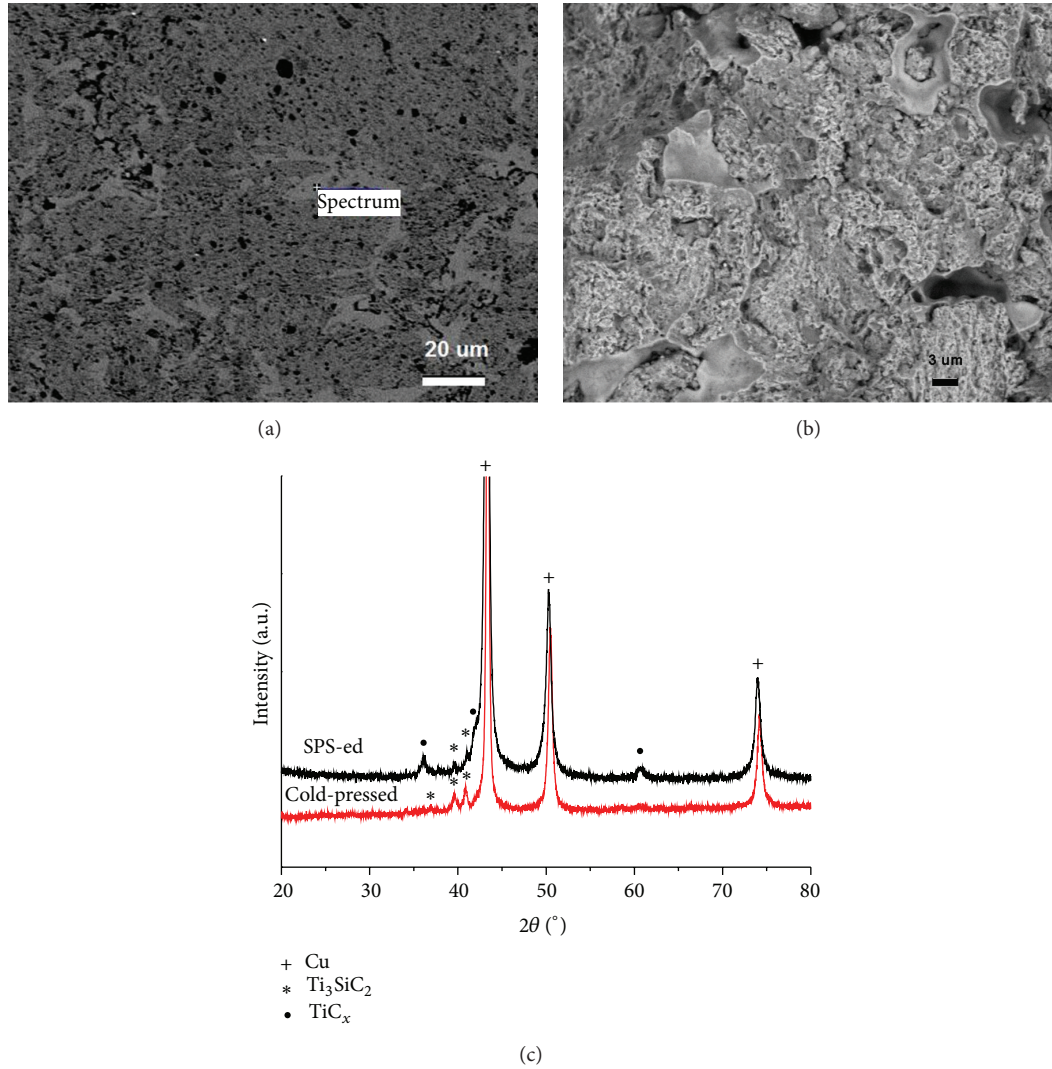


FIGURE 2: Microstructure of the SPS-ed 18 vol.% Ti_3SiC_2 -Cu composite ((a)—polished cross section and (b)—fracture surface) and XRD patterns of the cold-pressed and SPS-ed 18 vol.% Ti_3SiC_2 -Cu compacts (c).

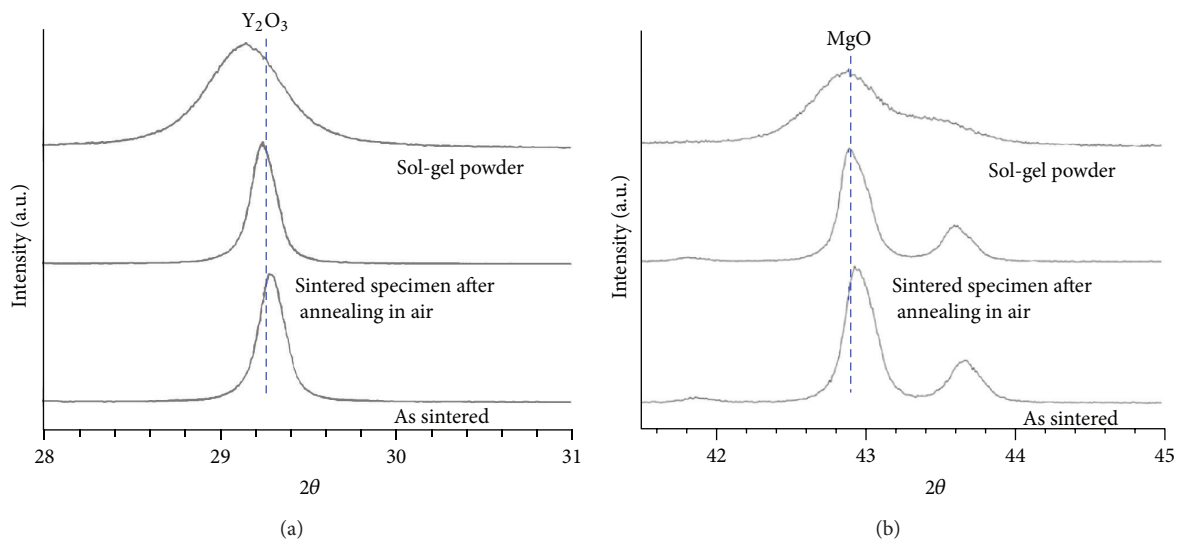


FIGURE 3: XRD patterns of the Y_2O_3 -MgO nanocomposites: powders, SPS-ed and annealed in air after the SPS, showing the shift of the peak positions of both oxides (reprinted from [22], Copyright (2011), with permission from Elsevier).

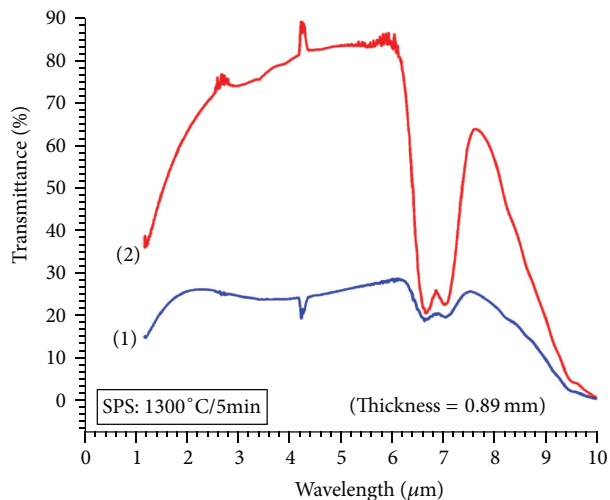


FIGURE 4: Transmission spectra of SPS-ed Y_2O_3 -MgO nanocomposite (1) and after annealing in air (2) (reprinted from [22], Copyright (2011), with permission from Elsevier).

3. Successful Syntheses of Nanostructured Materials and Nanocomposites by Reactive SPS

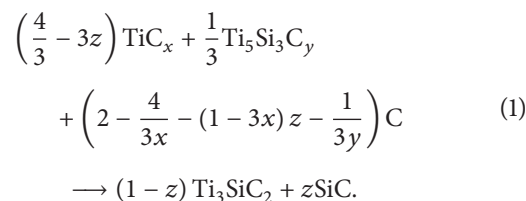
In order to obtain a nanograined or nanocomposite product by a chemical reaction in the SPS, careful choice of the reactants and their preparation procedures should be made. The microstructure of the precursor is of primary importance. In order to initiate the reaction at many nucleation sites at the same time, a large number of contact points between the solid reactants should be established, which is favored by well-developed interfaces in the reactant mixture. The most visible solution along this line is to have particles of reactants as small as possible and to mix them thoroughly avoiding the formation of aggregates of particles of the same type. However, as will be discussed later, a mixture of fine particles or grains is not the only way to create conditions for the formation of nanosized reaction products.

If two nanopowders are selected as initial reactants and the aggregates of each component are retained in the mixture, then the availability of the reactants to each other is greatly reduced. In such cases, sintering of particles of the same powder can occur before the reaction starts. Kim et al. [27] applied dry mixing and ultrasonic treatment in liquid in an attempt to improve the mixing uniformity of nickel and aluminum nanopowders and proved the former to be more efficient in breaking the nanoparticle aggregates. In order to obtain a nanograined product, it may be sufficient to have only one reactant in the form of nanopowder. A demonstration of this possibility is the synthesis of nano-HfB₂ through the reaction between micron-sized B₄C powder, HfO₂ nanopowder, and phenolic resin [28]. The crucial influence of the preparation procedure of a two-phase mixture of nanopowders on the reaction onset temperature and resultant microstructure of the reaction product was clearly shown in a comparative study by Stanciu et al. [29], who used three types of precursors for reactive sintering of Al₂TiO₅: co-gelified Al₂O₃ and

TiO₂ powders, mechanical mixtures of Al₂O₃ and TiO₂ individual sol-gel powders, and powders synthesized by coprecipitation. As is seen from the XRD patterns, the reaction between co-gelified Al₂O₃ and TiO₂ powders was complete after the SPS at 1100°C occurring only partially in the other two precursors (Figure 5).

A more widely used powder preparation technique for the subsequent reactive SPS is mechanical milling [32], in which powders with a size from several to several tens of microns are normally used as raw materials. The powder mixtures are placed in a vial and subjected to impact and shear from the milling media. During milling, the powders experience grinding and particle and grain size reduction and accumulate defects of the crystalline structure. Repeated fracturing and cold welding of the particles during mechanical milling gradually refine the microstructure of the milled mixture, improve its uniformity and increase the interfacial area between the components. If high-intensity milling is used, the targeted reaction can partially occur during milling. The presence of certain amounts of reaction products in the mixture prior to sintering can help form and preserve a nanostructured material after the SPS when the product grains serve as multiple nucleation centers. As was shown by Munir [9], the presence of reaction products in the mechanically milled Mo-Si mixture helped achieve a finer-grained product synthesized in the SPS. However, depending on the mixing uniformity, distribution and number/size of the product grains formed during milling, an opposite influence can be also expected if a few product grains formed during milling continue to grow consuming the reactants during the SPS. In such cases, a coarse-grained material will develop as a result of the reactive SPS.

Sintering of powder precursors with well-developed interfaces between the reactants is the most common approach to the synthesis of nanomaterials by reactive SPS. Interestingly enough, interfaces can develop during the reaction itself, if the latter proceeds through several stages and thus has a complex mechanism. Zhang et al. [30] have shown that a phase with grains as small as 100 nm can form as a result of a solid state reaction between micron-sized powders. They have synthesized a Ti₃SiC₂-SiC composite from the mixture of Ti, C and Si. The intermediate crystalline phases TiC_x and Ti₅Si₃C_y formed first from the elements and then participated in the reaction:



The resultant SiC phase had a grain size of about 100 nm, while the Ti₃SiC₂ phase had grains grown up to 5 μm (Figure 6). The formation of SiC through intermediate products rather than by a direct reaction from the elements appears to be crucial for the microstructure development of the Ti₃SiC₂-SiC nanocomposites, the mixture of intermediate phases possessing a refined structure relative to that of the

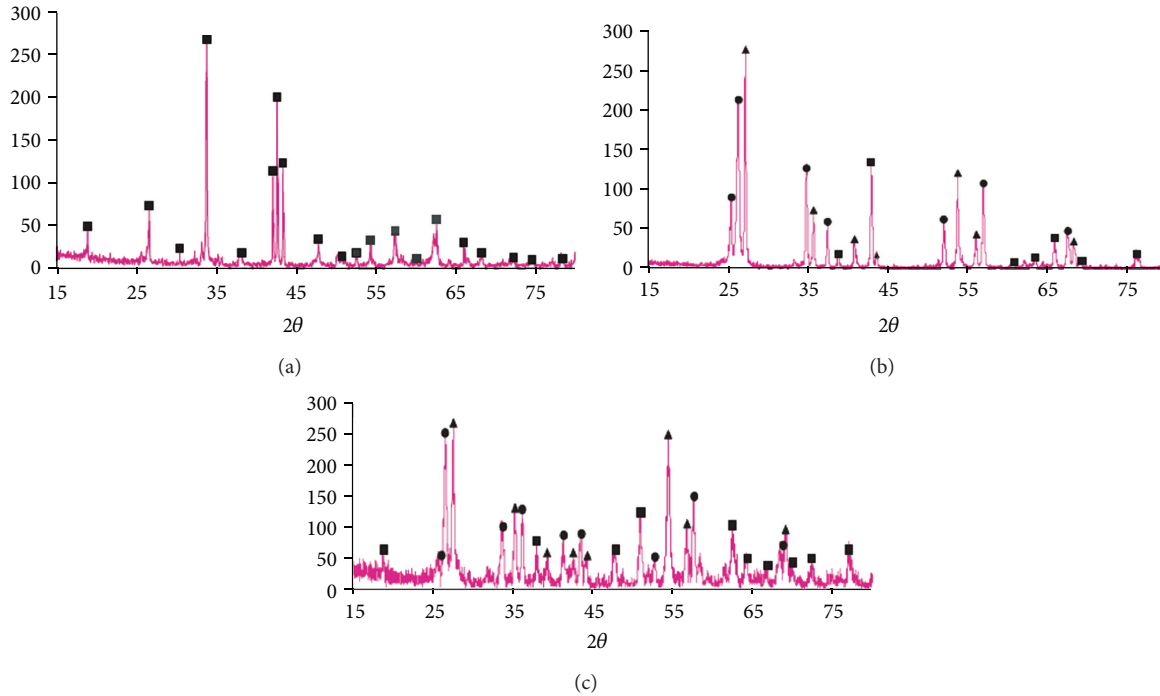


FIGURE 5: XRD patterns of the SPS-ed compacts produced from Al_2O_3 and TiO_2 nanopowder mixtures of different processing histories, SPS-temperature 1100°C : (a)—co-gelified Al_2O_3 and TiO_2 powders, (b)—mechanical mixtures of Al_2O_3 and TiO_2 individual sol-gel powders, (c)—powders synthesized by co-precipitation; squares- Al_2TiO_5 , triangles- TiO_2 , and circles- Al_2O_3 (reprinted from [29], Copyright (2004), with permission from Elsevier).

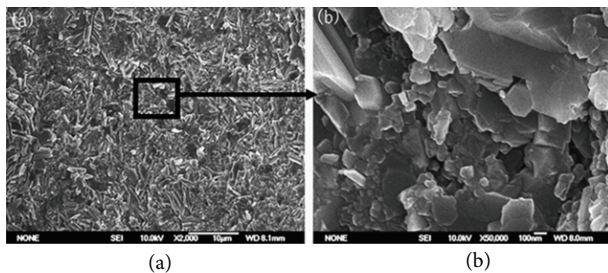


FIGURE 6: Fracture surface of Ti_3SiC_2 -SiC nanocomposite SPS-ed at 1280°C showing grains of SiC about 100 nm in size, (a)—lower magnification, (b)—higher magnification (reprinted from [30], Copyright (2007), with permission from Elsevier).

reactant mixture. Similar observations have been reported by Wang et al. [33] for the submicron-grained $\text{TiN-Al}_2\text{O}_3$ composites formed from AlN , TiO_2 and Ti powders, all three having particles from several to several tens of microns. Though the powders were mixed by milling, the conditions of mixing were mild (mixing was conducted in ethanol); therefore, a significant grain size reduction could not be expected. From the reported experimental results, it can be assumed that the fine-grained structure of the composite was due to a sequence of several solid state reactions occurring in the reactant mixture.

Flexible control over the SPS parameters allows inducing nanocrystallization of amorphous metallic [34, 35] and non-metallic [36] matrices and maintaining the nanostructure of the composite materials until the end of sintering. A further

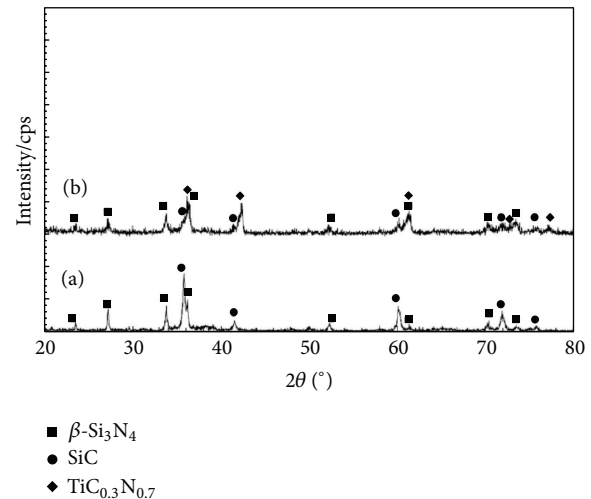


FIGURE 7: XRD patterns of the Si_3N_4 -SiC ceramic nanocomposite obtained by SPS of a Si-C-N amorphous precursor (a) and Si_3N_4 -SiC- $\text{TiC}_{0.3}\text{N}_{0.7}$ ceramic nanocomposite obtained by reactive SPS in a mixture of nanocrystalline TiO_2 with amorphous Si-C-N (reprinted from [31], Copyright (2004), with permission from Elsevier).

development of this processing route is the use of amorphous solids as reactants in mixtures with other phases. Following this line, Duan et al. [31, 37] synthesized Si_3N_4 -SiC- $\text{TiC}_{0.3}\text{N}_{0.7}$ ceramic nanocomposites (Figure 7) by reactive SPS starting from a mixture of nanocrystalline TiO_2 and an amorphous Si-C-N material obtained by pyrolysis of a polymer. In the synthesized composite, the $\text{TiC}_{0.3}\text{N}_{0.7}$ phase formed

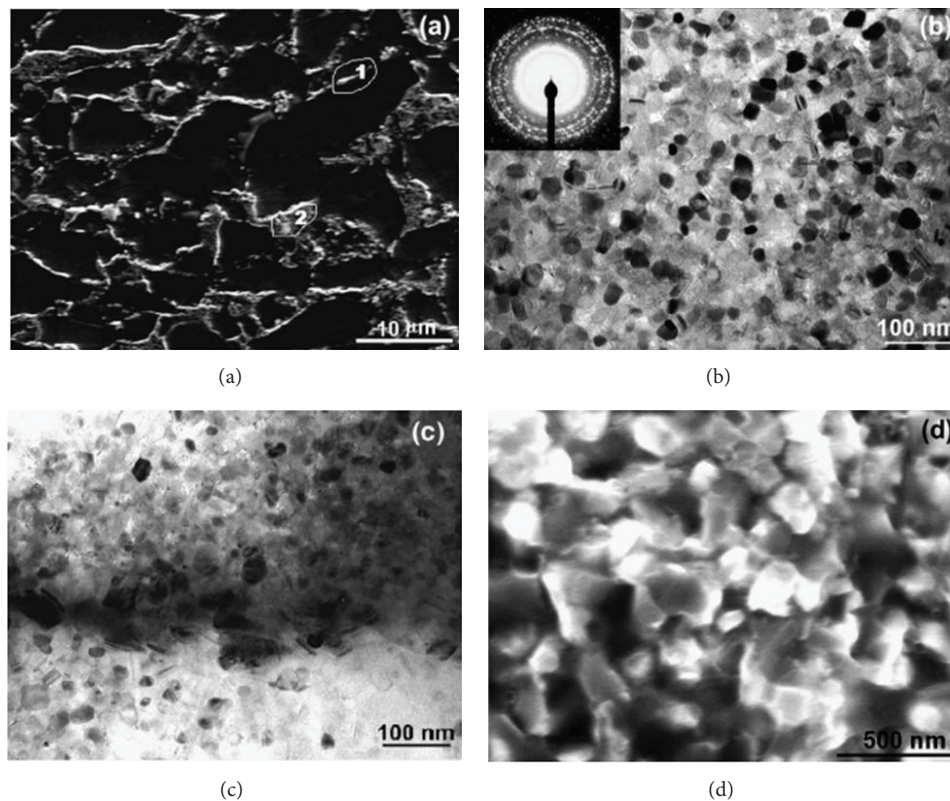


FIGURE 8: $\text{Si}_3\text{N}_4/\text{SiC}/\text{TiC}_{0.3}\text{N}_{0.7}$ nanocomposite: (a)—fracture surface, SEM; (b)—microstructure of dark areas in (a) corresponding to the $\text{Si}_3\text{N}_4/\text{SiC}$, TEM; (c)—region 1 in (a), TEM; (d)—region 2 in (a) corresponding to the $\text{TiC}_{0.3}\text{N}_{0.7}$ phase, SEM (reprinted from [31], Copyright (2004), with permission from Elsevier).

a network composed of 100–300 nm grains, which penetrated through the regions of the $\text{Si}_3\text{N}_4/\text{SiC}$ composite with grains ranging from 20 to 30 nm (Figure 8); improved densification of the three-phase composite was achieved in comparison to the SPS of the amorphous Si-C-N alone.

If refractory compounds are synthesized in the SPS form by exothermic chemical reactions, local heat evolution in the reaction initiation zones and the concomitant temperature rise in the adjacent regions can make it very challenging to synthesize materials with nanosized grains. If the reaction is moderately exothermic, the product grains do not grow as fast and, provided a suitable SPS schedule is found for densification, a nanostructured bulk product can be obtained. Examples of successful syntheses have been reported by Munir [9], who synthesized nanostructured MoSi_2 with 140 nm grains, and by Paris et. al. [38], who showed that iron aluminides with 30–90 nm grains could be obtained from mechanically milled mixtures, in which the reactants were refined and thoroughly intermixed at the nanoscale.

Ceramic nanomaterials and nanocomposites synthesized in the SPS show attractive mechanical properties making a careful selection of reactants and process parameters worthwhile. One of the most significant achievements of the reactive SPS is the preparation of fracture-tough ceramics. Monolithic titanium monoboride TiB with needle-shaped grains produced by reactive SPS possessed a fracture toughness of $5.9 \pm 0.4 \text{ MPa}\cdot\text{m}^{1/2}$ [39]. A fracture toughness of

$6.5 \text{ MPa}\cdot\text{m}^{1/2}$ and a microhardness of 20.6 GPa were achieved in TiN-TiB₂ in situ composites [40]. Along with high fracture toughness, other attractive properties appeared: Si_3N_4 -SiC-TiC_{0.3}N_{0.7} nanocomposite showed a fracture toughness of $6.7 \text{ MPa}\cdot\text{m}^{1/2}$ and metal-like electrical conductivity [31, 37] while nanoorganized MoSi_2 synthesized in the SPS exhibited a fracture toughness of $5.8 \pm 0.4 \text{ MPa}\cdot\text{m}^{1/2}$ and better oxidation resistance than its microcrystalline analog [41].

Full reduction of a metal oxide to a metallic phase in the SPS is used to synthesize metallic nanoparticle-toughened ceramics [15]. During the SPS of the Al_2O_3 - NiAl_2O_4 two-phase composite synthesized by co-precipitation and calcination, Ni nucleated from the NiAl_2O_4 phase so that in the resultant composite, Ni nanoparticles were uniformly distributed in the matrix of Al_2O_3 . The presence of metallic nanoparticles improved the bending strength and fracture toughness of the nanocomposite relative to Al_2O_3 .

Successful synthesis and consolidation of metal matrix composites containing nanoparticles of reinforcing phases by reactive SPS have been demonstrated for Ti_5Si_3 -Ti [42] and Fe_3C -Fe systems [43]. The distribution uniformity of Si achieved during mechanical milling of Ti-Si powder mixtures ensured the formation of 100–200 nm Ti_5Si_3 particles during the SPS; these particles stabilized an ultra-fine grained structure of the Ti matrix (200–400 nm), smaller titanium grains being observed in composites with higher Si

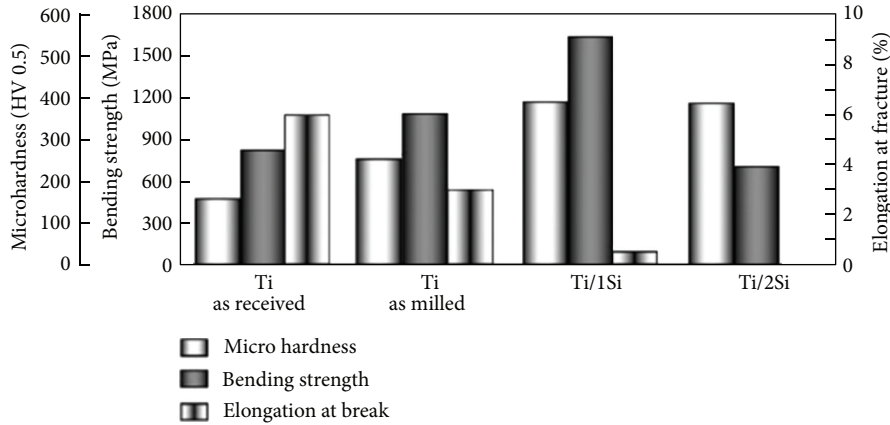


FIGURE 9: Microhardness, bending strength, and elongation at fracture of SPS-ed Ti-based materials; Ti/1Si and Ti/2Si denote Ti_5Si_3 -Ti composites containing 1 and 2 wt.% of Si, respectively, (reprinted from [42], Copyright (2006), with permission from Elsevier).

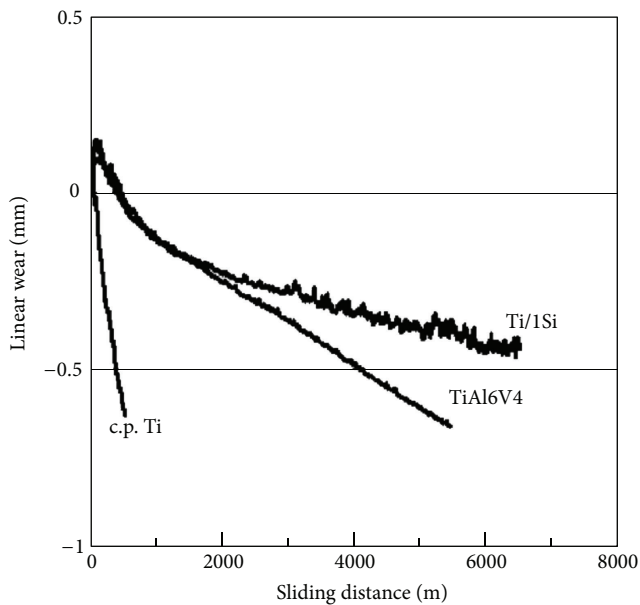


FIGURE 10: Wear behavior of Ti- Ti_5Si_3 composites (Si content 1 wt.%) produced by mechanical milling and SPS compared to that of pure titanium and the TiAl6V4 alloy (reprinted from [42], Copyright (2006), with permission from Elsevier).

content [42]. This unique microstructure was responsible for attractive mechanical properties of the Ti_5Si_3 -Ti composite possessing strength comparable to that of the Ti6Al4V alloy and improved wear resistance (Figures 9 and 10). Interesting combinations of strength and ductility were achieved in Fe-C alloys produced by SPS of mechanically milled mixtures of iron and graphite, the formation of cementite Fe_3C taking place during sintering of a nanostructured precursor [43]. The fully dense materials were composed of a nanostructured ferrite matrix having an average grain size of 150 nm and cementite Fe_3C dispersoids a few nanometers in size distributed in the ferrite grains and along the grain boundaries. The yield strength of the SPS-ed Fe- Fe_3C composite was 2000 MPa, while its fracture strength and

plastic strain reached 3500 MPa and 40%, respectively. High plastic deformation of the composite was an interesting finding, as nanostructured Fe-based alloys produced by other consolidation methods are normally much more brittle. This unique behavior of the Fe- Fe_3C composites was attributed to its full density, good metallurgical bonding achieved during the SPS, and a uniform distribution of the dispersoid phase retaining its fine size after sintering and preventing the material failure by inhomogeneous deformation during shear events rather characteristic of other Fe-based nanocrystalline alloys.

4. Challenges of Producing Dense Nanomaterials by Reactive SPS

The microstructure development during the reactive SPS follows one of the two possible scenarios: (1) simultaneous reaction and densification; (2) complete reaction followed by densification (if the latter is aimed at) at higher temperatures. A chemical reaction within a narrow temperature range accompanied by shrinkage of the sample is the best situation for the formation of a dense nanostructured product [9]. However, the reaction and densification steps do not always coincide during the reactive SPS. When the reaction is complete before densification starts, then, in order to obtain a fully dense product, one has to resort to higher-temperature sintering. Anselmi-Tamburini et al. [44] have shown that boron carbide B_4C forms in the mixtures of amorphous boron and carbon black at 1200°C during the SPS, while temperatures as high as 1900°C are required to produce a dense compact from the reaction product. In certain cases, full density sintered products can only be obtained when the fine structure of the material is sacrificed. The interrelation between the grain size and density of boron carbide B_4C synthesized from the mixtures of amorphous boron and carbon black nanopowders was demonstrated by Hulbert et al. [45, 46], who used an off-set die in the SPS facility. Modeling of the process suggested that the difference between the temperatures of the upper and bottom parts of the sample was 400 K. The sintered material had a gradient structure in

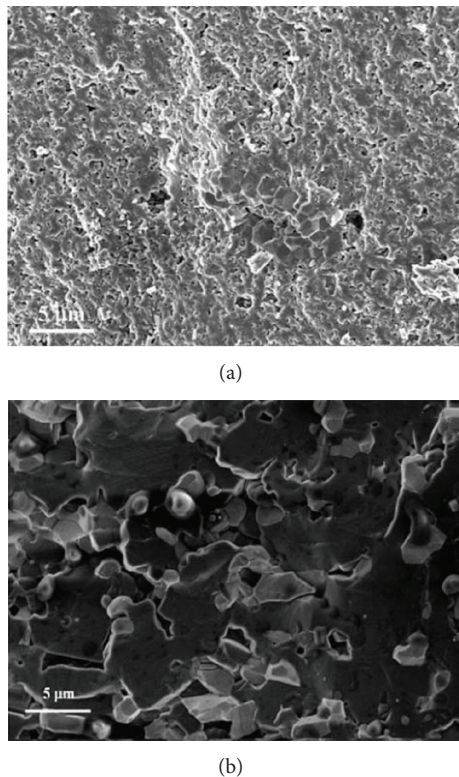


FIGURE 11: Fracture surface of the $\text{TiB}_2\text{-B}_4\text{C}$ composite showing an agglomerate of TiB_2 with a pore in the center, reactant mixture milled for 4 h, SPS-ed at 1600 (a); a nearly fully dense $\text{TiB}_2\text{-B}_4\text{C}$, reactant mixture milled for 16 h, SPS-ed at 1700 (b) (reprinted from [48], Copyright (2009), with permission from Elsevier).

terms of grain size and porosity. Within the sample, a fine-grained porous B_4C with grains of 200 nm was formed in the regions subjected to lower temperatures, while dense boron carbide with grains about $2\ \mu\text{m}$ in size could be found in parts of the sample that experienced higher sintering temperatures.

In single-phase materials synthesized by reactive SPS, the microstructure evolution can be described using the grain size and porosity characteristics. In composite materials, the grain size may not be the same for all constituent phases depending on the mechanism of the synthesis reaction and the tendency of each material to coarsen during sintering. The porosity distribution may not be uniform throughout the volume of the composite. When working with a multiphase material, one has to take into account the differences in properties of the phases, such as characteristic grain growth and densification rates. An illustration of the above considerations is the in situ synthesized $\text{B}_4\text{C-23 vol.}\% \text{TiB}_2$ composites obtained by reactive SPS from Ti-B-C mechanically milled mixtures [47, 48]. The agglomeration of titanium diboride is seen in the SPS-ed $\text{B}_4\text{C-TiB}_2$ samples that were milled for durations insufficient for a uniform distribution of titanium [47]. The agglomerates of titanium diboride consisted of faceted grains $1\text{-}2\ \mu\text{m}$ in size and contained a pore in the center (Figure 11).

In the same sample, the boron carbide phase showed much smaller grains. The presence of a pore inside the TiB_2

agglomerate can be explained by a decrease in the specific volume that accompanies the reaction between metallic titanium and boron. Faster densification of the synthesized boron carbide, whose content in the composite was 77 vol.% and which thus played the role of a matrix being already quite dense by the moment the reaction between Ti and B was complete, did not allow TiB_2 grains to rearrange and better sinter between themselves. Due to refractory nature of TiB_2 , its agglomerates comprised the major part of the total porosity of the composites. In order to eliminate this porosity, the distribution of titanium should be more uniform, which was achieved by a longer mechanical milling of the reactant mixtures. As is seen from Figure 11(b), the nearly fully dense material had micron-sized grains of both phases. Similar observation for the $\text{B}_4\text{C-TiB}_2$ composites was reported by Nikzad et al. [49] showing that a relative density of 98% could be only achieved allowing marked grain growth to happen. The gradually coarsening microstructure of the in situ $\text{B}_4\text{C-TiB}_2$ composites obtained upon increasing electric current while keeping the other experimental parameters constant is demonstrated in Figure 12. Although submicron grains can be seen in the sample SPS-ed at 1100 A and having a relative density of 94%, the sample of 98% relative density reveals excessive grain growth such that both phases are represented by grains of several microns.

5. Outlook

As the information on the successes of SPS in the rapid and convenient synthesis of new materials and compounds as well as previously known materials but of improved microstructure and properties penetrates into new areas of materials science, an increasing number of researchers express their interest in performing feasibility tests and later on to embark on a systematic study of the synthesis of their materials with the help of this promising method. In the past two decades, we have seen a large number of studies on reactive SPS. Most of them are based on chemical reactions between premixed reactants to synthesize new compounds and composites. A pathway to nanostructured products through decomposition reactions well established in materials science has not yet been given full attention in regard to the SPS capabilities. Thermal decomposition of salts [50] resulting in the formation of metal nanoparticles can become reactions of choice to be performed in the SPS. In the coming years, new syntheses routes can be anticipated to be found for various materials using SPS in its usual design as well as with new geometries of dies and punches. Once the conditions for the nanostructure formation are established using simple geometries, the temperature distribution in the reacting sample can be varied by a more elaborate design of the die-punch setup. The synthesis thus can be implemented to give microstructures with gradients in the grain size and porosity including bodies of tubular geometries [51]. The successes of reactive SPS in synthesizing bulk nanostructured materials can be further extended by the simultaneous synthesis and, joining of two materials [52] as well as by the manufacturing of nanostructured coatings [53–55].

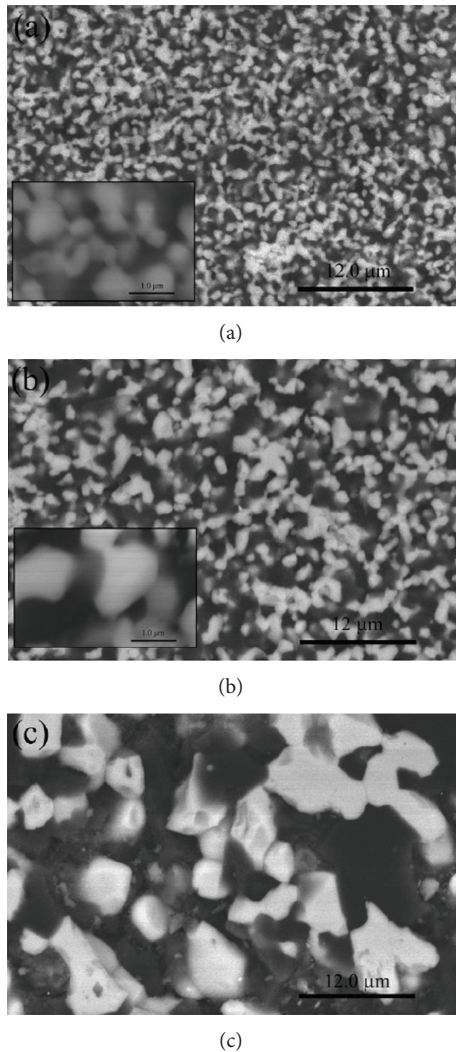


FIGURE 12: Microstructure of the B_4C - TiB_2 composites SPS-ed using different electric current values ((a)—1100 A, (b)—1150 A, and (c)—1200 A) (reprinted from [49], Copyright (2012), with permission from Elsevier).

6. Conclusions

Initially designed for conducting solid state sintering, SPS has been proved to be attractive for conducting solid state chemical reactions. Being a powerful technique and a user-friendly facility, SPS has been developed into a method of solid state synthesis under applied electric current and mechanical pressure. An increasing number of solid state chemists consider SPS as a new tool, full capabilities of which are yet to be discovered. If the reactants are mixed at the nanolevel, then the formation of a nanograined product during the SPS will be favored. However, there exists a specific microstructure development path with multiple intermediate reaction products: even though the reaction started in the mixture of coarse-grained powders, its final products can be composed of nanograins. Making a dense material from the nanostructured reaction product in the SPS is another challenge; in certain cases, when the reaction is complete

before any substantial densification occurs, successful consolidation cannot be achieved without sacrificing the as synthesized nanostructure. However, applying the same principles of optimization of the SPS parameters as those used for consolidation of ex situ produced nanopowders, a processing parameter window can be found to maintain the fine grain size of the reaction product until the sintering completion.

Acknowledgments

Professor Amiya K. Mukherjee acknowledges support by a grant from the US Office of Naval Research (ONR Grant no. N00014-10-1-0632) with Dr. Lawrence Kabacoff as the Program Manager. Dr. Dina V. Dudina acknowledges support by a grant from the Mayor's Office of Novosibirsk, Russian Federation (15-12, 24.05.2012).

References

- [1] M. Tokita, "Trends in advanced SPS spark plasma sintering systems and technology," *Journal of the Society of Powder Technology Japan*, vol. 30, no. 11, pp. 790–804, 1993.
- [2] J. R. Groza and A. Zavaliangos, "Sintering activation by external electrical field," *Materials Science and Engineering A*, vol. 287, no. 2, pp. 171–177, 2000.
- [3] U. Anselmi-Tamburini, S. Gennari, J. E. Garay, and Z. A. Munir, "Fundamental investigations on the spark plasma sintering/synthesis process: II. Modeling of current and temperature distributions," *Materials Science and Engineering A*, vol. 394, no. 1-2, pp. 139–148, 2005.
- [4] U. Anselmi-Tamburini, J. E. Garay, and Z. A. Munir, "Fundamental investigations on the spark plasma sintering/synthesis process. III. Current effect on reactivity," *Materials Science and Engineering A*, vol. 407, no. 1-2, pp. 24–30, 2005.
- [5] Z. A. Munir, U. Anselmi-Tamburini, and M. Ohyanagi, "The effect of electric field and pressure on the synthesis and consolidation of materials: a review of the spark plasma sintering method," *Journal of Materials Science*, vol. 41, no. 3, pp. 763–777, 2006.
- [6] Z. A. Munir, D. V. Quach, and M. Ohyanagi, "Electric current activation of sintering: a review of the pulsed electric current sintering process," *Journal of the American Ceramic Society*, vol. 94, no. 1, pp. 1–19, 2011.
- [7] D. M. Hulbert, A. Anders, D. V. Dudina et al., "The absence of plasma in 'spark plasma sintering,'" *Journal of Applied Physics*, vol. 104, no. 3, Article ID 033305, 2008.
- [8] T. Holland, T. B. Tran, D. V. Quach, U. Anselmi-Tamburini, J. R. Groza, and A. K. Mukherjee, "Athermal and thermal mechanisms of sintering at high heating rates in the presence and absence of an externally applied field," *Journal of the European Ceramic Society*, vol. 32, no. 14, pp. 3675–3683, 2012.
- [9] Z. A. Munir, "Synthesis and densification of nanomaterials by mechanical and field activation," *Journal of Materials Synthesis and Processing*, vol. 8, no. 3-4, pp. 189–196, 2000.
- [10] J. R. Groza and A. Zavaliangos, "Nanostructured bulk solids by field activated sintering," *Reviews on Advanced Materials Science*, vol. 5, no. 1, pp. 24–33, 2003.
- [11] N. Saheb, Z. Iqbal, A. Khalil et al., "Spark Plasma Sintering of metals and metal matrix nanocomposites: a review," *Journal of Nanomaterials*, vol. 2012, Article ID 983470, 13 pages, 2012.

- [12] R. Orrù, R. Licheri, A. M. Locci, A. Cincotti, and G. Cao, "Consolidation/synthesis of materials by electric current activated/assisted sintering," *Materials Science and Engineering R*, vol. 63, no. 4-6, pp. 127-287, 2009.
- [13] T. Hungria, J. Galy, and A. Castro, "Spark plasma sintering as a useful technique to the nanostructuring of piezo-ferroelectric materials," *Advanced Engineering Materials*, vol. 11, no. 8, pp. 615-631, 2009.
- [14] T. Isobe, K. Daimon, K. Ito, T. Matsubara, Y. Hikichi, and T. Ota, "Preparation and properties of $\text{Al}_2\text{O}_3/\text{Ni}$ composite from NiAl_2O_4 spinel by in situ reaction sintering method," *Ceramics International*, vol. 33, no. 7, pp. 1211-1215, 2007.
- [15] T. Isobe, K. Daimon, T. Sato, T. Matsubara, Y. Hikichi, and T. Ota, "Spark plasma sintering technique for reaction sintering of $\text{Al}_2\text{O}_3/\text{Ni}$ nanocomposite and its mechanical properties," *Ceramics International*, vol. 34, no. 1, pp. 213-217, 2008.
- [16] C.-B. Rong, V. Nandwana, N. Poudyal et al., "Bulk FePt Fe_3Pt nanocomposite magnets prepared by spark plasma sintering," *Journal of Applied Physics*, vol. 101, no. 9, Article ID 09K515, 2007.
- [17] J. Gurt Santanach, C. Estournès, A. Weibel, A. Peigney, G. Chevallier, and C. Laurent, "Spark plasma sintering as a reactive sintering tool for the preparation of surface-tailored $\text{Fe-FeAl}_2\text{O}_4\text{-Al}_2\text{O}_3$ nanocomposites," *Scripta Materialia*, vol. 60, no. 4, pp. 195-198, 2009.
- [18] D. Salamon, M. Eriksson, M. Nygren, and Z. Shen, "Homogeneous TiB_2 ceramics achieved by electric current-assisted self-propagating reaction sintering," *Journal of the American Ceramic Society*, vol. 90, no. 10, pp. 3303-3306, 2007.
- [19] A. M. Locci, R. Licheri, R. Orrù, and G. Cao, "Reactive Spark Plasma Sintering of rhenium diboride," *Ceramics International*, vol. 35, no. 1, pp. 397-400, 2009.
- [20] U. Anselmi-Tamburini, Y. Kodera, M. Gasch et al., "Synthesis and characterization of dense ultra-high temperature thermal protection materials produced by field activation through spark plasma sintering (SPS): I. Hafnium diboride," *Journal of Materials Science*, vol. 41, no. 10, pp. 3097-3104, 2006.
- [21] J. Schmidt, R. Niewa, M. Schmidt, and Y. Grin, "Spark plasma sintering effect on the decomposition of MgH_2 ," *Journal of the American Ceramic Society*, vol. 88, no. 7, pp. 1870-1874, 2005.
- [22] D. Jiang and A. K. Mukherjee, "The influence of oxygen vacancy on the optical transmission of an yttria-magnesia nanocomposite," *Scripta Materialia*, vol. 64, no. 12, pp. 1095-1097, 2011.
- [23] J. H. Noh, H. S. Jung, I.-S. Cho et al., "Enhancing the densification of nanocrystalline TiO_2 by reduction in spark plasma sintering," *Journal of the American Ceramic Society*, vol. 93, no. 4, pp. 993-997, 2010.
- [24] D. J. Roberts, J. Zhao, and Z. A. Munir, "Mechanism of reactive sintering of MgAlB_{14} by pulse electric current," *International Journal of Refractory Metals and Hard Materials*, vol. 27, no. 3, pp. 556-563, 2009.
- [25] D. V. Dudina, V. I. Mali, A. G. Anisimov et al., " $\text{Ti}_3\text{SiC}_2\text{-Cu}$ composites by mechanical milling and Spark Plasma Sintering: possible microstructure formation scenarios," *Metals and Materials International*. In press.
- [26] D. Jiang, D. M. Hulbert, U. Anselmi-Tamburini, T. Ng, D. Land, and A. K. Mukherjee, "Optically transparent polycrystalline Al_2O_3 produced by spark plasma sintering," *Journal of the American Ceramic Society*, vol. 91, no. 1, pp. 151-154, 2008.
- [27] J. S. Kim, H. S. Choi, D. Dudina, J. K. Lee, and Y. S. Kwon, "Spark plasma sintering of nanoscale ($\text{Ni} + \text{Al}$) powder mixture," *Diffusion and Defect Data B*, vol. 119, pp. 35-38, 2007.
- [28] H. Wang, S.-H. Lee, and H.-D. Kim, "Nano-hafnium diboride powders synthesized using a spark plasma sintering apparatus," *Journal of the American Ceramic Society*, vol. 95, no. 5, pp. 1493-1496, 2012.
- [29] L. Stanciu, J. R. Groza, L. Stoica, and C. Plapcianu, "Influence of powder precursors on reaction sintering of Al_2TiO_5 ," *Scripta Materialia*, vol. 50, no. 9, pp. 1259-1262, 2004.
- [30] J. Zhang, L. Wang, L. Shi, W. Jiang, and L. Chen, "Rapid fabrication of $\text{Ti}_3\text{SiC}_2\text{-SiC}$ nanocomposite using the spark plasma sintering-reactive synthesis (SPS-RS) method," *Scripta Materialia*, vol. 56, no. 3, pp. 241-244, 2007.
- [31] R.-G. Duan, J. D. Kuntz, J. E. Garay, and A. K. Mukherjee, "Metal-like electrical conductivity in ceramic nano-composite," *Scripta Materialia*, vol. 50, no. 10, pp. 1309-1313, 2004.
- [32] C. Suryanarayana, "Mechanical alloying and milling," *Progress in Materials Science*, vol. 46, no. 1-2, pp. 1-184, 2001.
- [33] L. Wang, T. Wu, W. Jiang, J. Li, and L. Chen, "Novel fabrication route to $\text{Al}_2\text{O}_3\text{-TiN}$ nanocomposites via spark plasma sintering," *Journal of the American Ceramic Society*, vol. 89, no. 5, pp. 1540-1543, 2006.
- [34] S. Ishihara, W. Zhang, H. Kimura, M. Omori, and A. Inoue, "Consolidation of Fe-Co-Nd-Dy-B glassy powders by spark-plasma sintering and magnetic properties of the consolidated alloys," *Materials Transactions*, vol. 44, no. 1, pp. 138-143, 2003.
- [35] L. Perrière, M. T. Thai, S. Tusseau-Nenez, M. Blétry, and Y. Champion, "Spark plasma sintering of a Zr-based metallic glass," *Advanced Engineering Materials*, vol. 13, no. 7, pp. 581-586, 2011.
- [36] J. Wan, R.-G. Duan, M. J. Gasch, and A. K. Mukherjee, "Methods of processing $\text{Si}_3\text{N}_4/\text{SiC}$ nano-nano composites from polymer precursor," *Materials Science and Engineering A*, vol. 424, no. 1-2, pp. 105-116, 2006.
- [37] R.-G. Duan, J. E. Garay, J. D. Kuntz, and A. K. Mukherjee, "Electrically conductive in situ formed nano- $\text{Si}_3\text{N}_4/\text{SiC}/\text{TiC}_x\text{N}_{1-x}$ ceramic composite consolidated by Pulse Electric Current Sintering (PECS)," *Journal of the American Ceramic Society*, vol. 88, no. 1, pp. 66-70, 2005.
- [38] S. Paris, E. Gaffet, F. Bernard, and Z. A. Munir, "Spark plasma synthesis from mechanically activated powders: a versatile route for producing dense nanostructured iron aluminides," *Scripta Materialia*, vol. 50, no. 5, pp. 691-696, 2004.
- [39] Z. Zhang, X. Shen, F. Wang, and S. Lee, "A new rapid route for in situ synthesizing monolithic TiB ceramic," *Journal of the American Ceramic Society*, vol. 94, no. 9, pp. 2754-2756, 2011.
- [40] J. W. Lee, Z. A. Munir, M. Shibuya, and M. Ohyanagi, "Synthesis of dense $\text{TiB}_2\text{-TiN}$ nanocrystalline composites through mechanical and field activation," *Journal of the American Ceramic Society*, vol. 84, no. 6, pp. 1209-1216, 2001.
- [41] G. Cabouro, S. Chevalier, E. Gaffet, Y. Grin, and F. Bernard, "Reactive sintering of molybdenum disilicide by spark plasma sintering from mechanically activated powder mixtures: processing parameters and properties," *Journal of Alloys and Compounds*, vol. 465, no. 1-2, pp. 344-355, 2008.
- [42] D. Handtrack, F. Despong, C. Sauer, B. Kieback, N. Reinfried, and Y. Grin, "Fabrication of ultra-fine grained and dispersion-strengthened titanium materials by spark plasma sintering," *Materials Science and Engineering A*, vol. 437, no. 2, pp. 423-429, 2006.
- [43] H. W. Zhang, R. Gopalan, T. Mukai, and K. Hono, "Fabrication of bulk nanocrystalline Fe-C alloy by spark plasma sintering of mechanically milled powder," *Scripta Materialia*, vol. 53, no. 7, pp. 863-868, 2005.

- [44] U. Anselmi-Tamburini, Z. A. Munir, Y. Kodera, T. Imai, and M. Ohyanagi, "Influence of synthesis temperature on the defect structure of boron carbide: experimental and modeling studies," *Journal of the American Ceramic Society*, vol. 88, no. 6, pp. 1382–1387, 2005.
- [45] D. M. Hulbert, D. Jiang, U. Anselmi-Tamburini, C. Unuvar, and A. K. Mukherjee, "Experiments and modeling of spark plasma sintered, functionally graded boron carbide-aluminum composites," *Materials Science and Engineering A*, vol. 488, no. 1-2, pp. 333–338, 2008.
- [46] D. M. Hulbert, D. Jiang, U. Anselmi-Tamburini, C. Unuvar, and A. K. Mukherjee, "Continuous functionally graded boron carbide-aluminum nanocomposites by spark plasma sintering," *Materials Science and Engineering A*, vol. 493, no. 1-2, pp. 251–255, 2008.
- [47] D. V. Dudina, D. M. Hulbert, D. Jiang, C. Unuvar, S. J. Cytron, and A. K. Mukherjee, "In situ boron carbide-titanium diboride composites prepared by mechanical milling and subsequent Spark Plasma Sintering," *Journal of Materials Science*, vol. 43, no. 10, pp. 3569–3576, 2008.
- [48] D. M. Hulbert, D. Jiang, D. V. Dudina, and A. K. Mukherjee, "The synthesis and consolidation of hard materials by spark plasma sintering," *International Journal of Refractory Metals and Hard Materials*, vol. 27, no. 2, pp. 367–375, 2009.
- [49] L. Nikzad, R. Licheri, T. Ebadzadeh, R. Orrù, and G. Cao, "Effect of ball milling on reactive spark plasma sintering of B_4C-TiB_2 ," *Ceramics International*, vol. 38, no. 8, pp. 6469–6480, 2012.
- [50] B. B. Bokhonov, L. P. Burleva, D. R. Whitcomb, and Y. E. Usanov, "Formation of nano-sized silver particles during thermal and photochemical decomposition of silver carboxylates," *Journal of Imaging Science and Technology*, vol. 45, no. 3, pp. 259–266, 2001.
- [51] T. Holland, D. Hulbert, U. Anselmi-Tamburini, and A. Mukherjee, "Functionally graded boron carbide and aluminum composites with tubular geometries using pulsed electric current sintering," *Materials Science and Engineering A*, vol. 527, no. 18-19, pp. 4543–4545, 2010.
- [52] W. Liu and M. Naka, "In situ joining of dissimilar nanocrystalline materials by spark plasma sintering," *Scripta Materialia*, vol. 48, no. 9, pp. 1225–1230, 2003.
- [53] T. Matsubara, T. Shibutani, K. Uenishi, and K. F. Kobayashi, "Fabrication of TiB_2 reinforced Al_3Ti composite layer on Ti substrate by reactive-pulsed electric current sintering," *Materials Science and Engineering A*, vol. 329–331, pp. 84–91, 2002.
- [54] M. Mulukutla, A. Singh, and S. P. Harimkar, "Spark plasma sintering for multi-scale surface engineering of materials," *Journal of Metals*, vol. 62, no. 6, pp. 65–71, 2010.
- [55] A. Singh, S. R. Bakshi, D. A. Virzi, A. K. Keshri, A. Agarwal, and S. P. Harimkar, "In-situ synthesis of $TiC/SiC/Ti_3SiC_2$ composite coatings by spark plasma sintering," *Surface and Coatings Technology*, vol. 205, no. 13-14, pp. 3840–3846, 2011.

Research Article

Dense Nanostructured Nickel Produced by SPS from Mechanically Activated Powders: Enhancement of Mechanical Properties

F. Naimi,¹ L. Minier,¹ S. Le Gallet,¹ H. Couque,² and F. Bernard¹

¹ ICB UMR 6303 CNRS/Université de Bourgogne, BP 47870, 21078 Dijon Cedex, France

² Nexter Munitions, 7 route de Guerry, 18000 Bourges, France

Correspondence should be addressed to F. Bernard; fbernard@u-bourgogne.fr

Received 25 February 2013; Accepted 16 April 2013

Academic Editor: Faming Zhang

Copyright © 2013 F. Naimi et al. This is an open access article distributed under the Creative Commons Attribution License, which permits unrestricted use, distribution, and reproduction in any medium, provided the original work is properly cited.

An investigation was performed to evaluate the potential of the spark plasma sintering process in producing dense nanostructured materials. Microstructured and nanostructured nickel was sintered by SPS starting from nickel powder (APS 3–7 μm) in the as-received state and after a mechanical activation using a high-energy ball mill. First, a sintering study to determine SPS processing conditions to reach full densification was carried out with specimens 50 mm in diameter and 10 mm in height. In a second step, an experimental investigation was undertaken with dense nickel disks to generate tensile properties. The tensile tests were performed at a strain rate of 10^{-3} s^{-1} with specimens 16 mm in gage length and 4 mm in gage diameter. Tensile ductility in excess of 40% was reached with the microstructured nickel. For the nanostructured nickel, high yield stresses in excess of 600 MPa were measured with a tensile ductility of 30%. These results were analyzed through densification and microstructure measurements.

1. Introduction

The term “nanomaterials” is usually used for nanostructured or nanophased materials, in which the dimension of grains is ranged from 1 to 100 nanometers, which have specific characteristics due to the modification of the surface/volume ratio. However, if many examples in the literature can easily illustrate these effects in electronics, magnetic recording, cosmetics, catalysis, etc. [1–7], it is very difficult to access to the evolution of mechanical properties versus the grain size. The relative dearth of experimental data on mechanical properties of nanomaterials has been attributed to the difficulty in preparing significant size dense specimens [8]. Nevertheless, some examples showed clearly that the improvement of mechanical properties of metals and alloys is historically related to a refinement of microstructure. Indeed the decreasing of the grain size increases the yield strength according to the Hall-Petch law [9–11]. The development of substructure limits the dislocation motions via the precipitation—creation of dislocation cells (10–200 nm)—and, consequently, reinforces the compromise between yield stress and ductility [12].

For example, in the case of tungsten alloys prepared by powder metallurgy and thermal transformation, an increasing by two orders of magnitude of strength resistance is observed [13].

Material processing via powders has the potential of controlling the material microstructure at a nanoscale. The process begins with the synthesis of powders. It is now possible to synthesize powders with a grain size in the nanorange for a wide range of ceramic and metallic compounds from three different ways: (i) physical route such as evaporation-condensation processes and laser pyrolysis [14–21], (ii) chemical route including soft chemistry, sol-gel methods, and hydrothermal synthesis which can be extended to supercritical conditions [22–25], and (iii) the mechanical route in which powders are “nanostructured” (as opposed to those “nanosized”), for example, powders of metallic alloys with a nanodistribution of phases within each particle, can be obtained by mechanical alloying [26–30].

Then, it is necessary to add a consolidation step to obtain dense materials. Different processes have been developed to consolidate nanoparticles [31–34]. Rawers [34] has reviewed

the main methods to densify nanomaterials and discussed the advantages and disadvantages. All the methods are based on the application of high pressure but also of high temperature to affect densification through particle deformation and mass transport. One promising technique is the hot pressing of mechanically milled powders, in which the careful control of processing parameters (time, temperature, and pressure) makes possible the fabrication of fully dense nanostructured samples [33, 34]. However, the high-temperature treatment leads to significant grain coarsening (Ostwald ripening). Usually, for limiting the grain growth, it is necessary to decrease the temperature, for example, by the use of very high pressure (4 GPa in some cases) in order to plastically deform the nanometric grains [35]. An alternative route to enhance densification and avoid excessive grain growth is the so-called fast firing method [36] and fast sintering techniques, usually named SPS (spark plasma sintering, [37]). The aim of these methods is to reduce the time of exposure to high temperatures. An example is given in the case of W-2Y nanopowders prepared by ball milling and then sintered in vacuum [38]. In a recent review containing 1005 papers, Orrù et al. [39] report the potentiality of SPS technology to produce “in a short time” various types of materials. Indeed, SPS is one of the most attractive techniques for producing innovative materials with a moderate cost and, for some cases, enhanced properties [37, 39]. The SPS technique allows rapid heating through Joule effect by applying to the powders and environmental tools (die, punches, and spacers usually in graphite) a high current (~ 1000 to $30\,000$ A). It allows producing materials from 10 to 100 times faster as compared to classical powder metallurgy techniques. Rapid heating is performed and sintering is greatly enhanced, allowing the production of a dense material with a limited grain coarsening. Exceptional results are obtained such as a limitation of grain growth in the case of ceramics [40–42], or of metallic composites [43, 44].

The aim of the present research work was to fabricate dense nanostructured nickel in order to take advantage of the improvement of mechanical properties with reduced grain size. One of the challenges was to limit the grain coarsening even in significant size specimens, through the control of the SPS processing parameters (such as heating rate, sintering temperature, holding time, and pressure). However, it is also crucial to control the production of nanopowders in order to get powders having a nanometric size and a size distribution as narrow as possible. Such a control is not obvious due to the large reactivity of nanoparticles. That is why as-milled powders have been produced using high-energy ball milling. Indeed, the milling process leads to both the reduction in the crystallite size and the accumulation of defects in powder particles. The other interest of ball milling is the possibility to form agglomerates with a micrometer size (size usually available with commercial ones) containing nanocrystallites. Moreover, the reactivity towards ambient air of mechanically activated powder in which the specific surface area is reduced in comparison with individual nanoparticles produced, for example, by a chemistry route. Consequently, the storage, the transport, and the handling of mechanically activated Ni agglomerates are facilitated.

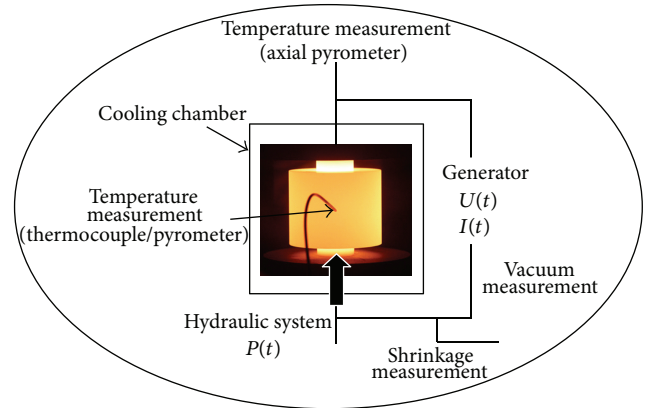


FIGURE 1: Description of the SPS process.

In the present work, Ni milled powders were prepared using high-energy planetary mill and were subsequently consolidated as disk of 50 mm in diameter using the SPS process, from which tensile specimens were extracted for mechanical characterization.

2. Experimental Procedure

The investigation has been performed by evaluating the mechanical properties of nickel samples sintered by SPS from a mechanically activated powder. Mechanical properties are then compared with those of a reference sample obtained by electrodeposition. The process to produce dense nanostructured Ni from a micrometric commercial powder (commercial Ni from a micrometric commercial powder) consists in two steps [45, 46]: (i) mechanical activation of the elemental powder by a short-duration treatment in a high-energy planetary milling (milled powder) and (ii) densification of Ni in one step by flash sintering using SPS equipment.

The dimensions of sintered specimens must be sufficient to perform tensile tests, that is, 50 mm in diameter and 10 mm in height. Conditions of powder preparation were selected to produce per vial one batch necessary to perform one SPS sample. Consequently, 120 g of elemental powder Ni (Alfa Aesar, APS 3–7 μm in particle size, 99.9% purity) was milled in a planetary ball vario-mill Fritsch Pulverisette 4 [47, 48]. Based on previous works [49, 50], a specific ball milling condition was established at 250 rpm (rotation per minute) for the disk rotation speed and -50 rpm for the absolute vial rotation speed. The charge ratio C_R (steel ball to powder mass ratio) was 7. The powder being constituted of quite abrasive materials, a short duration of milling has been selected to avoid any contamination of the product by the milling tools (8 h uninterrupted). Moreover to limit this contamination but also to increase the yield of nanostructured powder, three millings without cleaning milling tools have been carried out. Under these conditions, the ductile character of powders induced the formation of Ni coating on the vial surface acting as a protective liner against the abrasion on the surface of tempered iron tools. In addition, the milling parameters were selected to be sufficiently long

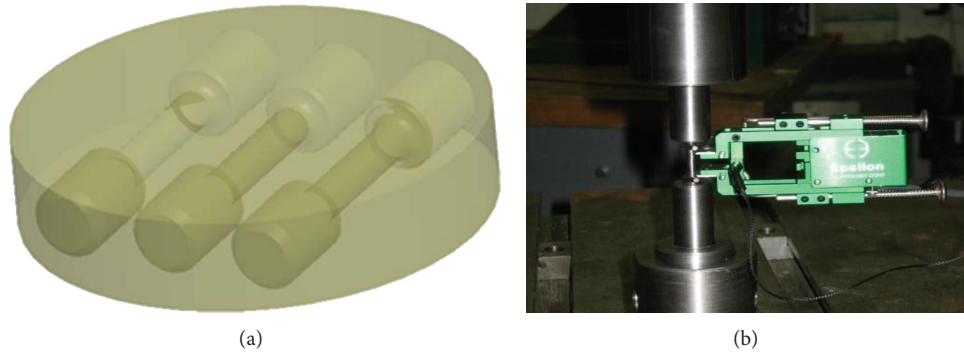


FIGURE 2: Tensile test: (a) tensile specimens layout in the sintered disc with a diameter of 50 mm in which three specimens were extracted, (b) tensile specimen with installed extensometer.

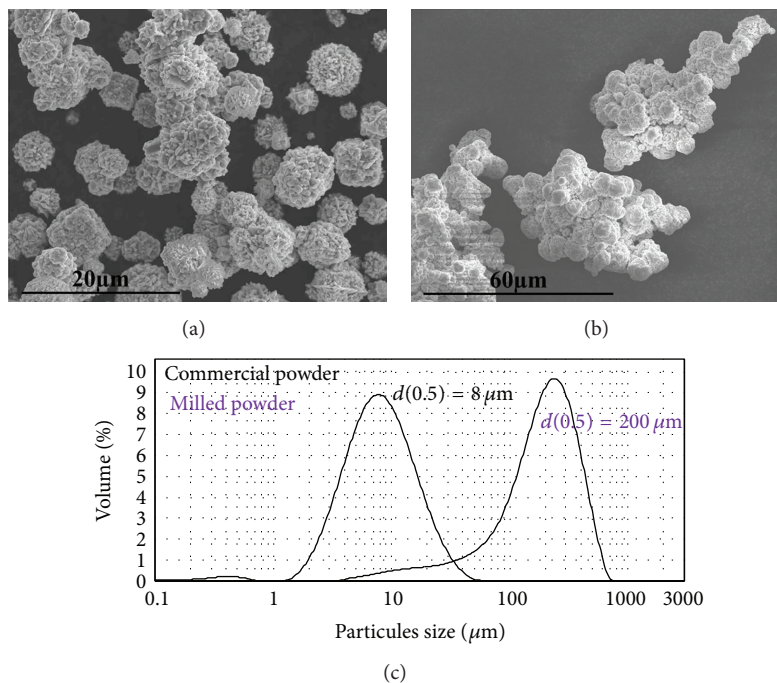


FIGURE 3: SEM observations of commercial Ni powder (APS 3–7 μm) and (a) milled Ni powder (b) including the particle size distribution determined by laser granulometry for both systems (c).

for producing mechanically activated agglomerates. Many studies reported the existence of correlation between ball milling conditions and microstructure of milled powders [51, 52]. It was determined that there is an interval of time for which the crystallite size and the dislocation density are not time dependent whereas the twin faults density increased proportionally to milling duration. Other authors [51] showed that in the case of nanostructured Cu powder prepared by ball milling a frequency of shocks in range of 6–17 Hz does not affect the microstructure. On the other hand, crystallite size, dislocation and, twin densities are function of the energy of shocks. From the kinetic model developed by Abdellaoui and Gaffet [48], the change of speed rotations of disk and vials led to an injected power during the ball milling process which can be expressed as the energy of shocks (E)

and the frequency of shocks (F). In this work, energy and frequency of shocks are, respectively, equal to 0.08 J and 9 Hz.

Sintering is the second step and is required to obtain nanostructured materials with a density perfectly controlled. In the case of SPS, the sintering is due to the simultaneous application of direct current pulses of very high intensity (several thousands of amperes) and of a uniaxial pressure to the encapsulating system (Figure 1). The Ni powders were sintered in the spark plasma sintering apparatus (HPD125 apparatus, FCT System GmbH). Dense samples of 50 mm diameter and 10 mm thickness were sintered into a graphite die (100 mm outer diameter and 50 mm height). The powders were first cold compacted in the die lined with graphite foil (graphite foil is also inserted between the powder and the punches) at the sintering pressure during 5 minutes. The die

containing the cold-compacted sample was enveloped with a carbon felt to reduce the radiation heat losses from the outer surface. The temperature was monitored by a K-type thermocouple located in a hole at 3 mm far from the sample and half height of the die.

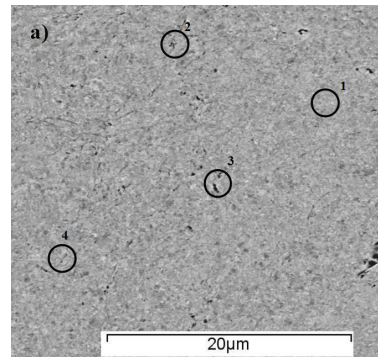
Before characterization, the samples were first polished with 180-grit silicon carbide and up to $1\ \mu\text{m}$ with diamond paste and, finally, cleaned in an ultrasonic ethanol bath in order to remove surface contamination from graphite foil. The relative density is obtained by the ratio of the bulk density of the sintered samples (determined using the Archimedes method in distilled water) to the theoretical density. Each value is an average of three measurements. X-ray powder diffraction (XRD) measurements were performed with a Bruker-AXS D8 Advance diffractometer ($\text{CuK}\alpha$ radiation, $\lambda = 0.154051\ \text{nm}$) using a super speed VANTEC-1 detector. Pattern decomposition was carried out with the profile-fitting program TOPAS using Le Bail's method [49].

A scanning electron microscope (SEM JEOL JSM-7600F) with a field emission gun (FEG) and coupled with (i) a LINK OXFORD Energy Dispersive X-Ray Spectrometry (EDXS) and (ii) an electron backscattering diffraction (EBSD) detector was used to analyze, respectively, the grain morphology and the local chemical composition of materials. The microstructures of powders (commercial and milled) were characterized by embedding and polishing them in order to perform an analysis of the cross section of grains or agglomerates and SPS materials were cut along the axial direction. The samples were observed under secondary or backscattered electron modes and analyzed by orientation imaging microscopy (OIM). The EBSD Kikuchi patterns were posttreated using CHANNEL 5.0 software in order to obtain information on grain size distribution. The grain maps were reconstructed assuming that the real grains contain more than two adjacent pixels with the same orientation and the grain boundary angles were higher than 4° .

Finally, in order to evaluate the mechanical properties, three tensile specimens were extracted from SPS-sintered samples in relation with the schematic representation given on Figure 2. Such a procedure allows us to perform, for each as-sintered material, three tests. The tensile tests were performed at a strain rate of $10^{-3}\ \text{s}^{-1}$ with specimens 16 mm in gage length and 4 mm in gage diameter using a Testwell machine equipped with a load cell of capacity 5000 daN. The gage length elongation was measured with an extensometer Epsilon over a gage length of 10 mm.

3. Experimental Results

3.1. Mechanical Activation Stage. The powder issued from the high energy ball milling does not keep the spherical morphology of the commercial powder grains (Figure 3). Mechanically activated powders in comparison to commercial Ni powders appear as large agglomerates due to successive fracture/welding process occurring during the milling. Indeed, the size of commercial powder grain increases from $8\ \mu\text{m}$ to $200\ \mu\text{m}$ ($d(0.5)$) measured by laser granulometry (Figure 3(c)) whereas the crystallite size determined from



(a)

Spot	At.Ni (%)	At.O (%)	At.Cr, Fe (WDS) (%)
1	100	0	<100 ppm
2	96.8	3.2	<100 ppm
3	93.8	6.2	<100 ppm
4	100	0	<100 ppm

(b)

FIGURE 4: (a) BSE micrographs showing the transverse cut of milled Ni agglomerates. The dark zones correspond to oxygen contamination and pores in agreement with (b) EDX analyses reported in the table in which WDS (Fe, Cr) analysis were added.

XRD peak profile analysis decreases from 250 nm to 52 nm. This mechanical activation has allowed the formation of micrometric agglomerates constituted of nanocrystallites. In addition, the microdistortion rate corresponding to an increasing of defect density is also modified but the magnitude seems to be lower ($\sim +10\%$). For the selected milling condition, no contamination from the milling tools was detected by both EDX-SEM and XRD analyses. Indeed, two chemical analyses performed by EDX and WDS on milled Ni-agglomerate confirmed that no Cr and Fe contamination was observed. Only few areas located on agglomerate boundary are composed of oxygen (Figure 4). However, oxides are not detected by XRD (in the detection limit of the apparatus). This study confirms the interest to use high-energy ball-milling without cleaning vials in order to avoid any contamination.

Figure 5 obtained from SEM-EBSD analysis permits to determine a grain size distribution (inverse pole figure) and a defect density (kernel analysis) on commercial (Figure 5(a)) and mechanically activated (Figure 5(b)) nickel powders. The white areas on commercial powder figures correspond to the resin. These figures confirm the XRD analyses and show that the high energy ball milling process allows reducing the crystallite size (Figure 5(b)-top). Moreover, many defects have been introduced (Figure 5(b)-down). Indeed, the inverse pole figure for the milled powder exhibits a large grain size distribution including zones containing large grains and others composed with finer grains. In fact mechanical activation of Ni powder allows to obtain a good combination

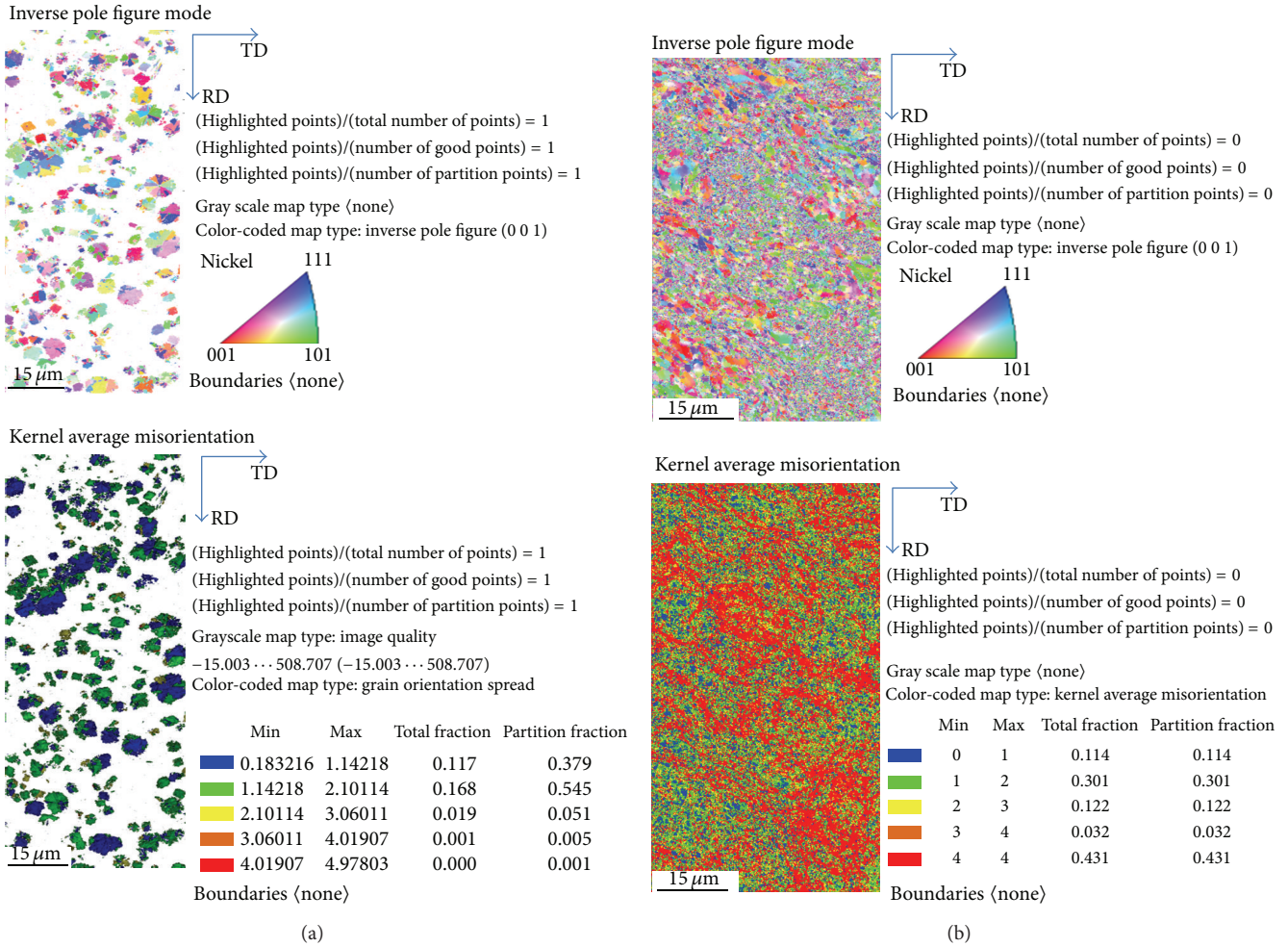


FIGURE 5: For both (a) commercial and (b) milled Ni powders, inverse pole figure mode and kernel average misorientation have been plotted in order to establish, respectively, the average grain size of particles (top) and a defect density inside powders (down).

between large and fine particles. Moreover, the density of defects introduced during the milling is significant in comparison with commercial powders in which the density of defect is negligible. This density of defects observed on EBSD images is higher than that obtained by XRD analysis for which the contribution of microdistorsion seems to be underestimated. In addition, the lattice strain has been found to increase in the first stage of grain deformation, to reach a maximum, and then to decrease upon further millings [26, 27]. This behavior has been attributed to strain release which can be observed during the milling especially when the plastic deformation mechanisms are activated via formation and movement of dislocations to grain boundary gliding. Consequently, it is essential to study the influence of the crystallite size reduction and defect density multiplication on the sintering, in particular, on the grain coarsening and consolidation stages.

3.2. Sintering Stage. In order to evaluate the sintering behavior of each powder (i.e., commercial and milled powders), a dilatometric study inside the SPS machine was performed.

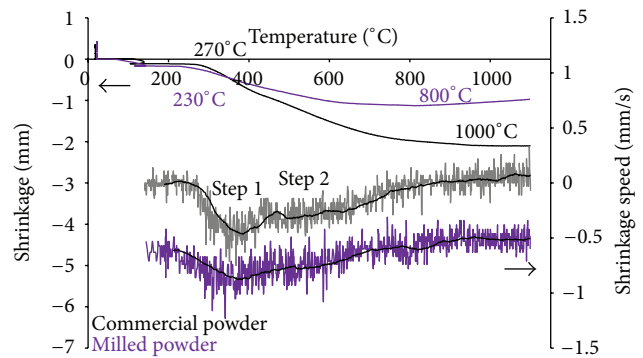


FIGURE 6: Dilatometric curves of sintering of the commercial powder (270–1000°C) and the mechanically activated Ni powder (230–800°C).

The SPS cycle consisted of a sintering at 1000°C under 50 MPa without dwelling time. A heating rate of 50°C/min has been applied. This comparative study presented Figure 6 which shows the sintering behavior of both powders is different. In

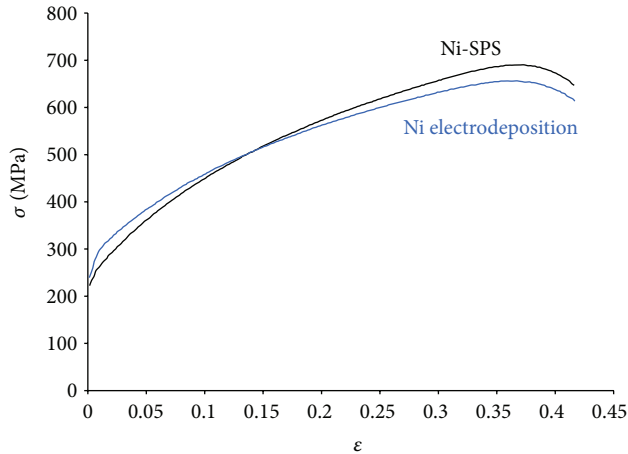


FIGURE 7: True stress-strain responses of the micrometric Ni prepared by electrodeposition and by SPS.

particular, the temperatures corresponding, respectively, at the beginning (230°C instead of 270°C) and at the end (800°C instead of 1000°C) of sintering decrease when a mechanical activation stage on the commercial powder is used. This effect can be attributed to the microstructure difference in terms of crystallite size and defect density as it was observed on EBSD analysis presented on Figure 5. In addition, the shrinkage curve of Ni commercial powder is composed of two steps, firstly between 270°C and 400°C and secondly between 400°C and 1000°C whereas such a slope change is not observed for the milled powder (Figure 6).

This different sintering behavior can be explained by the difference of morphology between the two powders. Indeed, the commercial one, due to its thistle-like morphology, has in a first step, and before starting to sinter, its surface which becomes smooth. The optimization of the sintering conditions of the micrometric Ni powder has been performed in a previous work by the establishment of a SPS sintering map [50–52, 59, 60]. Accordingly, the commercial Ni powder was sintered at 750°C under 100 MPa during 5 minutes. The heating rate was divided into two steps. The heating rate was $200^{\circ}\text{C}/\text{min}$ until 600°C and decreased at $50^{\circ}\text{C}/\text{min}$ for the second step. The density of the sample was $99 \pm 0.5\%$. Tensile tests were performed on this SPS sintered sample and compared with the reference Ni prepared by electrodeposition (99% dense) (Figure 7). The yield stress, the hardening characteristics, and the ductility of the micrometric SPS sintered specimen and electrodeposition one are totally comparable. Such a comparison validates the SPS process for producing dense nickel with similar properties to the reference material (electrodeposition Ni). Consequently, the sample elaborated from the Ni milled powder has been sintered in the same conditions (sintering parameters and tools). The density of this sintered specimen is equal to $96 \pm 0.5\%$ only. This density difference could be attributed to the plasticity of the milled powder agglomerates which is smaller than that of the commercial powder. As expected, the nanostructured Ni sample exhibits a higher mechanical strength than the micrometric sample (Figure 8). A nonnegligible ductility of

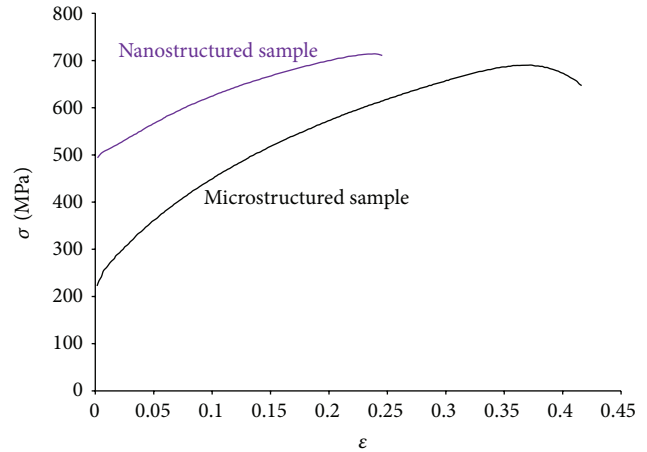


FIGURE 8: True stress-strain response of the microstructured and the nanostructured nickel elaborated by SPS under a pressure of 100 MPa.

25% was reached with the nanostructured sample. Figure 9 compares the fractographs of the micrometric nickel and the nanostructured nickel both elaborated by SPS under a pressure of 100 MPa. They both exhibit stretched voids typical of ductile failure. The micrometric nickel reveals a continuous net of stretched voids of size ranging from 2 to $10\ \mu\text{m}$, while the nanostructured nickel reveals a finer stretched void structure with a somehow continuous network of voids ranging from 0.5 to $2\ \mu\text{m}$. In addition, the nanostructured nickel exhibits large voids spherical in shape of size ranging from 5 to $10\ \mu\text{m}$. Because of their spherical aspects, these voids are believed to originate from pores as the residual porosity is high in excess of 4%.

To improve the density of the sample elaborated from the milled powder, the SPS process has to be optimized. Precisely, the beneficial effect of the SPS process on the densification was demonstrated elsewhere showing that the density is improved with the heating rate, the applied pressure, and the holding time up to a critical value [39]. However, heating rate and holding time do not provide a significant improvement and an increasing of the sintering temperature could lead to grain growth, which will be harmful to the mechanical properties. On the contrary, an increasing of the pressure allows decreasing the sintering temperature while improving densification. So, the strategy adopted has been to apply higher pressure to enhance the contribution of the plastic deformation to densification and bonding. The high stress enhances the plastic strain controlling pore closure. Also, the stress plays a significant role in stress-assisted densification mechanisms. In addition, the extensive plastic deformation under high stress results in the destruction of any continuous surface oxides on powder particles which may degrade bonding and properties. The high pressure applied may also have a beneficial effect of slowing down grain growth because of the reduction of free volumes in grain boundaries which favor atomic jumps across the boundary.

Therefore, the effect of the pressure has been investigated. Because of the poor flexural strength of the graphite, the

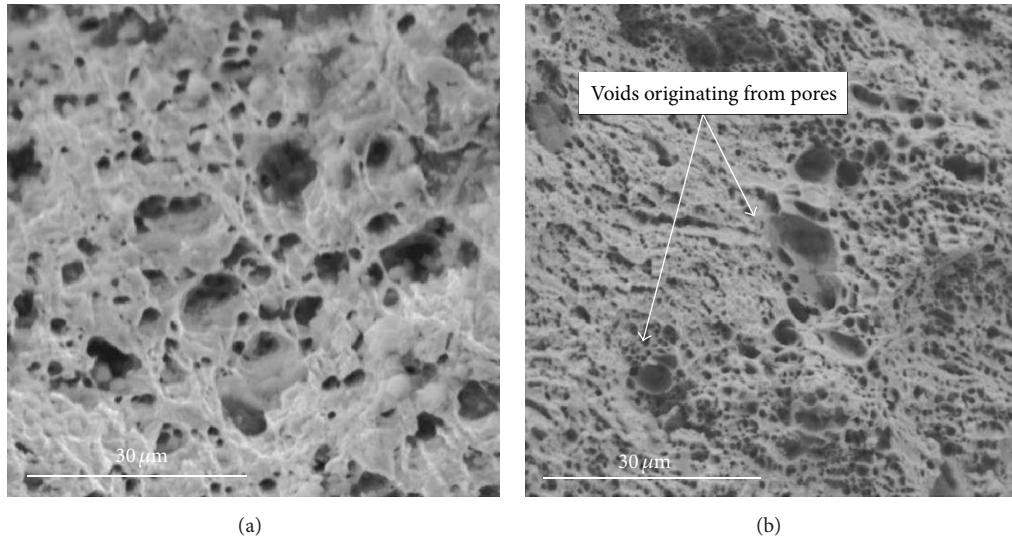


FIGURE 9: Fractographs of the tensile specimens for the microstructured (a) and the nanostructured (b) nickel elaborated by SPS under a pressure of 100 MPa.

uniaxial pressure is limited to 100 MPa. Consequently, specific tungsten carbide-cobalt tools including cylindrical die of 100 mm outer diameter and 50 mm height and punches have been designed. However, the sample densification is influenced by the nature of SPS tools. Despite a similar sintering temperature, the sample temperature can be different [61]. Therefore, the electrical and thermal conductivities of WC-Co tools impose to modify the thermal cycle applied to mechanically activated Ni powder. In addition, applying very high pressures will strongly affect the sintering behavior by changing the densification temperature. In order to evaluate the influence of the tool on the sintering, a dilatometric curve of the milled powder has been realized from the following sintering conditions: sintering at 700°C under 200 MPa with a 200°C/min heating rate without dwelling time. According to this curve the sintering of milled Ni powder has been performed at 550°C during 10 minutes under 200 MPa. As previously mentioned, the heating rate was divided into two steps. The heating rate was 200°C/min until 450°C and decreased at 50°C/min for the second step. The density of this sample was close to $98 \pm 0.5\%$.

On Figure 10, it appears that the sintered nanostructured Ni at 200 MPa has higher mechanical strength (~ 590 MPa) than the milled powder sintered under 100 MPa (~ 500 MPa). In addition, the ductility has been improved from 25 to 35%.

As shown in Figure 11, both nanostructured nickel samples exhibit a continuous network composed of stretched voids with size ranging from 0.5 to 2 μm . For the nanostructured nickel elaborated under high pressure (Figure 11(b)), small spherical voids in size, less than 1 μm , have been observed as well. However their sizes similar to the size of the stretched voids indicate that the residual porosity may play a minor role in the final failure process of this nanostructured nickel.

Finally, the yield strength of 590 MPa is three times higher than the yield strength of electrodeposition sample. In fact

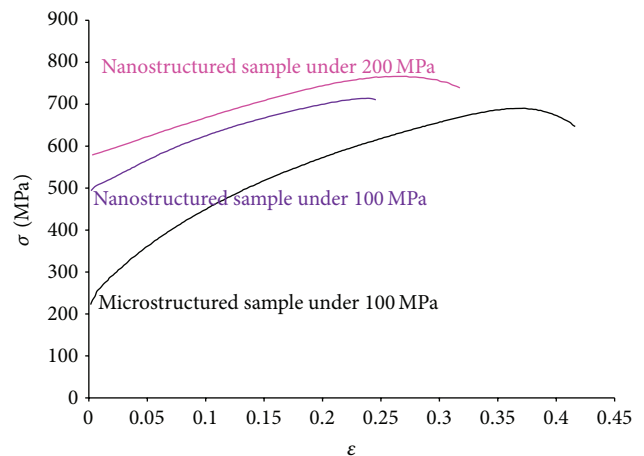


FIGURE 10: True stress-strain response of the micronic sample obtained by electrodeposition and sample obtained by SPS; microstructured nickel and milled nickel under 100 MPa and 200 MPa.

the strength observed is approximately consistent with what would be expected under the Hall-Petch relationship. The second interesting feature is that a plastic strain of 30% is an observed event at this high strength level. Most nanophase nickel alloys (grain size < 100 nm) reported previously did not exhibit such pronounced plastic strain before fracture. It is surmised that the premature failure observed in these materials may at least partly be due to the presence of a significant amount of pores, impurities. The behavior of this nanostructured nickel may lead to the presence of “bi-modal” microstructure which is composed of larger grain dispersed in the finer grain matrix as observed on Figure 12.

The EBSD-SEM image on this sample shows clearly these two areas. A sample elaborated in the same conditions but

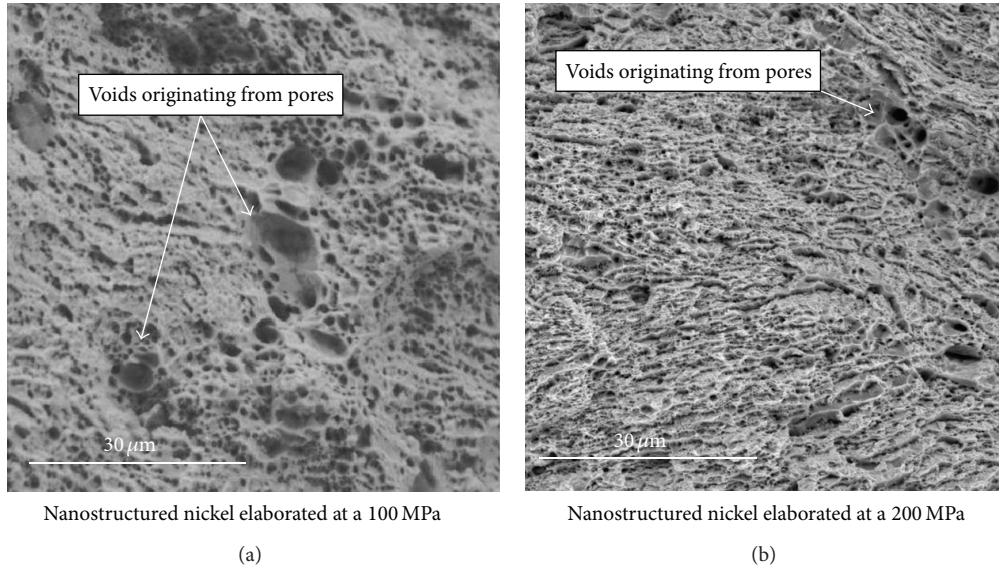


FIGURE 11: Fractographs of the tensile specimens for the two nanostructured nickels.

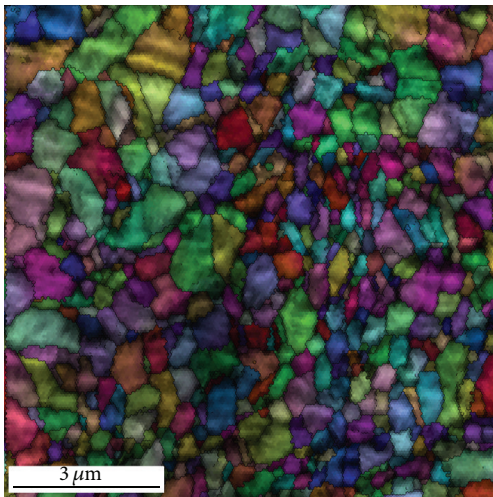


FIGURE 12: EBSD-SEM images of the sample elaborated from the milled powder sintered under 200 MPa.

with the commercial powder has a larger and more homogeneous microstructure. Consequently, it will be interesting to control this combination between larger gains and finer ones in order to understand the role of each grain population on mechanical properties especially on strength and ductility. However, in comparison with Hall-Petch plot for nickel processed by different processing routes (Figure 13), it is clearly shown that the dense nanostructured nickel (98% with an average crystallite size of 130 nm determined by XRD analysis) produced by mechanically activated SPS process is in agreement (our result is symbolized by a open circle) with the dashed line which represents a linear fit on data generated by electrodeposition by Ebrahimi et al. [53] and Xiao et al.

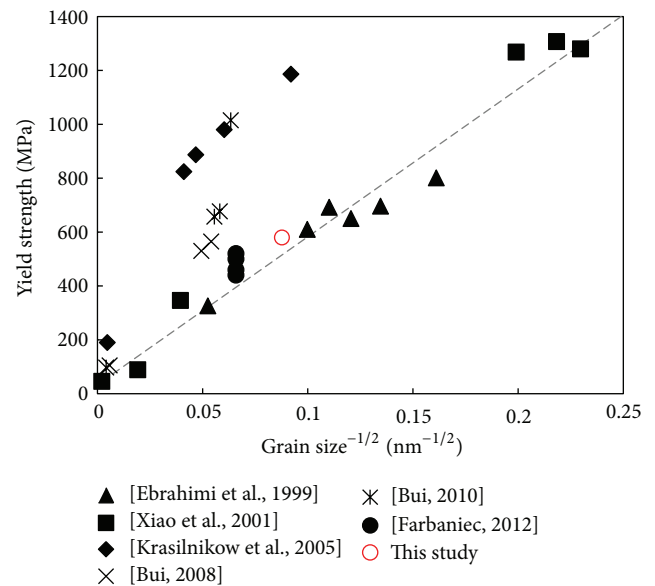


FIGURE 13: Hall-Petch plot for nickel processed by different processing routes (see [53–58]).

[54]. Other data reported in the figure were generated with nanopowders sintered by SPS [55] and HIP [56] and with micrometric nickel plastically deformed by equal channel angular pressing [57] and by dynamic plastic deformation [57]. If the latest technology is another potential mean to generate ultrafined and nanostructured nickel, the sintering of nanopowders, compared to mechanically activated powders, reveals its limitations, as the high density of oxides provides higher strength with a drawback of exhibiting no capacity to deform plastically.

4. Conclusion

The method of dense nanostructured Ni preparation used in the present work is the mechanically activated spark plasma sintering (MASPS). The process to fabricate dense nanomaterials starting from micrometric commercial powders consists in two main steps: (a) mechanical activation (MA) using a high energy ball mill and (b) densification using the SPS device. In the former, mixture of pure elemental powders of Ni was milled in a Fritsch planetary ball mill (the so-called vario-mill P4 Pulverisette). Finally, the milled nickel powders have been sintered by SPS. The sintering conditions from these mechanically activated powders will be established in order to identify the “SPS window” for which it is possible to consolidate these powders without a coarsening of particles or with a control of the grain growth from a modification of the applied pressure (200 MPa). Consequently, dense nanostructured nickel samples have been produced (98%). These latter presented a specific and interesting microstructure which combines larger particles with smaller ones.

In addition, in order to use a representative sample for performing mechanical tests, it will be essential to control these nanostructures in larger sample (diameter greater than 50 mm). Finally, these Ni nanostructured samples were tested using classical static mechanical tests such as traction tests and compared to the literature data. These nanostructured nickel specimens which had yield strength of 600 MPa with ductility close to 30% are in agreement with the expected Hall-Petch relationship.

Acknowledgments

Thanks are due to M. Pascal Vanneau from Nexter Munitions who realized the tensile tests and to MM. Bruno Salesse and Fabien Hemeret from Nexter Systems who performed the fractographies of the tensile specimens. Thanks are also due to M. Frédéric Herbst who performed SEM-EBSD observation and Mme Isabelle Gallet for ball milling preparation.

References

- [1] M. Lahmani, C. Bréchnignac, and P. Houdy, *Nanomaterials and Nanochemistry*, Springer, Berlin, Germany, 2007.
- [2] G. Schmid, “Nanoclusters: Building blocks for future nanoelectronic devices?” *Advanced Engineering Materials*, vol. 3, pp. 737–743, 2001.
- [3] C. Piriot, “Preparation and characterization of carbon nanotube/polyacrylonitrile composites,” *Advanced Engineering Materials*, vol. 4, pp. 109–114, 2002.
- [4] C. Edser, “Nanopowders seek commercial roles to repay R&D effort,” *Metal Powder Report*, vol. 54, no. 4, pp. 11–13, 1999.
- [5] J. M. Capus, “Prospects look promising for nanopowders,” *Metal Powder Report*, vol. 56, no. 1, pp. 12–14, 2001.
- [6] B. H. Kear and G. Skandan, “Overview: status and current developments in nanomaterials,” *International Journal of Powder Metallurgy*, vol. 35, no. 7, pp. 35–37, 1999.
- [7] *Nanomatériaux*, Observatoire français des techniques avancées, 2001.
- [8] H. Hahn and K. A. Padmanabhan, “A model for the deformation of nanocrystalline materials,” *Philosophical Magazine B*, vol. 76, no. 4, pp. 559–571, 1997.
- [9] E. O. Hall, “The deformation and ageing of mild steel: III Discussion of results,” *Proceedings of the Physical Society B*, vol. 64, no. 9, article 303, pp. 747–753, 1951.
- [10] N. J. Petch, “Cleavage strength of polycrystals,” *Journal of Iron and Steel Institute*, vol. 174, pp. 25–28, 1953.
- [11] H. Gleiter, “Nanocrystalline materials,” *Progress in Materials Science*, vol. 33, no. 4, pp. 223–315, 1989.
- [12] S. Zaefferer, “Investigation of the correlation between texture and microstructure on a submicrometer scale in the TEM,” *Advanced Engineering Materials*, vol. 5, no. 8, pp. 607–613, 2003.
- [13] G. Nicolas, “Alliages Lourds de W-Ni-Fe à très haute caractéristiques mécaniques et procédé de fabrication desdits alliages,” Brevet FR 262209 (A1), 1989.
- [14] J. Bigot, A. G. Goursat, G. Vernet, J. F. Rimbart, J. Foulard, and T. Sarle, 1983, French Patent no. 8307414.
- [15] Y. Champion and J. Bigot, “Preparation and characterization of nanocrystalline copper powders,” *Scripta Materialia*, vol. 35, no. 4, pp. 517–522, 1996.
- [16] Y. Champion and J. Bigot, “Synthesis and structural analysis of aluminum nanocrystalline powders,” *Nanostructured Materials*, vol. 10, no. 7, pp. 1097–1110, 1998.
- [17] M. Umemoto, M. Udaka, K. Kawasaki, and X. D. Liu, “Characterization of mechanically alloyed Ti-Zr-Cu-Ni powders,” *Journal of Materials Research*, vol. 13, no. 6, pp. 1511–1516, 1998.
- [18] Y. Moriyoishi, M. Futaki, S. Komatsu, and T. Ishigaki, “The preparation and characterization of ultrafine tungsten powder,” *Journal of Materials Science Letters*, vol. 16, no. 5, pp. 347–349, 1997.
- [19] W. R. Cannon, S. C. Danforth, J. H. Flint, J. S. Haggerty, and R. A. Marra, “Sinterable ceramic powders from laser-driven reactions: I, process description and modeling,” *Journal of the American Ceramic Society*, vol. 65, pp. 324–331, 1982.
- [20] R. Dez, F. Ténégal, C. Reynaud, M. Mayne, X. Armand, and N. Herlin-Boime, “Laser synthesis of silicon carbonitride nanopowders; structure and thermal stability,” *Journal of the European Ceramic Society*, vol. 22, no. 16, pp. 2969–2979, 2002.
- [21] X. X. Bi, B. Ganguly, G. P. Huffman, F. E. Huggins, M. Endo, and P. C. Eklund, “Nanocrystalline α -Fe, Fe_3C , and Fe_7C_3 produced by CO_2 laser pyrolysis,” *Journal of Materials Research*, vol. 8, no. 7, pp. 1666–1674, 1993.
- [22] J. A. Darr and M. Poliakoff, “New directions in inorganic and metal-organic coordination chemistry in supercritical fluids,” *Chemical Reviews*, vol. 99, no. 2-3, pp. 495–541, 1999.
- [23] F. Cansell, C. Aymonier, and A. Loppinet-Serani, “Review on materials science and supercritical fluids,” *Current Opinion in Solid State and Materials Science*, vol. 7, no. 4-5, pp. 331–340, 2003.
- [24] Y. Hakuta, H. Hayashi, and K. Arai, “Fine particle formation using supercritical fluids,” *Current Opinion in Solid State and Materials Science*, vol. 7, no. 4-5, pp. 341–351, 2003.
- [25] F. Demoisson, M. Ariane, A. Leybros, H. Muhr, and F. Bernard, “Design of a reactor operating in supercritical water conditions using CFD simulations. Examples of synthesized nanomaterials,” *Journal of Supercritical Fluids*, vol. 58, pp. 371–377, 2011.
- [26] C. Suryanarayana, “Mechanical alloying and milling,” *Progress in Materials Science*, vol. 46, pp. 1–81, 2001.
- [27] E. Gaffet and G. Le Caer, “Mechanical processing for nanomaterials,” in *Encyclopedia of Nanoscience and Nanotechnology*, vol. 1,

- pp. 1–39, American Scientific Publishers, Stevenson Ranch, Calif, USA, 2004.
- [28] E. Gaffet, F. Bernard, J. C. Niepce et al., “Some recent developments in mechanical activation and mechanosynthesis,” *Journal of Materials Chemistry*, vol. 9, no. 1, pp. 305–314, 1999.
- [29] M. Abdellaoui and E. Gaffet, “A mathematical and experimental dynamical phase diagram for ball-milled Ni₁₀Zr₇,” *Journal of Alloys and Compounds*, vol. 209, no. 1-2, pp. 351–361, 1994.
- [30] E. Gaffet, M. Abdellaoui, and N. Malhouroux-Gaffet, “Formation of nanostructural materials induced by mechanical processings,” *Materials Transactions, The Japan Institute of Metals*, vol. 36, no. 2, pp. 198–209, 1995.
- [31] G. E. Fougere, L. Riester, M. Ferber, J. R. Weertman, and R. W. Siegel, “Young’s modulus of nanocrystalline Fe measured by nanoindentation,” *Materials Science and Engineering A*, vol. 204, no. 1-2, pp. 1–6, 1995.
- [32] G. E. Fougere, J. R. Weertman, and R. W. Siegel, “Processing and mechanical behavior of nanocrystalline Fe,” *Nanostructured Materials*, vol. 5, no. 2, pp. 127–134, 1995.
- [33] J. Rawers, G. Slavens, D. Govier, C. Doğan, and R. Doan, “Microstructure and tensile properties of compacted, mechanically alloyed, nanocrystalline Fe-Al,” *Metallurgical and Materials Transactions A*, vol. 27, no. 10, pp. 3126–3134, 1996.
- [34] J. Rawers, “Comparison of attrition milled, nanostructured, powder-compaction techniques,” *Nanostructured Materials*, vol. 11, no. 4, pp. 513–522, 1999.
- [35] J. Eckert, J. C. Holzer, C. E. Krill, and W. L. Johnson, “Structural and thermodynamic properties of nanocrystalline fcc metals prepared by mechanical attrition,” *Journal of Materials Research*, vol. 7, no. 7, pp. 1751–1761, 1992.
- [36] K. R. Venkatchari, D. Huang, S. P. Ostrander, W. A. Schulze, and G. C. Stangle, “Preparation of nanocrystalline yttria-stabilized zirconia,” *Journal of Materials Research*, vol. 10, no. 3, pp. 756–761, 1995.
- [37] M. Tokita, “Trends in advanced SPS spark plasma sintering systems and technology: functionally gradients materials and unique synthetic processing methods from next generation of powder technology,” *Journal of the Society of Powder Technology, Japan*, vol. 30, pp. 790–804, 1993.
- [38] M.-N. Avettand-Fenoël, *Influence des Paramètres de Broyage et de Frittage sur la Microstructure d’Alliages O.D.S à Base de Tungstène [Ph.D. thesis]*, 2003.
- [39] R. Orrù, R. Licheri, A. M. Locci, A. Cincotti, and G. Cao, “Consolidation/synthesis of materials by electric current activated/assisted sintering,” *Materials Science and Engineering R*, vol. 63, no. 4-6, pp. 127–287, 2009.
- [40] Z. Shen, M. Johnsson, Z. Zhao, and M. Nygren, “Spark plasma sintering of alumina,” *Journal of the American Ceramic Society*, vol. 85, no. 8, pp. 1921–1927, 2002.
- [41] G. Bernard-Granger and C. Guizard, “Spark plasma sintering of a commercially available granulated zirconia powder: I. Sintering path and hypotheses about the mechanism(s) controlling densification,” *Acta Materialia*, vol. 55, no. 10, pp. 3493–3504, 2007.
- [42] N. Millot, S. Le Gallet, D. Aymes, F. Bernard, and Y. Grin, “Spark plasma sintering of cobalt ferrite nanopowders prepared by coprecipitation and hydrothermal synthesis,” *Journal of the European Ceramic Society*, vol. 27, no. 2-3, pp. 921–926, 2007.
- [43] G. Cabouro, S. Chevalier, E. Gaffet, D. Vrel, N. Boudet, and F. Bernard, “In situ synchrotron investigation of MoSi₂ formation mechanisms during current-activated SHS sintering,” *Acta Materialia*, vol. 55, no. 18, pp. 6051–6063, 2007.
- [44] G. Ji, T. Grosdidier, F. Bernard, S. Paris, E. Gaffet, and S. Launois, “Bulk FeAl nanostructured materials obtained by spray forming and spark plasma sintering,” *Journal of Alloys and Compounds*, vol. 434-435, pp. 358–361, 2007.
- [45] Z. A. Munir, F. Charlot, F. Bernard, and E. Gaffet, “One-step synthesis and consolidation of nano-phase materials,” U.S Patent no.6, 200,515, March 2001.
- [46] G. Ji, F. Bernard, S. Launois, and T. Grosdidier, “Processing conditions, microstructure and mechanical properties of hetero-nanostructured ODS FeAl alloys produced by SPS,” *Materials Science and Engineering*, vol. 559, pp. 566–573, 2013.
- [47] M. Abdellaoui, T. Barradi, and E. Gaffet, “Mechanism of mechanical alloying phase formation and related magnetic and mechanical properties in the FeSi system,” *Journal of Alloys and Compounds*, vol. 198, no. 1-2, pp. 155–164, 1993.
- [48] M. Abdellaoui and E. Gaffet, “The physics of mechanical alloying in a planetary ball mill: Mathematical treatment,” *Acta Metallurgica Et Materialia*, vol. 43, no. 3, pp. 1087–1098, 1995.
- [49] A. Le Bail, H. Duroy, and J. L. Fourquet, “Ab-initio structure determination of LiSbWO₆ by X-ray powder diffraction,” *Materials Research Bulletin*, vol. 23, no. 3, pp. 447–452, 1988.
- [50] L. Minier, *Influence du Frittage “Flash” sur l’Obtention de Nanostructures dans des Systèmes Métalliques et Céramiques [Ph.D. thesis]*, Université de Bourgogne, 2008.
- [51] H. Couque, L. Minier, C. Wolff et al., “High strain rate response of nanostructured and microstructured nickel elaborated by SPS,” in *Proceedings of the 18th DYMAT Technical Meeting*, H. Couque, Ed., pp. 57–64, 2008.
- [52] O. Boytsov, A. I. Ustinov, E. Gaffet, and F. Bernard, “Correlation between milling parameters and microstructure characteristics of nanocrystalline copper powder prepared via a high energy planetary ball mill,” *Journal of Alloys and Compounds*, vol. 432, no. 1-2, pp. 103–110, 2007.
- [53] F. Ebrahimi, G. R. Bourne, M. S. Kelly, and T. E. Matthews, “Mechanical properties of nanocrystalline nickel produced by electrodeposition,” *Nanostructured Materials*, vol. 11, no. 3, pp. 343–350, 1999.
- [54] C. Xiao, R. A. Mirshams, S. H. Whang, and W. M. Yin, “Tensile behavior and fracture in nickel and carbon doped nanocrystalline nickel,” *Materials Science and Engineering A*, vol. 301, no. 1, pp. 35–43, 2001.
- [55] Q.H. Bui, *Polycristaux à Grains Ultrafins Élaborés par Métallurgie des Poudres: Microstructure, Propriétés Mécaniques et Modélisation Micromécanique [Ph.D. thesis]*, University of Paris 13, Villetaneuse, France, 2008.
- [56] Q. H. Bui, G. Dirras, S. Ramtani, and J. Gubicza, “On the strengthening behavior of ultrafine-grained nickel processed from nanopowders,” *Materials Science and Engineering A*, vol. 527, no. 13-14, pp. 3227–3235, 2010.
- [57] N. Krasilnikov, W. Lojkowski, Z. Pakielka, and R. Valiev, “Tensile strength and ductility of ultra-fine-grained nickel processed by severe plastic deformation,” *Materials Science and Engineering A*, vol. 397, no. 1-2, pp. 330–337, 2005.
- [58] L. Farbaniec, *Deformation Mechanisms and Fracture Strength of Polycrystalline Ultrafine-Grained Materials: Experimental and Numerical Investigations [Ph.D. thesis]*, University of Paris 13, Villetaneuse, France, 2012.
- [59] P. Scardi, M. Leoni, E.J. Mittemeijer, and P. Scardi, *Diffraction Analysis of the Microstructure of Materials*, Springer, Berlin, Germany, 2003.

- [60] L. Minier, S. Le Gallet, Y. Grin, and F. Bernard, "Influence of the current flow on the SPS sintering of a Ni powder," *Journal of Alloys and Compounds*, vol. 508, no. 2, pp. 412–418, 2010.
- [61] L. Minier, S. Le Gallet, Yu. Grin, and F. Bernard, "A comparative study of nickel and alumina sintering using Spark Plasma Sintering (SPS)," *Materials Chemistry and Physics*, vol. 134, pp. 243–253, 2012.

Research Article

Formation Behavior of Continuous Graded Composition in Ti-ZrO₂ Functionally Graded Materials Fabricated by Mixed-Powder Pouring Method

Murali Jayachandran, Hideaki Tsukamoto, Hisashi Sato, and Yoshimi Watanabe

Graduate School of Engineering, Nagoya Institute of Technology, Gokiso-cho, Showa-ku, Nagoya 466-8555, Japan

Correspondence should be addressed to Yoshimi Watanabe; yoshimi@nitech.ac.jp

Received 21 February 2013; Accepted 23 April 2013

Academic Editor: Lianjun Wang

Copyright © 2013 Murali Jayachandran et al. This is an open access article distributed under the Creative Commons Attribution License, which permits unrestricted use, distribution, and reproduction in any medium, provided the original work is properly cited.

A mixed-powder pouring method has been proposed to fabricate functionally graded materials (FGMs) with the desired compositional gradient. The experimental procedure involves preparation of mixed powders consisting of more than two types of particles with different size and/or density, which exhibit different velocities in suspension and sedimentation to form the green body under gravity conditions. The green body was sintered by a spark plasma sintering (SPS) method. The initiation of the particle settlement was precisely controlled by using crushed ice as the suspension medium. Ti-ZrO₂ FGMs were fabricated, in this study, using different sizes of ZrO₂ and Ti particles. Vickers hardness confirmed the compositional gradient in the fabricated FGMs. A numerical simulation was also carried out to analyze the particle movement inside the suspension medium during the formation process and predict compositional gradient in the FGMs.

1. Introduction

Functionally graded materials (FGMs) are the advanced composite materials characterized by spatial variations in composition and microstructure that change over the volume [1–5]. Due to this compositional gradient in materials and components, the functional properties of FGMs can be achieved [1–5]. The interface between materials is substantially eliminated; that is, the stress singularity is removed leading to minimizing thermal fatigue failure.

There are several effective techniques recently proposed to fabricate Ti-ZrO₂ FGMs [6–8]. Kinoshita et al. proposed a method developing compositional gradient using a slurry-pouring method [7, 8]. This method allowed particles to settle down under the gravitational force and the FGMs were successfully fabricated with large and continuous compositional gradients. However, it is difficult to control the initiation of particle settlement. In case of a centrifugal slurry-pouring method, the initiation of particle settlement cannot be controlled to completely nullify the effect of gravitational force.

In this study, to overcome this problem, we propose mixed-powder method, in which crushed ice is used as the

particle suspension medium to control the particle sediment from the initiation to the end. In order to clearly understand behavior of particles in the suspension medium, also termed as a “buffer zone,” the simulation was carried out in cases of different buffer zone lengths. We show that the desired gradient pattern from 100% Ti at one surface to 100% ZrO₂ at another can be obtained with the buffer zone of length 250 mm based on the simulation. Ti-ZrO₂ FGMs were experimentally fabricated using this new technique of mixed-powder pouring method. The simulation and experimental results are compared to verify the validity of the model and understand the effectiveness and usefulness of mixed-powder pouring method in the FGM fabrication.

2. Basic Theory and Simulation

The velocity of a spherical solid particle migrating in viscous liquid under the gravitational force can be described based on Stokes' law. In the simulation, the crushed ice was assumed to possess the characteristics of water, and the movement of solid particles is not affected by any other external forces

except for the resistance force by the suspension liquid and the gravitational force. The velocity of Ti and ZrO₂ particles migrating under the gravitational force in liquid can be expressed by the following equations:

$$v_{\text{Ti}} = \frac{(\rho_{\text{Ti}} - \rho_f)}{18\eta} d_{\text{Ti}}^2 g, \quad (1)$$

$$v_{\text{ZrO}_2} = \frac{(\rho_{\text{ZrO}_2} - \rho_f)}{18\eta} d_{\text{ZrO}_2}^2 g,$$

where ρ_{Ti} , ρ_{ZrO_2} , and ρ_f are the densities of Ti and ZrO₂ particles and the density of suspension liquid, d_{Ti} and d_{ZrO_2} are diameter of Ti and ZrO₂ particles, and η and g are viscosity of suspension liquid and acceleration due to gravity, respectively.

Figure 1 shows migration velocities of Ti and ZrO₂ particles under the gravitational force, where the densities of Ti and ZrO₂ particles are 4.5 Mg/m³ and 6.05 Mg/m³, respectively [8]. The velocities of the particles are calculated as a function of sizes and densities using (1).

As seen in Figure 1, it is obvious that the velocity of ZrO₂ particles is higher than that of Ti particles, when the particle size is the same, due to larger density of ZrO₂ particles. On the other hand, if the mixed powder contains the ZrO₂ particles of smaller size and Ti particles of larger size, then Ti particles can have higher velocity than that of ZrO₂ particles in some specific conditions [8, 9].

The velocity of the particles is also greatly influenced by the resistance by the suspension liquid. Using Brinkman's viscosity equation [10], the resistance force by the viscous liquid to the migrating particles is calculated in the simulation. The viscosity of suspension liquid containing solid particles with spherical shape can be written as follows:

$$\eta = \frac{\eta_0}{(1 - V/V_{\text{max}})^{5/2}}, \quad (2)$$

where η , η_0 , V , and V_{max} are the apparent viscosity of the liquid containing solid particles, the viscosity of the suspension liquid without particles, the volume fraction of solid particles and the maximum containable volume fraction of solid particles, respectively. The V_{max} depends on the packing fraction of solid particles in liquid. The maximum volume fraction of spherical solid particles is between 52% for simple cubic packing and 74% for close packing.

In this study, the formation behavior of graded composition in Ti-ZrO₂ FGMs using mixed-powder pouring method under gravity is simulated. The length of the suspension medium, that is, the buffer zone, of 250 mm, is used in the simulation. The buffer zone is divided into subzones with the equal length as shown in Figure 2. The particle movement velocity along the gravitational force direction is calculated in each zone. Correspondingly, the volume fraction of the two kinds of powders at any arbitrary zone, n , is also simulated. The volume fraction of particles, V'_n , at zone n is calculated using the formula following:

$$V'_n = V_n - \frac{v_n}{a} V_n + \frac{v_{n-1}}{a} V_{n-1} D_{n-1}, \quad (3)$$

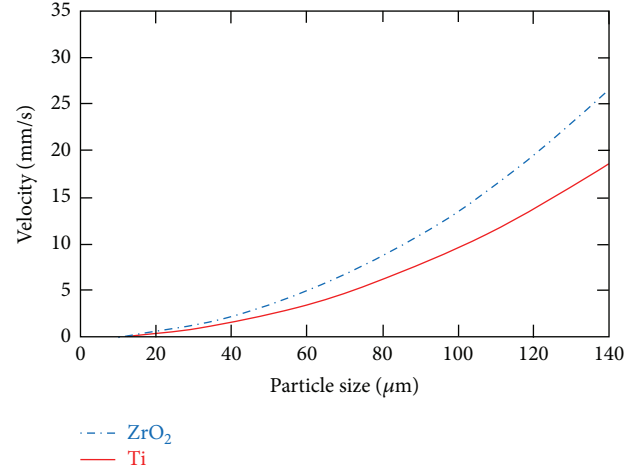


FIGURE 1: Variation in particle velocity for different size and density.

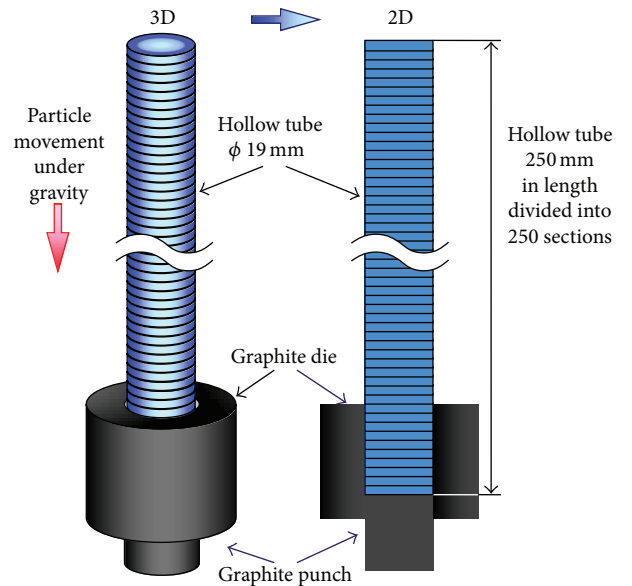


FIGURE 2: Classification of buffer length in zones.

where V_n , v_n , a , and D_n are the prior volume fraction of particle, movement velocity of a particle, width of each zone, and the ratio of volume fraction of zones n and $n + 1$, respectively.

Figure 3 shows the flowchart for calculation of the velocity of particles inside the suspension zone and the volume fraction of the particles in each zone. The input parameters required for calculation are as follows: the densities of the particles used in the mixed-powder pouring method, the density and viscosity of water (suspension medium) of 0.998 Mg/m³ and 0.89 mPa·s, respectively, particle size range, and the number of zones or sections in the suspension medium. The maximum packing factor is set at 0.52 in the calculation process.

The initial volumes of two particles are calculated. In case of Ti particles of a size range of 90–150 μm, the initial volumes

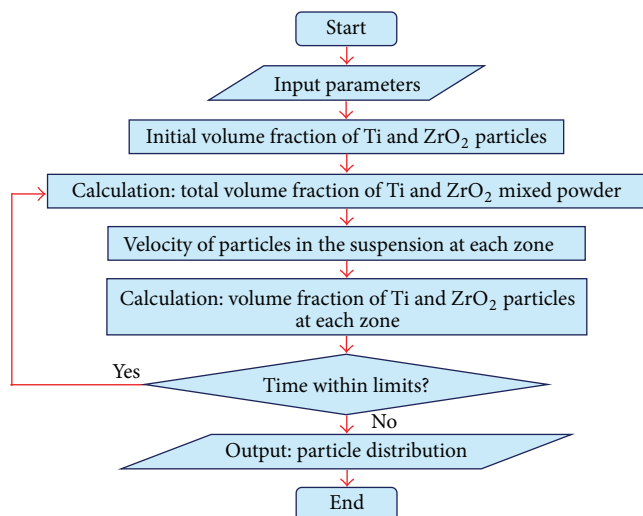


FIGURE 3: Calculation process of particle distribution in FGMs.

of 90 μm and 150 μm sized Ti powder are taken as 25% each, and the rest 50% of initial volume is assumed to be the average of 90 μm and 150 μm , that is, 120 μm . The velocity of particles at each zone is calculated based on Stoke's law. From the velocity of the particles, the volume fraction of particles is calculated using (3). This process is repeated in the specified limited time and the final particle distribution is obtained.

3. Materials and Methods

For the mixed-powder pouring process, homogeneously mixed powders of Ti and ZrO_2 with a volume ratio 1:1 were prepared. Ti particles have an angular shape, and ZrO_2 particles have a spherical shape. The details of prepared homogeneous mixture with different particle sizes are described in Table 1. In all the samples shown in Table 1, the average size of ZrO_2 particles is larger than that of Ti particles.

3.1. Preparation of SPS Specimen. A graphite die with an inner diameter of 20 mm and a height of 40 mm was used. carbon sheet was placed along the inner wall of the graphite die as shown in Figure 4. A bottom punch was fitted tightly to one end of the graphite die as shown in Figure 4. A hollow tube with a length of 220 mm made of plastic was fitted and sealed to another end of the graphite die. The height of the total suspension, that is, the length of the hollow tube along with the graphite die is 250 mm. The crushed ice with a volume of $78.5 \times 10^{-6} \text{ m}^3$ was prepared using the ice crusher.

The hollow tube was filled with the crushed ice as shown in Figure 4(a). Then, prepared homogeneously mixed powders were poured from the top of the crushed ice, as shown in Figure 4(b). The crushed ice was allowed to melt gradually under isothermal conditions at 40°C. Sedimentation of Ti and ZrO_2 particles proceeded along the hollow tube at the uniform temperature. The homogeneously-mixed powders poured on the top of crushed ice will move down along the hollow tube and settle down at the bottom of the graphite die. Sedimentation of the mixed powders depend on the densities

and/or sizes of the particles. After settlement, a green body was obtained, as shown in Figure 4(c), which was sintered using SPS afterwards.

3.2. Fabrication of FGMs. The SPS was carried out under the pressure of 30 MPa at the sintering temperature of 1200°C. After sintering, disc-shaped Ti-ZrO₂ sample of FGMs with 20 mm in diameter and 10 mm in height was obtained. To carry out microstructural investigation, the specimen was cut into a cuboid shape with dimensions of $10 \times 8 \times 5 \text{ mm}^3$ using a microcutter. Scanning electron microscope (SEM) and energy dispersive X-ray spectroscopy (EDX) were used to observe the microstructure and evaluate the composition distribution of the fabricated FGMs, respectively. Further, Vickers hardness test was conducted on the FGM samples to study the mechanical property and confirm the gradient in the composition of the fabricated FGMs.

4. Results and Discussion

4.1. Compositional Gradients Obtained by Simulation. Figures 5(a), 5(b), and 5(c) show the calculated volume fraction distributions of Ti and ZrO_2 in samples A, B, and C, respectively. The abscissa in Figure 5 is the position in the direction of gravity normalized by the length of composite; that is, 0 and 1 represent the top and bottom surfaces of the FGMs, respectively. It can be seen from Figure 5 that Ti and ZrO_2 distributions across the normalized position have yielded large compositional gradient within the FGMs. According to the simulation, with increase in normalized position 0 to 1, the volume fraction of Ti decreases and ZrO_2 increases, which results in a largely graded microstructure. It can be also seen in the figures that the particle distribution becomes homogeneous between normalized positions 0.6 and 0.65.

4.2. Microstructure and Compositional Gradient of Ti-ZrO₂ FGMs. Photographs of Ti-ZrO₂ FGMs samples #A, #B, and #C are shown in Figures 6(a), 6(b), and 6(c), respectively. As shown in these figures, continuous compositional gradients may form within these samples.

Figures 7(a), 7(b), and 7(c) are the SEM images the FGMs samples #A, #B, and #C, respectively. The four SEM images in each column show the graded structure of Ti and ZrO_2 across the normalized position, that is, from top to bottom of the fabricated FGMs. From the four figures, it can be seen that the concentration of spherical particles increases gradually from top to bottom.

The concentrations of Ti and ZrO_2 at each region were analyzed by EDX, and the volume fraction distributions of Ti and ZrO_2 in Ti-ZrO₂ FGMs were obtained as shown in Figures 8(a), 8(b), and 8(c). It can be seen from these figures that the volume fraction of Ti is close to 100% between the normalized positions of 0 and 0.2 in all the samples. The composition of Ti decreases and that of ZrO_2 increases continuously and gradually, to become nearly homogeneous between normalized positions of 0.6 and 0.65. The volume fraction of ZrO_2 reaches close to 100% between the normalized positions 0.8 and 1, as shown in Figures 8(a) and 8(b). Therefore, it is found that the mixed-powder pouring

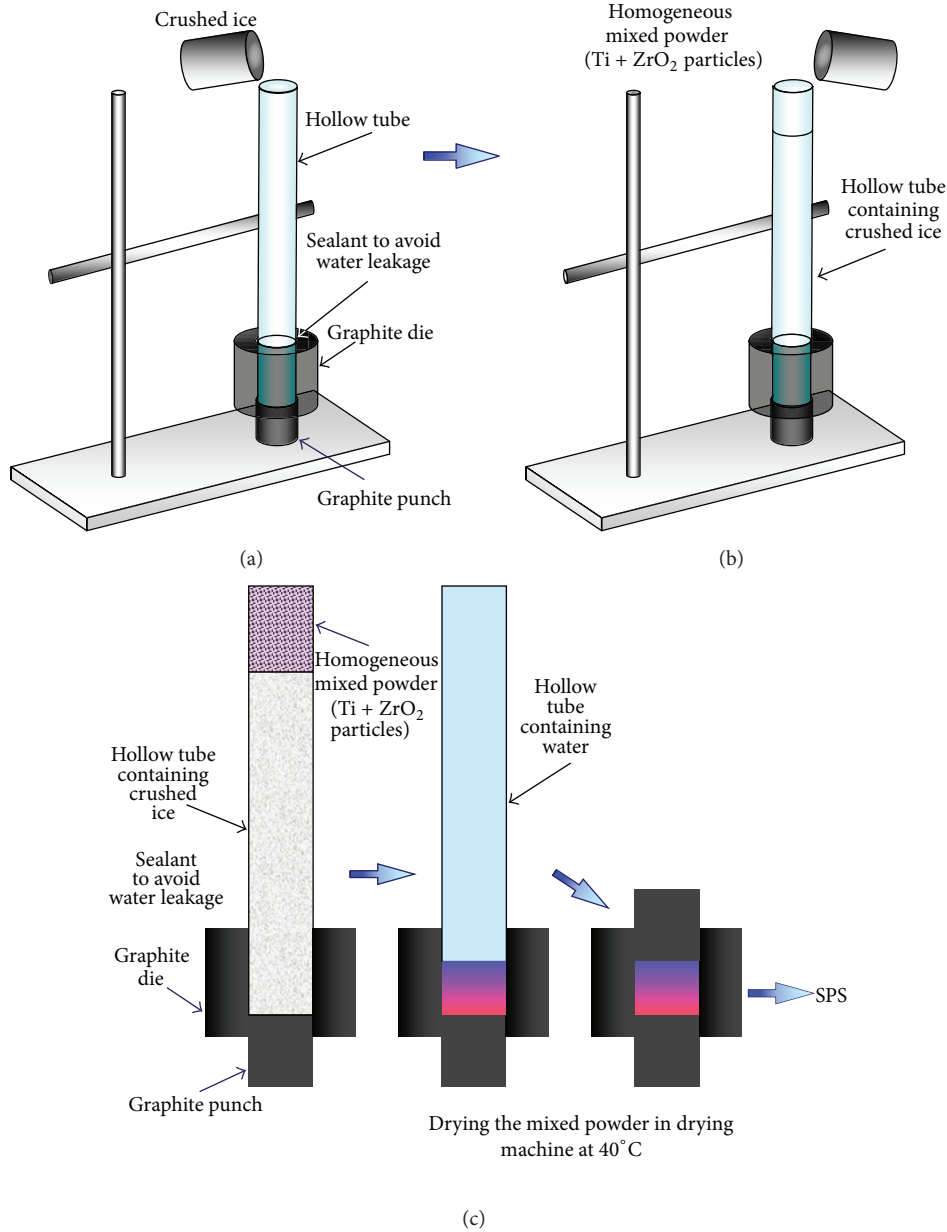


FIGURE 4: Experimental setup: (a) pouring crushed ice into hollow tube, (b) pouring homogeneous Ti-ZrO₂ mixed powder into hollow tube containing crushed ice, and (c) process involved in preparation of green body.

TABLE 1: Samples prepared in this study.

Particle	Density	Mass	Sample A	Sample B	Sample C
ZrO ₂	6050 kg/m ³	9.51 g	75–106 μm	38–75 μm	106–150 μm
Ti	4500 kg/m ³	7.07 g	63–90 μm	45 μm pass	90–150 μm

method is an effective fabrication technique for FGMs with large and continuous compositional gradient. However, from the results shown in Figure 8(c), it can be observed that the volume fraction of ZrO₂ fails to reach 100% near the normalized position 1 where the large compositional gradient is not observed because of small migration speed difference between Ti and ZrO₂ particles. The larger buffer zone is neces-

sary, for obtaining the larger compositional gradient in sample #C.

Figure 9 shows the X-ray diffraction (XRD) pattern from the ZrO₂ surface in sample A. At the ZrO₂ surface, peaks for ZrO₂ (tetragonal) and no peak for Ti can be seen, which means that 100% ZrO₂ layer formed at one side. It is considered that FGMs with 100% ZrO₂ at one side and 100%

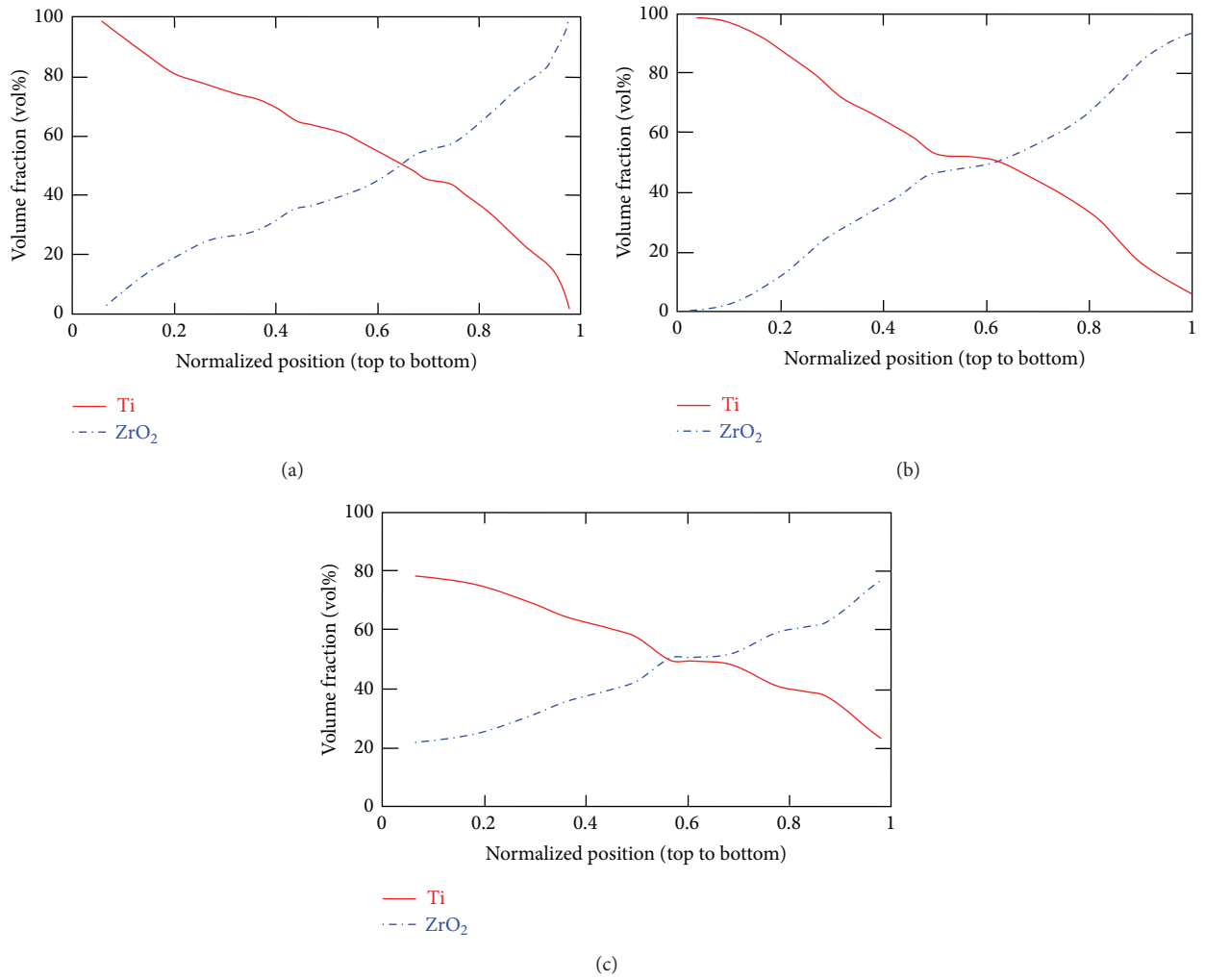


FIGURE 5: Calculated volume fractions of Ti and ZrO₂ in Ti-ZrO₂ FGMs, (a) sample A, (b) sample B, and (c) sample C.

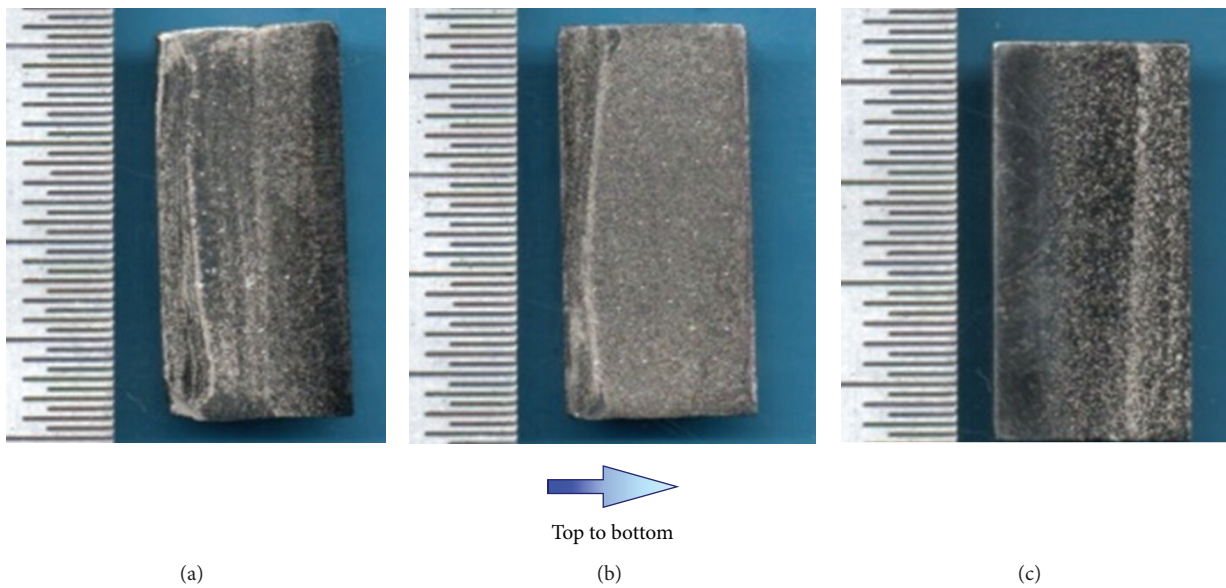


FIGURE 6: Photographs of Ti-ZrO₂ FGMs samples, (a) sample A (b) sample B, and (c) sample C.

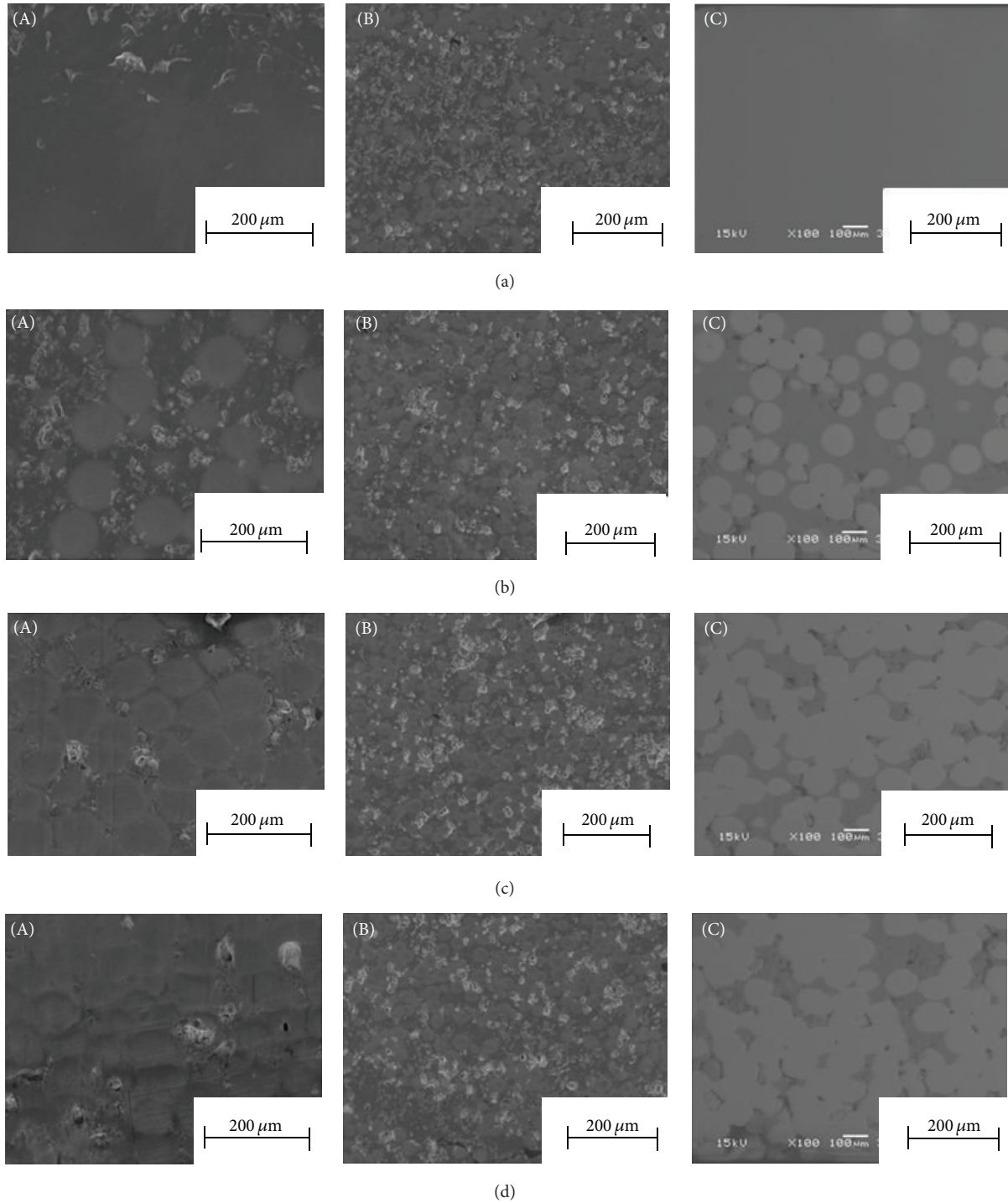


FIGURE 7: SEM photographs of microstructure of Ti-ZrO₂ FGMs for (A) sample A, (B) sample B, and (C) sample C. Photographs of (X-a), (X-b), (X-c) and (X-d) are taken at normalized position of 0.0 to 0.25, 0.25 to 0.5, 0.5 to 0.75, and 0.75 to 1.0, respectively.

Ti at another side can be obtained with a suitable selection of powder sizes and buffer zone length.

4.3. Hardness. The hardness values in Ti-ZrO₂ FGMs samples #A, #B, and #C are also shown in Figures 8(a), 8(b), and 8(c), respectively. The Vickers hardness (Hv) of Ti and

ZrO₂ ranges between 200–300 and 1200–1300, respectively. It was concluded in [11] that SPS has the potential of enhanced densification and suppressed grain growth due to a fast heating rate and apparent low firing temperature. Therefore, the actual hardness measured in the fabricated FGMs is on the slightly higher side. The hardness inside the fabricated

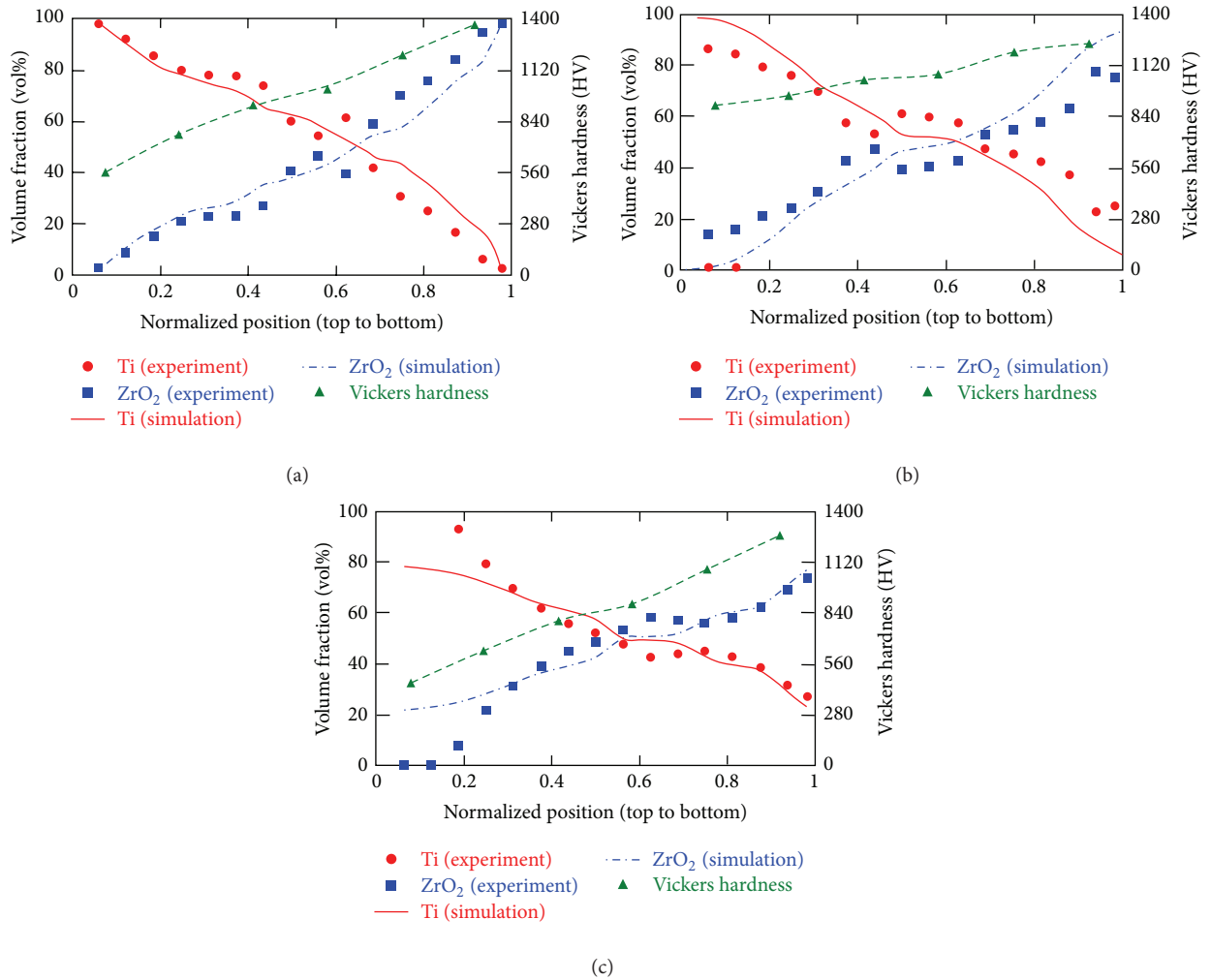


FIGURE 8: Comparison of experimental volume fraction results with simulation results and effects of hardness number in Ti-ZrO₂ FGMs (a) sample A (b) sample B, and (c) sample #C.

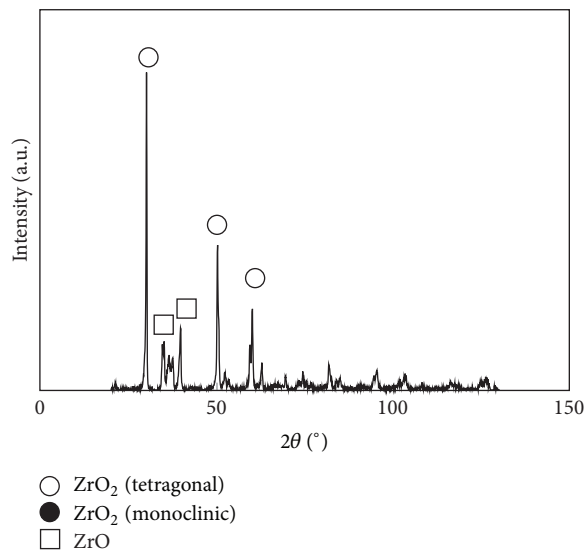


FIGURE 9: XRD pattern from the ZrO₂ surface in sample A.

FGMs increases with the increase in normalized position 0 to 1, thereby, confirming the increasing ZrO_2 content across the normalized position.

5. Conclusions

In this study, FGMs were fabricated using a mixed-powder pouring method followed by SPS. The desired continuous compositional gradient with 100% Ti at one side and 100% ZrO_2 at another side in the Ti- ZrO_2 FGMs was obtained. Numerical simulation considerably represented experimental results, which can be used to select suitable sizes of powders and experimental conditions to obtain predesigned compositional gradients in the FGMs.

Acknowledgments

This work is supported by Regional Innovation Cluster Program (Gifu Technical Innovation Program, Japan) of the Ministry of Education, Culture, Sports, Science and Technology of Japan. H. Sato and Y. Watanabe gratefully acknowledge the financial support from The Light Metal Educational Foundation Inc. of Japan. The authors are also grateful to Ms. Motoko Yamada for her helpful work in carrying out the experiments.

References

- [1] T. Hirai, "Materials science and technology," in *Processing of Ceramics*, R. J. Brook, Ed., vol. 17, p. 293, VCH Weinheim, FRG.
- [2] S. Suresh and A. Mortensen, *Fundamentals of Functionally Graded Materials, Processing and Thermomechanical Behaviour of Graded Metals and Metal-Ceramic Composites*, IOM Communications, London, UK, 1998.
- [3] Y. Miyamoto, W. A. Kaysser, B. H. Rabin, A. Kawasaki, and R. G. Ford, Eds., *Functionally Graded Materials, Design, Processing and Applications*, Kluwer Academic, New York, NY, USA, 1999.
- [4] S. Uemura, Y. Noda, Y. Shinohara, and Y. Watanabe, Eds., *Development and Application of Functionally Graded Materials*, CMC Publishing, Tokyo, Japan, 2003.
- [5] Y. Watanabe, N. Yamanaka, and Y. Fukui, "Control of composition gradient in a metal-ceramic functionally graded material manufactured by the centrifugal method," *Composites A*, vol. 29, no. 5-6, pp. 595-601, 1998.
- [6] S. Li, H. Izui, M. Okano, W. Zhang, and T. Watanabe, "Mechanical properties of ZrO_2 (Y_2O_3)- Al_2O_3 nanocomposites with addition of hydroxyapatite prepared by spark plasma sintering," *Materials Science Forum*, vol. 631-632, pp. 413-423, 2010.
- [7] K. Kinoshita, H. Sato, and Y. Watanabe, "Development of compositional gradient simulation for centrifugal slurry-pouring methods," *Materials Science Forum*, vol. 631-632, pp. 455-460, 2010.
- [8] Y. Watanabe, E. Miura-Fujiwara, and H. Sato, "Fabrication of functionally graded materials by centrifugal slurry-pouring method and centrifugal mixed-powder method," *Journal of the Japan Society of Powder and Powder Metallurgy*, vol. 57, no. 5, pp. 321-326, 2010.
- [9] Y. Watanabe and H. Sato, "Review fabrication of functionally graded materials under a centrifugal force," in *Nanocomposites with Unique Properties and Applications in Medicine and Industry*, J. Cuppolitti, Ed., p. 142, InTech, Rijeka, Croatia, 2011.
- [10] H. C. Brinkmann, "The viscosity of concentrated suspensions and solutions," *The Journal of Chemical Physics*, vol. 20, no. 4, p. 571, 1952.
- [11] T. Takeuchi, "Preparation of electric-functional ceramics by spark-plasma-sintering method," *Journal of High Temperature Society*, vol. 31, no. 4, p. 186, 2005.

Research Article

Spark Plasma Sintering and Densification Mechanisms of Antimony-Doped Tin Oxide Nanoceramics

Junyan Wu,¹ Fei Chen,¹ Qiang Shen,¹ Julie M. Schoenung,² and Lianmeng Zhang¹

¹ State Key Lab of Advanced Technology for Materials Synthesis and Processing, Wuhan University of Technology, Wuhan 430070, China

² Department of Chemical Engineering and Materials Science, University of California Davis, CA 95616, USA

Correspondence should be addressed to Lianmeng Zhang; lmzhang@whut.edu.cn

Received 22 February 2013; Revised 18 April 2013; Accepted 23 April 2013

Academic Editor: Bikramjit Basu

Copyright © 2013 Junyan Wu et al. This is an open access article distributed under the Creative Commons Attribution License, which permits unrestricted use, distribution, and reproduction in any medium, provided the original work is properly cited.

Densification of antimony-doped tin oxide (ATO) ceramics without sintering aids is very difficult, due to the volatilization of SnO₂, formation of deleterious phases above 1000°C, and poor sintering ability of ATO particles. In this paper, monodispersed ATO nanoparticles were synthesized via sol-gel method, and then ATO nanoceramics with high density were prepared by spark plasma sintering (SPS) technology using the as-synthesized ATO nanoparticles without the addition of sintering aids. The effect of Sb doping content on the densification was investigated, and the densification mechanisms were explored. The results suggest that ATO nanoparticles derived from sol-gel method show good crystallinity with a crystal size of 5–20 nm and Sb is incorporated into the SnO₂ crystal structure. When the SPS sintering temperature is 1000°C and the Sb doping content is 5 at.%, the density of ATO nanoceramics reaches a maximum value of 99.2%. Densification mechanisms are explored in detail.

1. Introduction

Because of their high electrical conductivity combined with chemical stability and corrosion resistance, antimony-doped tin oxide (ATO) materials are widely used in numerous applications such as catalytic and gas-sensing applications to monitor toxic gas emissions, as electrodes in the glass industry and as transparent conductive oxide (TCO) films [1–4]. Recently, ATO ceramics with high density (>95%) and high electrical conductivity have become target candidates for depositing TCO films in substitution of the more conventional indium tin oxide (ITO) films [5].

However, the densification of ATO ceramic is very difficult because surface diffusion and evaporation-condensation limit densification [6, 7]. Long heating times required for conventional sintering (pressureless sintering and hot pressing) usually cause evaporation of SnO₂ and lead to particle coarsening and low density. The sintering problem is further complicated by the high vapor pressure of SnO, the formation of deleterious intermediate phases, and decomposition of

the ATO system at temperatures above 1000°C [8]. Adding additives such as ZnO, CuO, and MnO₂ can promote densification by a liquid-phase mechanism [9–11], but the secondary phases formed in these cases adversely affect the electrical conductivity.

Spark plasma sintering (SPS) has the potential to obtain fully dense materials at low temperature and with a rapid sintering rate, which can prevent the formation of deleterious intermediate phases and reduce the evaporation of SnO₂. Furthermore the spark discharge could activate the particles to improve densification [12, 13]. Many researchers have reported the enhanced densification of SnO₂-based ceramics prepared by SPS [14, 15]. Scarlat et al. [14] prepared ATO ceramics using the field-assisted sintering technique (FAST) with ATO powders obtained by solid phase synthesis. The relative density (92.4%) was enhanced compared with the density of ATO ceramics sintered by conventional sintering technique (61.3%), but it is still too low for a target used to prepare TCO films using magnetron sputtering method. Zhang et al. [15] used the SPS technique to fabricate ATO

ceramics with high density of 97.4% using monodispersed ATO nanoparticles synthesized by the hydrothermal method. Compared to Scarlat et al.'s results, the high density of ATO ceramics obtained by Zhang et al. can be contributed to the higher activation energy of ATO nanoparticles. However, Zhang has only reported the sintering behavior of ATO ceramic with 5 at.% doping content of Sb. The sintering mechanism as well as the relationship between Sb doping content and densification behavior is not clear. Besides, as a conductive material, the effect of electrical conductivity on the sintering behavior and densification of ATO ceramic should not be ignored during the large electrical current sintering of SPS.

In this paper, monodispersed ATO nanoparticles were synthesized by the sol-gel method. Then, SPS with low temperature sintering and rapid sintering rate was used to obtain ATO ceramics with high density, without the incorporation of sintering aids. Finally, the densification mechanisms associated with SPS consolidation of bulk ATO ceramics were investigated.

2. Experimental

The ATO nanoparticles were prepared using sol-gel method. A precursor solution was synthesized using tin (IV) tetrachloride (SnCl_4 , >98%), antimony chloride (SbCl_3), anhydrous ethanol ($\text{C}_2\text{H}_5\text{OH}$, >99.7%), and citric acid (CA) in a three-necked flask. The solution was refluxed at 70°C for 5 h with a vigorous stirring and then aged at 30°C for 48 h to get a gel. Finally, the gel was dried at 80°C in a vacuum oven for 24 h and then calcined in furnace at 500°C for 3 h.

The SPS system (SPS-1050, Sumitomo Coal Mining Co, Yokohama, Japan) was used in the present investigation. The ATO nanoparticles were loaded in a 20 mm inner diameter graphite die, and then the die was transferred into the SPS machine. The pulse pattern was kept constant and consisted of twelve pulses (with a pulse duration of 3.3 ms), followed by two periods of zero current. The applied axial pressure was 40 MPa from the beginning of the heating step to the duration time, then it was unloaded to 0 MPa during the cooling step. All samples were sintered at 1000°C (which is below the formation temperature of some deleterious intermediate phases during sintering) with a heating rate of $100^\circ\text{C}/\text{min}$ and dwell durations up to 3 min in vacuum (~ 20 Pa).

The density of the sintered ATO ceramics was tested by the Archimedes method in water. The phase structures of the ATO nanoparticles and sintered ceramics were investigated by X-ray diffraction (XRD, Rigaku Ultima III) with $\text{CuK}\alpha$ radiation. The sample was scanned from 20° to 80° (2θ) in steps of 0.05° . The crystallite size is calculated by the full width at half maximum (FWHM). The microstructures of the ATO nanoparticles and sintered ceramics were observed in a field emission scanning electron microscope (FE-SEM, Hitachi S-4800) and a transmission electron microscope (TEM, JEM-2100F STEM/EDS). The oxidation states of Sb were determined by X-ray photoelectron spectroscopy (XPS, VG Multilab 2000). During XPS analysis, a Mg/Al double anode X-ray was used as the excitation source.

3. Results and Discussion

3.1. Phase Composition and Microstructure of ATO Nanoparticles. Figure 1 shows the XRD patterns for ATO nanoparticles with different Sb doping concentrations and pure SnO_2 nanoparticles. It can be seen that, with antimony content varying from 0 to 10 at.%, ATO nanoparticles show the presence of only one crystalline phase structurally related to cassiterite, which indicates that the SnO_2 lattice can accommodate 10 at.% Sb atoms without significant changes in the structure [16]. With increasing Sb content, the peaks show little shift to the lower 2θ values, which indicates that Sb is incorporated into the SnO_2 crystal structure. The crystallite size determined from the SnO_2 (110) plane by FWHM is approximately 4.6 nm, 5.8 nm, 9.1 nm, and 16.8 nm for ATO nanoparticles with 1 at.%, 3 at.%, 5 at.%, and 10 at.% Sb, respectively.

Figure 2 illustrates the TEM morphology of ATO nanoparticles with 5 at.% Sb and 10 at.% Sb. It is clear that the as-synthesized ATO nanoparticles show good crystallinity. The crystallite size of ATO nanoparticles with 5 at.% Sb is ~ 10 nm, while the crystallite size of ATO nanoparticles with 10 at.% Sb is ~ 20 nm, which is in agreement with crystallite size estimated by FWHM. This similarity indicates that the ATO nanoparticles synthesized by the sol-gel method are monodispersed. The small difference in crystallite size with different Sb doping concentration may contribute to the segregation of Sb to the surface of ATO particles, which ultimately affect the grain growth of particles [17]. The monodispersed ATO nanoparticles indicate high activation energy and good sintering potential, which may enhance the densification of ATO ceramics.

3.2. Densification and Sintering Behavior of ATO Nanoceramics. The SPS process used to consolidate the ATO nanoceramics (without the use of sintering aids) was carried out at 1000°C for a holding period of 3 min in vacuum at a heating rate of $100^\circ\text{C}/\text{min}$. Figure 3 shows the sintering behavior of pure SnO_2 nanoparticles and as-synthesized ATO nanoparticles. Figure 3(a) illustrates displacement, displacement rate, and temperature curves as a function of the sintering time, while Figure 3(b) illustrates the densification curves converted from displacement by considering the relative densities of sintered samples [18, 19]. The slight shrinkage for ATO nanoparticles at the initial sintering stage can be seen clearly from Figure 3(a), while no shrinkage for SnO_2 nanoparticles can be observed at the same stage. The slight shrinkage indicates the activation of ATO nanoparticles due to spark discharge, and this phenomenon will be further illustrated in Section 3.4. Furthermore, ATO nanoparticles show higher displacement rate than pure SnO_2 nanoparticles at about 700°C , which indicates enhanced sintering potential of ATO nanoparticles, especially ATO nanoparticles with 5 at.% Sb. On the other hand, it can be seen obviously in Figure 3(b) that the ATO nanoparticles containing 5 at.% Sb show a higher density than the other two samples at the same sintering temperature.

The lattice parameters and density data of the sintered ATO nanoceramics are provided in Table 1. For comparison,

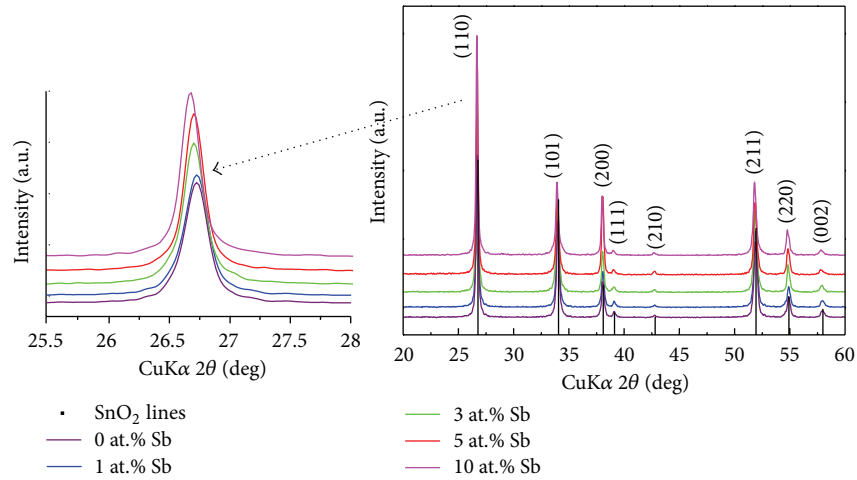


FIGURE 1: XRD patterns for ATO nanoparticles with different Sb doping concentrations.

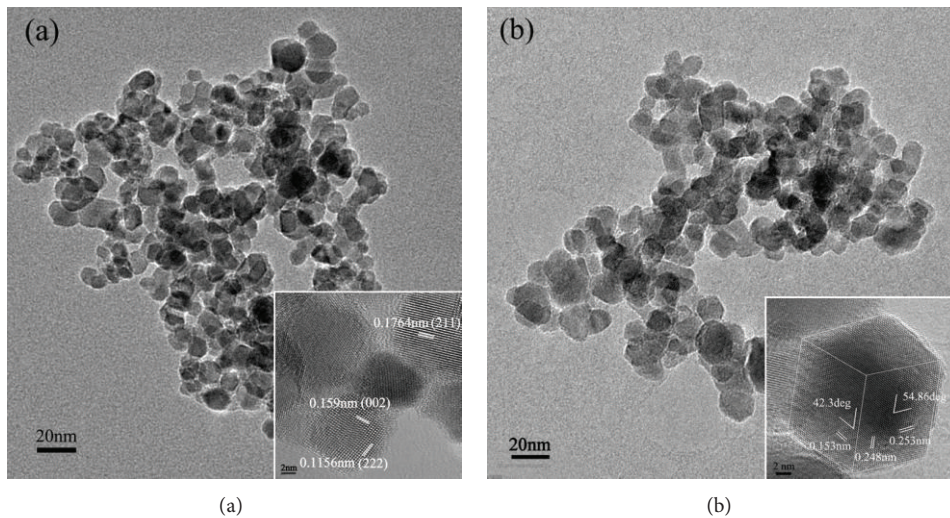


FIGURE 2: TEM morphology of ATO nanoparticles with (a) 5 at.% Sb, (b) 10 at.% Sb.

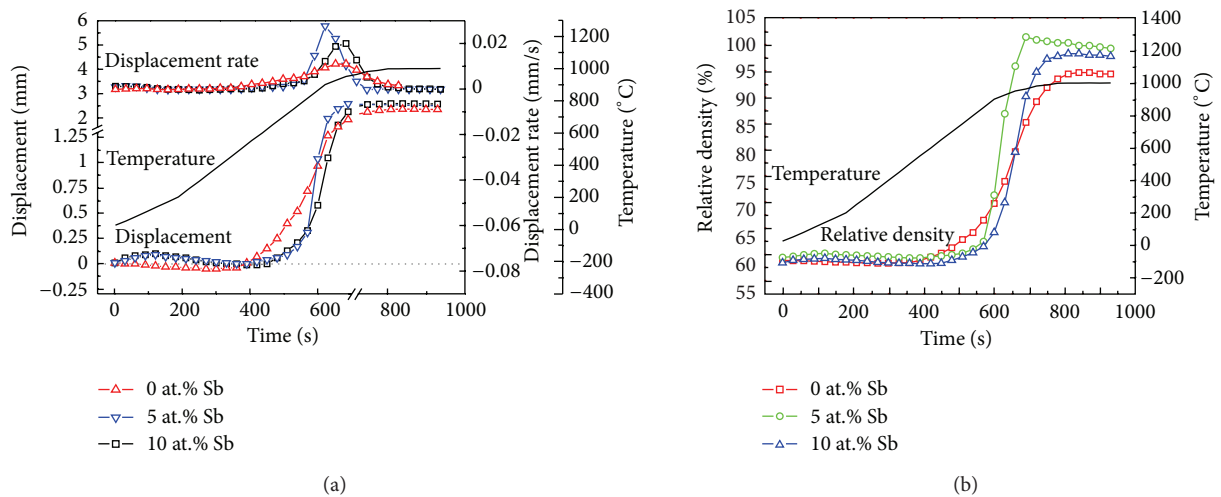


FIGURE 3: Sintering behavior of pure SnO₂ nanoparticles and as-synthesized ATO nanoparticles: (a) displacement, displacement rate, and temperature curves as a function of sintering time, (b) relative density and temperature curves as function of sintering time.

TABLE 1: Lattice parameters and density data of the sintered ATO nanoceramics.

Sample	$a = b$ (Å)	c (Å)	V (Å ³)	d_{theor} (g/cm ³)	d_{exp} (g/cm ³)	d_{rel} (%)
Pure SnO ₂ [†]	4.7382	3.1871	71.552	6.993	6.599	94.4
1 at. % Sb	4.7405	3.1898	71.682	6.987	6.71	96.1
3 at. % Sb	4.7468	3.1905	71.89	6.95	6.73	96.8
5 at. % Sb	4.7486	3.1955	72.057	6.944	6.889	99.2
10 at. % Sb	4.749	3.221	72.622	6.89	6.732	97.7

V is the volume of the ATO crystal lattice, d_{theor} is the theoretic density calculated by the lattice parameters, d_{exp} is the experimental density tested by the Archimedes method, and d_{rel} is the relative density calculated as $d_{\text{exp}}/d_{\text{theor}}$.

[†] Pure SnO₂: JCPDS Card number 41-1445.

equivalent data for pure SnO₂ are also included. It is clear that both a and c lattice parameters increase with increasing Sb doping concentration. These slight lattice distortions of the cassiterite SnO₂ indicate that Sb is incorporated into the tin oxide lattice to form the ATO solid solution. Furthermore, the as-sintered ATO nanoceramics exhibit high density (96–99% d_{theor}) under the selected SPS conditions, while the density of pure SnO₂ ceramic is only 94.4%. With the increase in Sb doping concentration from 0 at.% to 10 at.%, the density first increases then decreases. When Sb doping concentration is 5 at.%, the density reaches the maximum value of 99.2% which is in agreement with the SPS sintering behavior shown in Figure 3.

3.3. Phase Composition and Microstructure of ATO Nanoceramics. Figure 4 shows the XRD patterns of sintered ATO nanoceramics with different Sb doping concentrations. The XRD spectra show that all peaks are characterized as the cassiterite SnO₂ (JCPDS Card number 41-1445), which indicates that the sintered nanoceramics maintain the character of the ATO nanoparticles and no apparent phase change occurs. The pure and consistent phase of cassiterite SnO₂ before and after sintering implies that the low temperature sintering of SPS successfully prevents the formation of deleterious intermediate phases and the decomposition of the ATO system. The slight shift in peak position with different Sb doping concentration is in agreement with the increases in lattice parameters. The XRD data shows some differences before and after sintering, which may attribute to the transformation of Sb³⁺ to Sb⁵⁺ during sintering [20].

Representative SEM micrographs of the sintered ATO nanoceramics with different Sb doping concentrations are provided in Figure 5. It is observed that the as-sintered ATO nanoceramics are nearly fully dense with no obvious porosity. The grain sizes of the sintered ATO nanoceramics are less than 100 nm, and the grain size increases with increasing Sb doping concentration. When the Sb doping concentration varies from 1 at.% to 10 at.%, the grain size increases from 20 nm to 100 nm. The variable grain sizes may be due to the segregation of Sb to the surface of the ATO nanoparticles. With increasing Sb doping concentration, Sb segregation is known to occur as trivalent Sb (III) at the surface of ATO particles [21]. Trivalent Sb (III), as a cationic dopant with oxidation states lower than Sn⁴⁺, will act as a sintering additive to promote densification and grain growth [22].

Therefore, considering the Sb segregation, the grain size and density of the sintered ATO nanoceramic will increase with increasing Sb doping concentration. However, it can be seen from Figure 3 and Table 1 that the ATO nanoceramic with 5 at.% Sb shows a higher displacement rate and higher density than the ATO nanoceramic with 10 at.% Sb. Thus, the densification mechanisms for SPS-consolidated ATO nanoceramic cannot simply be attributed to the mechanism of adding Sb as a sintering additive.

3.4. Densification Mechanisms in ATO Nanoceramics. From the SPS point of view, the passage of electrical current depends on the electrical conductivity of the powder compact. In case of an insulating powder, the major part of the current passes through the graphite die, with a small fraction passing through particles. While for a conducting powder, the current will pass through the powder [23]. SnO₂ is an n-type semiconductor with low electrical conductivity, and the conductivity will be improved by the addition of dopants such as Sb ions [24, 25]. Thus, a comparatively larger fraction of the total current will pass through the ATO powder compact compared with the SnO₂ powder compact. The electrical resistivity values of SnO₂ (with no Sb) and ATO will also be shown in Figure 7. Therefore, spark discharges in the void spaces become more frequent in the ATO powder compact. The slight shrinkage and higher displacement rate of ATO nanoparticles shown in Figure 1 indicate the passage of current through the sample and the frequent spark discharge in void spaces, as further investigated in the following.

In an effort to investigate the densification mechanisms further, an ATO nanoceramic sample containing 5 at.% Sb was removed from the SPS unit after reaching only 700°C. This sample was evaluated using SEM and EDS, as shown in Figure 6. As shown in Figure 6(a), the spark discharges generate special grains (see region A) in the gaps between the particles. No such grains were observed in the starting nanoparticles. The EDS results in Figure 6(b) suggest that the molar ratios of Sb/Sn/O for the different regions of the microstructure are different. The molar ratios for the region far from the gaps (see region C) are 1/19/40, which is quite in agreement with the molar ratios for the raw particles. On the other hand, the Sn and O contents in the region on the gaps' edge (see region B) are much smaller than that in the starting nanoparticles, with a molar ratio of 1/15/20.

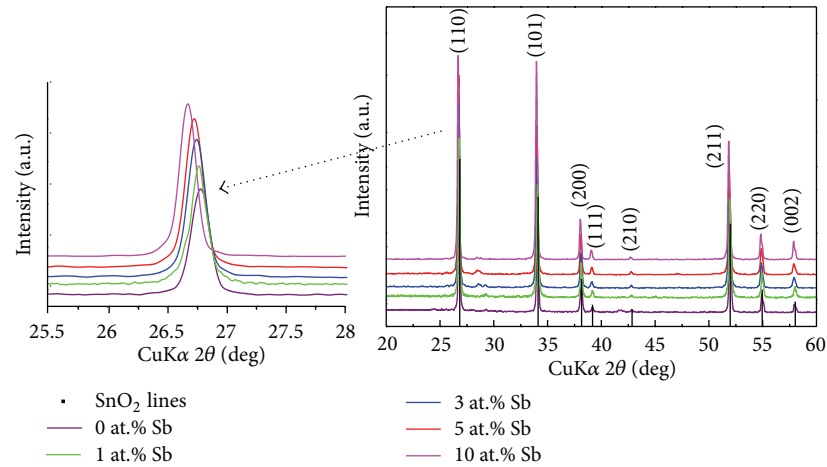


FIGURE 4: XRD patterns for sintered ATO nanoceramics with different Sb doping concentrations.

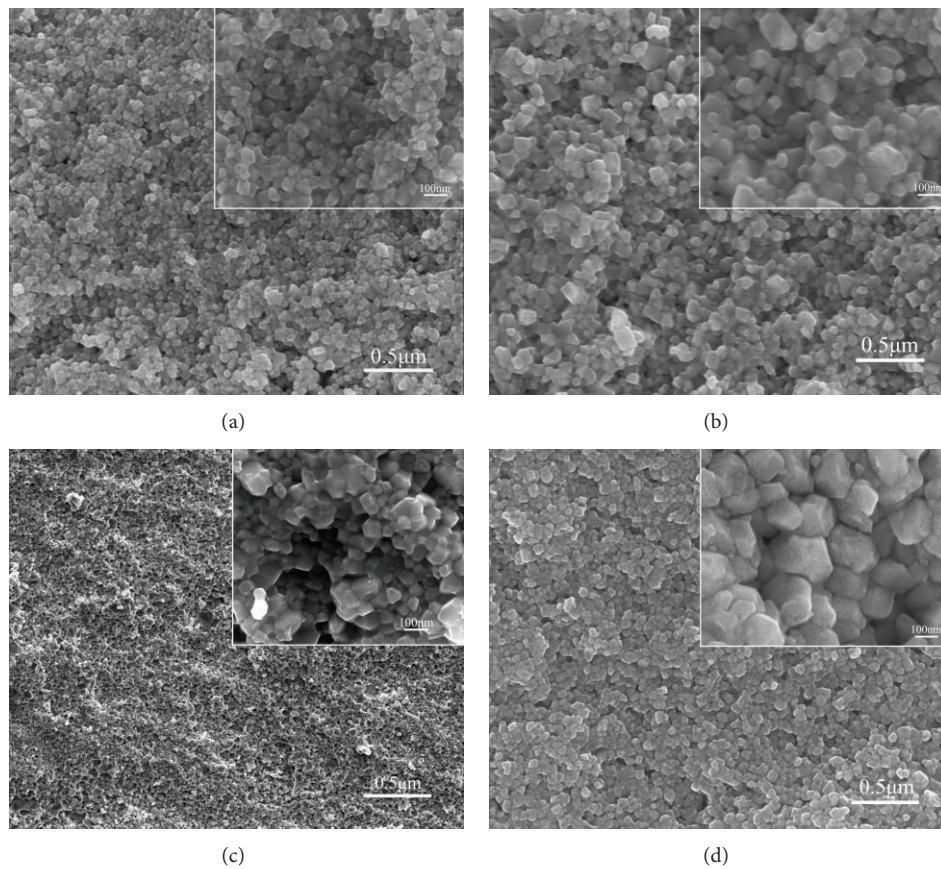


FIGURE 5: SEM micrographs of sintered ATO nanoceramics with different Sb doping concentrations: (a) 1 at.% Sb, (b) 3 at.% Sb, (c) 5 at.% Sb, and (d) 10 at.% Sb.

Many researchers have reported the effect of spark discharge during SPS sintering [26–28]. Particularly, Wu et al. have claimed that the discharge and high local temperature near the pores accelerate the reaction between raw materials [27]. On the other hand, Park et al. [7] have reported the possibility of SnO_2 to evaporative decompensate into $\text{SnO}(\text{g})$ and $\text{O}_2(\text{g})$ during spark plasma sintering. Thus, the

different molar ratios suggest that, on the edge of the gaps, SnO_2 decomposes into $\text{SnO}(\text{g})$ and $\text{O}_2(\text{g})$ then condenses as SnO_x in the gaps by the spark discharge. Therefore, SPS discharges in the void spaces enhance the mass transport, which ultimately enhances densification.

Figure 7 shows the electrical resistivity of the sintered ATO nanoceramics with different Sb doping concentrations.

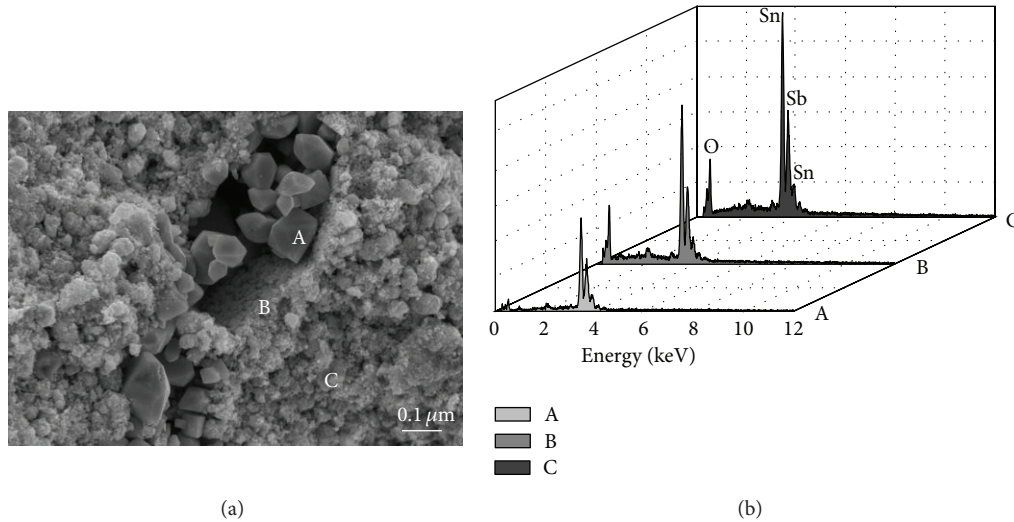


FIGURE 6: SEM micrograph and EDS spectra for ATO nanoceramic containing 5 at.% Sb, after SPS sintering to 700°C.

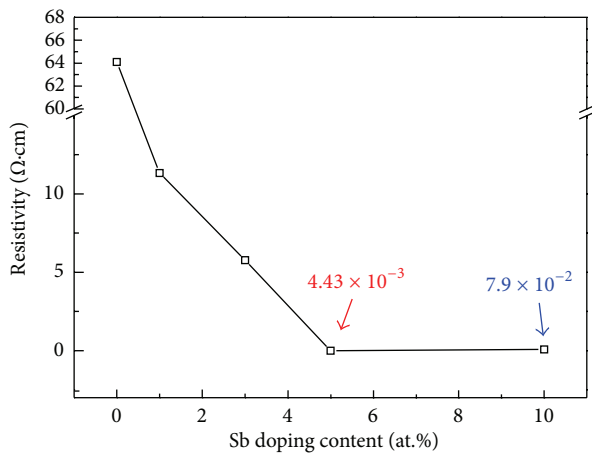


FIGURE 7: The electrical resistivity of sintered ATO nanoceramics with different Sb doping concentrations.

It can be seen that the electrical resistivity decreases with increasing Sb doping concentration and reaches a minimum value of $4.43 \times 10^{-3} \Omega \cdot \text{cm}$ when the Sb doping concentration is 5 at.%. The low electrical resistivity of the sintered ATO nanoceramic with 5 at.% Sb suggests more current passed through the sample and more mass transport occurred due to SPS discharge in the void spaces. This phenomenon explains the high displacement rate for the ATO nanoparticles with 5 at.% Sb, shown in Figure 3, which leads to the highest density of 99.2% for the sintered ATO nanoceramic containing 5 at.% Sb.

Although some researchers have reported the enhanced properties of SPS-prepared ATO ceramics, the density obtained by Park et al. [7] is around 95% and is 92.4% by Scarlat et al. [14], which are lower than our results. Other researchers have prepared dense ATO ceramics with density of >98% using hot pressing sintering, by adding sintering aids such as ZnO, CuO, and MnO₂ [9–11], but

the additive phases deteriorate their electrical properties. From the previous discussion, the high density of SPS-consolidated ATO ceramics can be attributed to three factors: (a) monodispersed ATO nanoparticles with little amount of Sb segregation at the surface provide high sintering potential and high surface activation; (b) low temperature sintering of SPS avoids the need for sintering aids and prevents the formation of deleterious intermediate phases and the decomposition of the ATO system, and the fast sintering rate reduces the evaporation of SnO₂; and (c) semiconducting ATO nanoparticles enable more current to pass through the sample during sintering and SPS discharge in the void spaces enhances the mass transport, which further enhances densification.

4. Conclusions

Monodispersed ATO nanoparticles were prepared via sol-gel method. Antimony is incorporated into the SnO₂ crystal structure in concentrations of 1 at.%, to 10 at.% and the ATO nanoparticles show good crystallinity with crystallite sizes on the order of 5–20 nm. Near full density ATO nanoceramics were obtained without the addition of sintering aids by applying the SPS process at 1000°C with a holding time of 3 min and a heating rate of 100°C/min using the as-synthesized ATO nanoparticles. The highest density achieved in the sintered ATO nanoceramic was 99.2% when the Sb doping concentration was 5 at.%. The high density of the SPS consolidated ATO nanoceramics is attributed to three factors: (a) monodispersed ATO nanoparticles with little amount of Sb segregation at the surface provide high sintering potential and high surface activation; (b) low temperature sintering of SPS prevents the formation of deleterious intermediate phases and the decomposition of the ATO system, and the fast sintering rate reduces the evaporation of SnO₂; and (c) semiconducting ATO nanoparticles enable more current to pass through the sample during sintering and SPS discharge

in the void spaces enhances the mass transport, which further enhances densification.

Acknowledgments

This work is supported by the International Science & Technology Cooperation Program of China (no. 2011DFA52650), the 111 Project (B13035), and the Fundamental Research Funds for the Central Universities in China.

References

- [1] W. Göpel and K. D. Schierbaum, "SnO₂ sensors: current status and future prospects," *Sensors and Actuators B*, vol. 26, no. 1–3, pp. 1–12, 1995.
- [2] W. Germain, H. P. Wilson, and V. E. Archer, *Kirth-Othamer Encyclopedia of Chemical Technology*, vol. 23, Wiley-Interscience, New York, NY, USA, 3rd edition, 1983.
- [3] I. Saadeddin, B. Pecquenard, J. P. Manaud et al., "Synthesis and characterization of single- and co-doped SnO₂ thin films for optoelectronic applications," *Applied Surface Science*, vol. 253, no. 12, pp. 5240–5249, 2007.
- [4] K. Ravichandran and P. Philominathan, "Fabrication of antimony doped tin oxide (ATO) films by an inexpensive, simplified spray technique using perfume atomizer," *Materials Letters*, vol. 62, no. 17–18, pp. 2980–2983, 2008.
- [5] M. Seo, Y. Akutsu, and H. Kagimoto, "Preparation and properties of Sb-doped SnO₂/metal substrates by sol-gel and dip coating," *Ceramics International*, vol. 33, no. 4, pp. 625–629, 2007.
- [6] T. Kimura, S. Inada, and T. Yamaguchi, "Microstructure development in SnO₂ with and without additives," *Journal of Materials Science*, vol. 24, no. 1, pp. 220–226, 1989.
- [7] W. J. Park, W. Jo, D. Y. Kim, and J. H. Lee, "Enhanced densification of pure SnO₂ by spark plasma sintering," *Journal of Materials Science*, vol. 40, no. 14, pp. 3825–3827, 2005.
- [8] N. Dolet, J. M. Heintz, M. Onillon, and J. P. Bonet, "Densification of 0.99SnO₂-0.01CuO mixture: evidence for liquid phase sintering," *Journal of the European Ceramic Society*, vol. 9, no. 1, pp. 19–25, 1992.
- [9] M. S. Castro and C. M. Aldao, "Characterization of SnO₂-varistors with different additives," *Journal of the European Ceramic Society*, vol. 18, no. 14, pp. 2233–2239, 1998.
- [10] I. Saadeddin, H. S. Hilal, B. Pecquenard et al., "Simultaneous doping of Zn and Sb in SnO₂ ceramics: enhancement of electrical conductivity," *Solid State Sciences*, vol. 8, no. 1, pp. 7–13, 2006.
- [11] S. Mihaiu, O. Scarlat, G. Aldica, and M. Zaharescu, "SnO₂ electroceramics with various additives," *Journal of the European Ceramic Society*, vol. 21, no. 10–11, pp. 1801–1804, 2001.
- [12] Z. A. Munir and D. V. Quach, "Electric current activation of sintering: a review of the pulsed electric current sintering process," *Journal of the American Ceramic Society*, vol. 94, pp. 1–19, 2011.
- [13] M. Omori, "Sintering, consolidation, reaction and crystal growth by the spark plasma system (SPS)," *Materials Science and Engineering A*, vol. 287, no. 2, pp. 183–188, 2000.
- [14] O. Scarlat, S. Mihaiu, G. Aldica, M. Zaharescu, and J. R. Groza, "Enhanced properties of Tin(IV) oxide based materials by field-activated sintering," *Journal of the American Ceramic Society*, vol. 86, no. 6, pp. 893–897, 2003.
- [15] J. R. Zhang, X. J. Xu, X. H. Li, L. Gao, and J. Sun, "Fabrication of antimony doped tin oxide ceramics by spark plasma sintering technique," *Chinese Journal of Inorganic Chemistry*, vol. 26, no. 6, pp. 1100–1104, 2010.
- [16] V. Müller, M. Rasp, G. Štefanić et al., "Highly conducting nanosized monodispersed antimony-doped tin oxide particles synthesized via nonaqueous sol-gel procedure," *Chemistry of Materials*, vol. 21, no. 21, pp. 5229–5236, 2009.
- [17] Y. Q. Li, J. L. Wang, S. Y. Fu, S. G. Mei, J. M. Zhang, and K. Yong, "Facile synthesis of antimony-doped tin oxide nanoparticles by a polymer-pyrolysis method," *Materials Research Bulletin*, vol. 45, no. 6, pp. 677–681, 2010.
- [18] D. Jain, K. M. Reddy, A. Mukhopadhyay, and B. Basu, "Achieving uniform microstructure and superior mechanical properties in ultrafine grained TiB₂-TiSi₂ composites using innovative multi stage spark plasma sintering," *Materials Science and Engineering A*, vol. 528, no. 1, pp. 200–207, 2010.
- [19] V. Zamora, A. L. Ortiz, F. Guiberteau, and M. Nygren, "Spark-plasma sintering of ZrB₂ ultra-high-temperature ceramics at lower temperature via nanoscale crystal refinement," *Journal of the European Ceramic Society*, vol. 32, pp. 2529–2536, 2012.
- [20] O. Scarlat, M. Susana-Mihaiu, and M. Zaharescu, "Subsolidus phase relations in the SnO₂-CuSb₂O₆ binary system," *Journal of the European Ceramic Society*, vol. 22, no. 11, pp. 1839–1846, 2002.
- [21] D. G. Stroppa, L. A. Montoro, A. Beltran et al., "Dopant segregation analysis on Sb: SnO₂ nanocrystals," *Chemistry A European Journal*, vol. 17, pp. 11515–11519, 2011.
- [22] I. Saadeddin, H. S. Hilal, B. Pecquenard et al., "Simultaneous doping of Zn and Sb in SnO₂ ceramics: enhancement of electrical conductivity," *Solid State Sciences*, vol. 8, no. 1, pp. 7–13, 2006.
- [23] L. E. Smart and E. A. Moore, *Solid State Chemistry: An Introduction*, CRC Press, 2005.
- [24] J. Robertson and B. Falabretti, "Electronic structure of transparent conducting oxides," in *Handbook of Transparent Conductors*, D. S. Ginley, Ed., p. 27, Springer Science, Business Media, Limited liability company, 2010.
- [25] U. Anselmi-Tamburini, S. Gennari, J. E. Garay, and Z. A. Munir, "Fundamental investigations on the spark plasma sintering/synthesis process: II. Modeling of current and temperature distributions," *Materials Science and Engineering A*, vol. 394, no. 1–2, pp. 139–148, 2005.
- [26] T. Holland, U. Anselmi-Tamburini, D. V. Quacha, T. B. Trana, and A. K. Mukherjee, "Effects of local Joule heating during the field assisted sintering of ionic ceramics," *Journal of the European Ceramic Society*, vol. 32, pp. 3667–3674, 2012.
- [27] Y. J. Wu, J. Li, X. M. Chen, and K. Kakegawa, "Densification and microstructures of PbTiO₃ ceramics prepared by spark plasma sintering," *Materials Science and Engineering A*, vol. 527, no. 20, pp. 5157–5160, 2010.
- [28] L. Minier, S. Le Gallet, Y. Grin, and F. Bernard, "Influence of the current flow on the SPS sintering of a Ni powder," *Journal of Alloys and Compounds*, vol. 508, no. 2, pp. 412–418, 2010.